PICO

PROBE OF INFLATION AND COSMIC ORIGINS

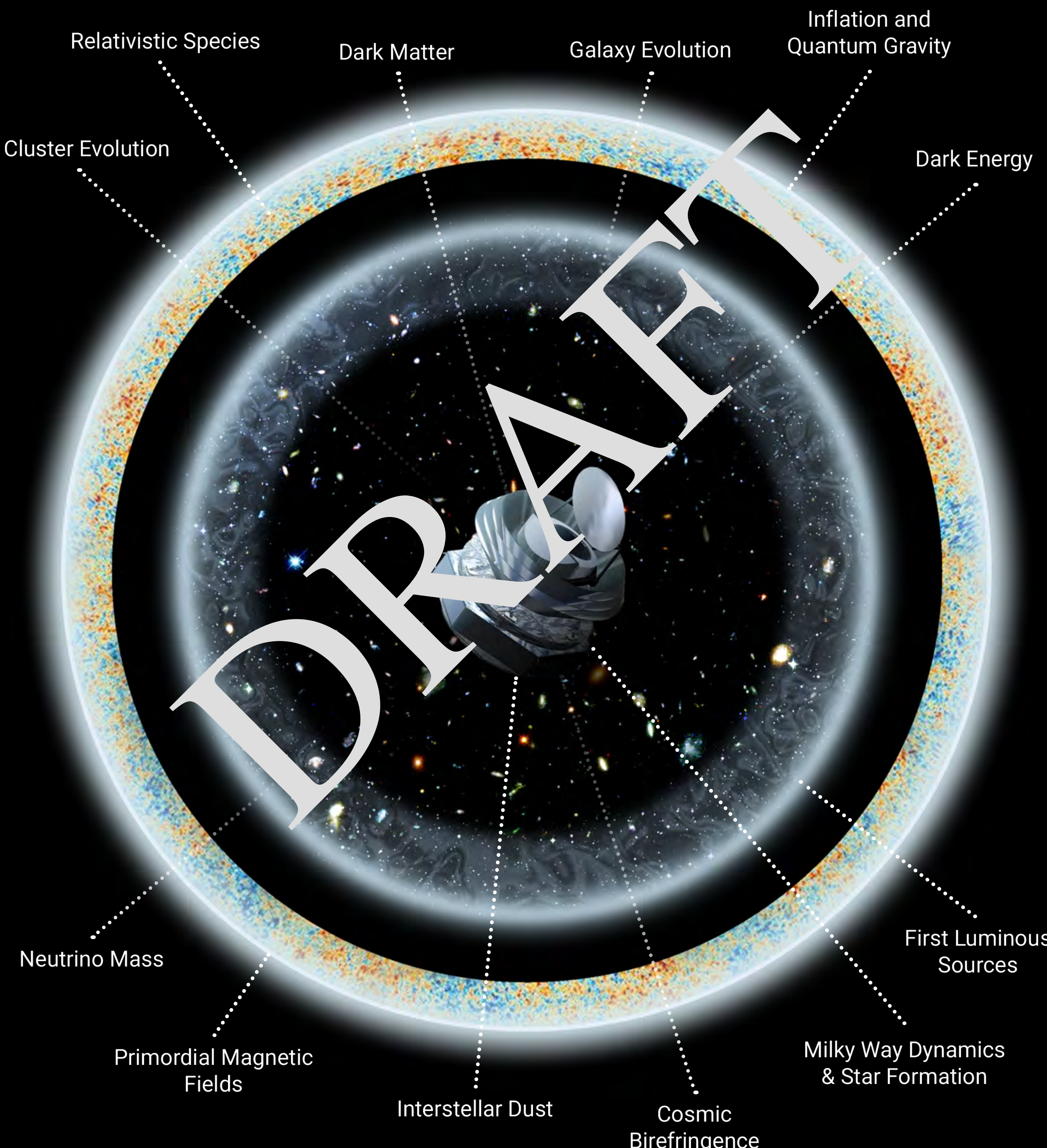

Report from a Probe-Scale Mission Study

January, 2019

Principal Investigator: Shaul Hanany [48]

Steering Committee: Charles Bennett [23], Scott Dodelson [5], Lyman Page [31]

Executive Committee: James Bartlett [1,22], Nick Battaglia [8], Jamie Bock [22], Julian Borrill [26,37], David Chuss [53], Brendan P. Crill [22], Jacques Delabrouille [1,20], Mark Devlin [50], Laura Fissel [29], Raphael Flauger [43], Dan Green [41], J. Colin Hill [6,17], Johannes Hubmayr [28], William Jones [31], Lloyd Knox [42], Al Kogut [27], Charles Lawrence [22], Jeff McMahon [47], Tim Pearson [2], Clem Pryke [48], Marcel Schmittfull [17], Amy Trangsrud [22], Alexander van Engelen [3]

Authors

Marcelo Alvarez [26,41]
Emmanuel Artis [20]
Peter Ashton [25,26,41]
Jonathan Aumont [19]
Ranajoy Banerji [49]
R. Belen Barreiro [18]
James G. Bartlett [1,22]
Soumen Basak [34]
Nick Battaglia [8]
Jamie Bock [22]
Kimberly K. Boddy [23]
Matteo Bonato [13]
Julian Borrill [26,37]
François Bouchet [15]
François Boulanger [10]
Blakesley Burkhart [32]
Jens Chluba [21]
David Chuss [53]
Susan E. Clark [17]
Joelle Cooperrider [22]
Brendan P. Crill [22]
Gianfranco De Zotti [14]
Jacques Delabrouille [1,20]
Eleonora Di Valentino [46]
Joy Didier [51]
Olivier Doré [22]
Josquin Errard [1]
Tom Essinger-Hileman [27]
Stephen Feeney [6]
Jeffrey Filippini [45]
Laura Fissel [29]
Raphael Flauger [43]
Vera Gluscevic [44]
Kris Gorski [22]
Dan Green [41]
Shaul Hanany [48]
Brandon Hensley [31]
Diego Herranz [18]
J. Colin Hill [6,17]
Eric Hivon [15]
Renée Hložek [9]
Johannes Hubmayr [28]
Bradley R. Johnson [7]
William Jones [31]
Terry Jones [48]
Lloyd Knox [42]
Al Kogut [27]
Marcos López-Caniego [11]
Charles Lawrence [22]
Alex Lazarian [52]
Zack Li [31]
Mathew Madhavacheril [31]
Jean-Baptiste Melin [20]
Joel Meyers [36]
Calum Murray [1]
Mattia Negrello [4]
Giles Novak [30]
Giles Novak [30]
Roger O'Brient [22]
Christopher Paine [22]
Tim Pearson [2]
Levon Pogosian [35]
Clem Pryke [48]
Giuseppe Puglisi [24,38]
Mathieu Remazeilles [21]
Graca Rocha [22]
Marcel Schmittfull [17]
Douglas Scott [40]
Ian Stephens [12]
Brian Sutin [22]
Maurizio Tomasi [39]
Amy Trangsrud [22]
Alexander van Engelen [3]
Flavien Vansyngel [16]
Qi Wen [48]
Siyao Xu [52]
Karl Young [48]
Andrea Zonca [33]

Endorsers

Maximilian Abitbol
Zeeshan Ahmed
David Alonso
Jason Austermann
Darcy Barron
Daniel Baumann
Karim Benabed
Bradford Benson
Paolo de Bernardis
Marco Bersanelli
Federico Bianchini
Colin Bischoff
J. Richard Bond
Sean Bryan
Carlo Burigana
Robert Caldwell
Xingang Chen
Francis-Yan Cyr-Racine
Tijmen de Haan
Cora Dvorkin
Ivan Soares Ferreira
Aurelien Fraisse
Silvia Galli
Ken Ganga
Tuhin Ghosh
Tuhin Ghosh
Sunil Golwala
Riccardo Gualtieri
Jon E. Gudmundsson
Nikhel Gupta
Sophie Henrot-Versillé
Thiem Hoang
Kevin M. Huffenberger
Marc Kamionkowski
Reijo Keskitalo
Rishi Khatri
Theodore Kisner
Ely Kovetz
Kerstin Kunze
Guilaine Lagache
Daniel Lenz
François Levrier
Marilena Loverde
Philip Lubin
Juan Macias-Perez
Nazzareno Mandolesi
Carlos Martins
Silvia Masi
Amber Miller
Lorenzo Moncelsi
Pavel Motloch
Tony Mroczkowski
Suvodip Mukherjee
Johanna Nagy
Pavel Naselsky
Federico Nati
Paolo Natoli
Michael Niemack
Elena Orlando
Francesco Piacentini
Nicolas Ponthieu
Giuseppe Puglisi
Benjamin Racine
Christian Reichardt
Christophe Ringeval
Karwan Rostem
Anirban Roy
Jose-Alberto Rubino-Martin
Maria Salatino
Benjamin Saliwanchik
Neelima Sehgal
Sarah Shandera
Erik Shirokoff
Anže Slosar
Tarun Souradeep
George Stein
Aritoki Suzuki
Eric Switzer
Andrea Tartari
Grant Teply
Peter Timbie
Matthieu Tristram
Caterina Umiltà
Vincent Vennin
Licia Verde
Patricio Vielva
Benjamin Wallisch
Benjamin Wandelt
Scott Watson
Rien van de Weygaert
Edward J. Wollack
Siavash Yasini

Affiliations

1. APC, Univ Paris Diderot, CNRS/IN2P3, CEA/lrfu, Obs de Paris, Sorbonne Paris Cité, France.
2. California Institute of Technology.
3. Canadian Institute for Theoretical Astrophysics, University of Toronto, Canada.
4. Cardiff University School of Physics and Astronomy.
5. Carnegie Melon University.
6. Center for Computational Astrophysics, Flatiron Institute.
7. Columbia University.
8. Cornell University.
9. Department of Astronomy & Astrophysics and Dunlap Institute, University of Toronto, Canada.
10. Ecole Normale Superieure, Paris, France.
11. European Space Astronomy Centre.
12. Harvard-Smithsonian Center for Astrophysics.
13. INAF-Istituto di Radioastronomia and Italian ALMA Regional Centre, Italy.
14. INAF-Osservatorio Astronomico di Padova, Italy.
15. Institut d'Astrophysique de Paris, CNRS and Sorbonne Université, France.
16. Institut d'Astrophysique Spatiale, CNRS, Univ. Paris-Sud, Université Paris-Saclay, France.
17. Institute for Advanced Study, Princeton.
18. Instituto de Física de Cantabria (CSIC-Universidad de Cantabria), Spain.
19. IRAP, Université de Toulouse, France.
20. IRFU, CEA, Université Paris-Saclay, France.
21. JBCA, University of Manchester.
22. Jet Propulsion Laboratory, California Institute of Technology.
23. Johns Hopkins University.
24. Kavli Institute for Particle Astrophysics and Cosmology.
25. Kavli Institute for the Physics and Mathematics of the Universe (WPI).
26. Lawrence Berkeley National Laboratory.
27. NASA Goddard Space Flight Center.
28. National Institute of Standards and Technology.
29. National Radio Astronomy Observatory.
30. Northwestern University.
31. Princeton University.
32. Rutgers University.
33. San Diego Supercomputer Center, University of California, San Diego.
34. School of Physics, Indian Institute of Science Education and Research Thiruvananthapuram, India.
35. Simon Fraser University.
36. Southern Methodist University.
37. Space Sciences Laboratory, University of California, Berkeley.
38. Stanford University.
39. Università degli studi di Milano.
40. University of British Columbia, Canada.
41. University of California, Berkeley.
42. University of California, Davis.
43. University of California, San Diego.
44. University of Florida.
45. University of Illinois, Urbana-Champaign.
46. University of Manchester.
47. University of Michigan.
48. University of Minnesota - Twin Cities.
49. University of Oslo, Norway.
50. University of Pennsylvania.
51. University of Southern California.
52. University of Wisconsin - Madison.
53. Villanova University.

***

This research was funded by a NASA grant NNX17AK52G to the University of Minnesota / Twin Cities, by the Jet Propulsion Laboratory, California Institute of Technology, under a contract with the National Aeronautics and Space Administration, and by Lockheed Martin Corporation.
Substantial contributions to the development of PICO were volunteered by scientists at many institutions world-wide. They are very gratefully acknowledged.

The information presented about the PICO mission concept is pre-decisional and is provided for planning and discussion purposes only.

The cost information contained in this document is of a budgetary and planning nature and is intended for informational purposes only. It does not constitute a commitment on the part of JPL and/or Caltech.

Contents

1 Executive Summary

The cosmic microwave background (CMB) comes to us from the furthest reaches of the observable Universe, and its photons experience all of cosmic history. Created when the Universe was a hotter, simpler place, CMB photons probe fundamental physics, provide exquisite measurements of the constituents of the cosmos, and test relativity. On their journey they feel the impact of the gravitational potentials formed from the assembling cosmic web of superclusters, clusters, and galaxies. They interact with the ionized gas in the inter- and circum-galactic medium, gas that eventually fuels star and galaxy formation. Superposed upon the CMB is the emission from multiple extragalactic sources and from our Galaxy. All of this leaves an imprint which sensitive measurements can disentangle so that CMB studies impact every aspect of cosmology and many areas of astrophysics.

Building upon a long legacy of successful measurements, the next decade holds tremendous potential for new, exciting CMB discoveries. Such discoveries, delivered by the Probe of Inflation and Cosmic Origins (PICO, Fig. 1.1), promise to be revolutionary, affecting physics, astrophysics, and cosmology. PICO is an imaging polarimeter that will scan the sky for 5 years in 21 frequency bands spread between 21 and 799 GHz; see Tables 1.1 and 1.2. It will produce ten independent full-sky surveys of intensity and polarization with a final combined-map noise level equivalent to 3300 *Planck* missions for the baseline required specifications, though in our current best-estimate it would perform as 6400 *Planck* missions.

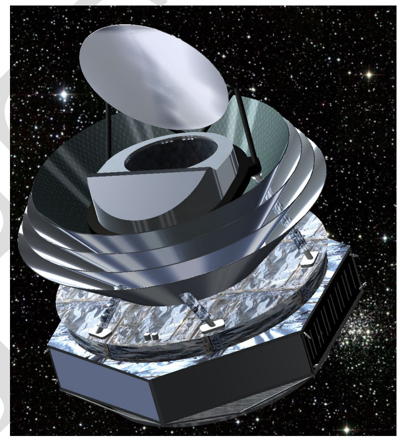

Figure 1.1: The PICO spacecraft

With these capabilities, unmatched by any other existing or proposed platform, PICO will have compelling and broad science deliverables. The mission will address the seven science objectives (SOs), which are listed in Table 1.3. Delivering this set was the basis for selecting PICO's design and for setting instrument requirements. But PICO's science reach is broader than the baseline set.

PICO could determine the energy scale of inflation and give a first, direct probe of quantum gravity (SO1, § 2.2). The mission will attempt to detect the signal that arises from gravitational waves sourced by inflation and parameterized by the tensor-to-scalar ratio, r, at a level of $r = 5 \times 10^{-4}\,(5\sigma)$. This level is 100 times lower than current upper limits, and more than 10 times lower than limits forecast by funded experiments. If the signal is not detected, PICO will constrain broad classes of inflationary models and exclude at 10σ models for which the characteristic scale in the potential is the Planck scale (SO1 and SO2). The combination of data from PICO and LSST can constrain features in the inflationary potential, the field content during inflation and could rule out all models of slow-roll single-field inflation, marking a watershed in studies of inflation. reword?

The mission will have a deep impact on particle physics by measuring the expected sum of the neutrino masses with 4σ confidence, rising to 7σ if the sum is near 0.1 eV (SO3). Reaching the 4σ level can only be done with an instrument that can measure the polarization of the CMB on the largest angular scales, a measurement best done from space, which gives access to the full sky, and with a broad band of frequencies to remove foreground contaminants. Cluster counts provided by PICO in combination with followup redshift measurements, and PICO's map of the projected gravitational potentials along the line of site in combination with the LSST gold sample of galaxies, will give two additional independent and equally competitive constraints on the sum of neutrino masses.

The measurements will either detect or strongly constrain deviations from the standard model of particle physics by counting the number of light particle species $N_{\rm eff}$ in the early universe. The constraint of $\Delta N_{\rm eff} < 0.06\,(2\sigma)$ will move the allowed decoupling temperature of a hypothetical new vector particle to temperatures that are 400 times higher than currently determined by *Planck* (SO4). The data will enable a search for primordial magnetic fields with sufficient sensitivity to rule them out as the sole source for the largest observed galactic magnetic fields; will improve by $\sim$300 constraints on polarization rotation arising from early universe fields that lead to cosmic birefringence, and will thus constrain string theory-motivated axions; and will constrain generic models of dark matter candidates.

PICO will elucidate the processes affecting the evolution of cosmic structures. It will measure the optical depth to reionization τ with an error $\sigma(\tau) = 0.002$ limited only by the small number of spatial modes available in the largest angular scale CMB polarization (SO5). The measurement will be used to constrain models of the formation of the first luminous sources, and is a key input to all astrophysical attempts to improve the determination of the sum of neutrino masses. The data will give a map of the projected gravitational potential due to all structures with a signal-to-noise ratio (SNR) 14 times higher than *Planck*, and a catalog of 150,000 clusters extending to their earliest formation redshift. Each of these datasets will be used in combination with other data – from LSST and from future optical and infrared surveys – to independently constrain the evolution of the amplitude of linear fluctuations $\sigma_8(z)$, with sub-percent accuracy.

Cross-correlating PICO's map of the thermal Sunyaev–Zeldovich effect with LSST's gold sample of galaxies, a correlation that is forecast to have an SNR exceeding 1000, will give precise tracing of the evolution of thermal pressure with z. This will be used to place constraints on models of energetic feedback, which is the most uncertain ingredient in models of galaxy formation.

PICO's maps of the Milky Way will be used to resolve long-standing questions about our own Galaxy. Galactic interstellar dust grains are a link between atoms and molecules and planetary objects, yet their composition and their role in Galactic chemistry is still under debate. Galactic magnetic fields are known to play a key role in the dynamics of gas in the Galaxy, and in determining the efficiency of star formation, but their quantitative contribution relative to turbulence is yet to be determined. With the mission's Galactic dust polarization maps we will constrain dust properties, including composition, temperature, and emissivities (SO6), and we will make maps of the Galactic magnetic field. These detailed $1'$ resolution maps will be used to quantify the relative roles of turbulence and magnetic fields in the dynamics of the Galaxy and in the observed low star-formation efficiency (SO7).

PICO will give full-sky maps of intensity and polarization at 21 frequency bands, each much than *Planck*'s nine frequency maps in intensity and seven in polarization; five PICO bands will have polarization information at frequencies between 385 and 800 GHz that *Planck* did not have. At 385 GHz PICO's noise is 100 times lower than *Planck*'s at 353 GHz. And PICO's highest resolution is five times finer than *Planck*'s. Only PICO will provide such full-sky legacy maps. With the six maps at frequencies not accessible to ground-based experiments we will: constrain the early phases of galaxy evolution by discovering 4500 strongly lensed dusty galaxies with z up to 5; investigate the early phases of cluster evolution by discovering 50,000 proto-clusters out to $z \sim 4.5$; perform a census of cold dust in 30,000 low z galaxies; make cosmic infrared background maps of the anisotropies due to dusty star-forming galaxies; map magnetic fields in 70 nearby galaxies; and, with 3,000-fold increase relative to *Planck* in the number of independent measurements of magnetic field in our own Galaxy, study how magnetic fields are generated through a combination of turbulence and large-scale gas motion.

With its broad frequency coverage PICO is better equipped than any other current or planned instrument to separate the detected signals to their original sources of emission. This capability is most important for the faintest of signals, the telltale of inflation, which is already known to be dominated by Galactic foregrounds. Our simulations indicate that PICO's combination of low noise and multitude of bands is sufficient to separate the inflationary signal from the foregrounds at the required level. But current uncertainties on the parameters characterizing Galactic foregrounds are large and we recommend support for (1) modeling, simulation, and algorithm development for effective foreground separation, and (2) improved Galactic emission measurements with sub-orbital experiments. combine recommendations?

Similar to its successful predecessors, WMAP and *Planck*, PICO will conduct observations from L2, a location that ensures a stable thermal environment. It will execute ten redundant, full-sky surveys, each

Table 1.1: **Mission Parameters**

Combined polarization map depth (rms noise in 1×1 arcmin^2 pixel):	
Baseline	0.87 μK$_{\rm CMB}$ arcmin equivalent to 3250 *Planck* missions
CBE[a]	0.61 μK$_{\rm CMB}$ arcmin equivalent to 6400 *Planck* missions
Survey duration	5 yr
Orbit type	Sun-Earth L2
Launch mass	2147 kg
Total power	1320 W
Data rate	6.1 Tbits/day
Cost	$ 958M

[a] CBE = Current best estimate.

Table 1.2: **Frequency Bands, Resolution, and Noise Level**

Frequency [GHz]	21	25	30	36	43	52	62	75	90	108	129	155	186	223	268	321	385	462	555	666	799
FWHM [arcmin]	38.4	32.0	28.3	23.6	22.2	18.4	12.8	10.7	9.5	7.9	7.4	6.2	4.3	3.6	3.2	2.6	2.5	2.1	1.5	1.3	1.1
Polarization map depth:																					
Baseline [μK$_{\rm CMB}$ arcmin]	23.9	18.4	12.4	7.9	7.9	5.7	5.4	4.2	2.8	2.3	2.1	1.8	4.0	4.5	3.1	4.2	4.5	9.1	45.8	177	1050
CBE[a] [μK$_{\rm CMB}$ arcmin]	16.9	13.0	8.7	5.6	5.6	4.0	3.8	3.0	2.0	1.6	1.5	1.3	2.8	3.2	2.2	3.0	3.2	6.4	32.4	125	740
Baseline [Jy/sr]	8.3	10.9	11.8	12.9	19.5	23.8	45.4	58.3	59.3	77.3	96.0	119	433	604	433	578	429	551	1580	2080	2880
CBE[a] [Jy/sr]	5.9	7.7	8.3	9.2	13.8	16.8	32.1	41.3	41.8	53.5	69.3	84	302	436	304	411	303	387	1120	1470	2040

Table 1.3: **Science Traceability Matrix (STM)**

Science Goals from NASA Science Plan	**Science Objectives**	**Scientific Measurement Requirements**			**Instrument (single instrument, single mode)**		**Mission Functional Requirements**
		Model Parameters	Physical Parameters	Observables	Functional Requirements	Projected Performance	
Explore how the Universe began (Inflation)	**SO1**. Probe the physics of the big bang by detecting the energy scale at which inflation occurred if it is above 4×10^{15} GeV, or place an upper limit if it is below (§ 2.2.1, Fig. 2.1)	Tensor-to-scalar ratio r: $\sigma(r) = 1 \times 10^{-4}$ at $r = 0$; $r < 5 \times 10^{-4}$ at 5σ confidence level[a]	CMB polarization *BB* power spectrum for modes $2 < \ell < 300$ to cosmic-variance limit, and CMB lensing power spectrum for modes $2 < \ell < 1000$ to cosmic-variance limit	Linear polarization across $60 < \nu < 300$ GHz over entire sky; foreground separation requires $21 < \nu < 799$ GHz	Frequency coverage: central frequencies ν_c from 21 to 799 GHz Frequency resolution: $\Delta\nu/\nu_c = 25\%$ Sensitivity: See Table 1.1 Combined instrument noise: $< 0.61\,\mu{\rm K_{CMB}}\sqrt{\rm s}$ Angular resolution [for delensing and foreground separation]: FWHM $= 6.2' \times (155\,{\rm GHz}/\nu_c)$ Effective aperture: 1.4 m Sampling rate: $(3/{\rm BeamFWHM}) \times (336'/{\rm s})$	Frequency coverage: See Table 1.1 21 bands with ν_c from 21 to 799 GHz Frequency resolution: $\Delta\nu/\nu_c = 25\%$ Sensitivity: See Table 1.1 Combined instrument noise: $0.43\,\mu{\rm K_{CMB}}\sqrt{\rm s}$ Angular resolution: See Table 1.1 FWHM $=$ $6.2' \times (155\,{\rm GHz}/\nu_c)$; $1.1'$ for $\nu_c = 799$ GHz Sampling rate: See Table 3.1 $(3/{\rm BeamFWHM}) \times (336'/{\rm s})$	Sun-Earth L2 orbit with Sun-Probe-Earth $< 15°$ 5 yr survey with $\geq 95\%$ survey efficiency Full sky survey: Spin instrument at 1 rpm; boresight 69° off spin axis; spin axis 26° off anti-Sun line, precessing 360° / 10hr Pointing control: Spin axis $60'$ (3σ, radial); spin 1 ± 0.1 rpm (3σ) Pointing stability: Drift of spin axis $< 1'$/1min (3σ, radial); jitter $< 20''$/20 ms (3σ, radial) Pointing knowledge (telescope boresight): $10''$ (3σ, each axis) from spacecraft attitude; $1''$ (1σ, total) final reconstructed Return and process instrument data: 1.5 Tbits/day (after $4\times$ compression) Thermally isolate instrument from solar radiation and from spacecraft bus
	SO2. Probe the physics of the big bang by excluding classes of potentials as the driving force of inflation (§ 2.2.1, Fig. 2.2)	Spectral index (n_s) and its derivative ($n_{\rm run}$): $\sigma(n_s) < 0.0015$; $\sigma(n_{\rm run}) < 0.002$	CMB polarization *BB* power spectrum for modes $2 < \ell < 1000$ to cosmic-variance limit	Intensity and linear polarization across $60 < \nu < 220$ GHz over the entire sky			
Discover how the Universe works (neutrino mass and $N_{\rm eff}$)	**SO3**. Determine the sum of neutrino masses. (§ 2.2.2, Fig. 2.5)	Sum of neutrino masses (Σm_ν): $\sigma(\Sigma m_\nu) = 14$ meV with DESI or Euclid[b]; independently $\sigma(\Sigma m_\nu) =$ 14 meV using cluster counts[c]	CMB polarization power spectra for modes $2 < \ell < 4000$; CMB intensity maps (to identify clusters using the Compton-y signal)				
	SO4. Tightly constrain the thermalized fundamental particle content of the early Universe (§ 2.2.2, Fig. 2.4)	Number of light relic particle species $N_{\rm eff}$: $\Delta N_{\rm eff} < 0.06$ (95%)	CMB temperature and polarization auto and cross power spectra $2 < \ell < 4000$				
Explore how the Universe evolved (reionization)	**SO5**. Distinguish between models that describe the formation of the earliest luminous sources in the Universe (§ 2.3, Fig. 2.6)	Optical depth to reionization (τ): $\sigma(\tau) < 0.002$	CMB polarization *EE* power spectrum for modes $2 < \ell < 40$ to cosmic-variance limit	Linear polarization across $60 < \nu < 300$ GHz over entire sky; foreground separation encompassed by SO1			
Explore how the Universe evolved (Galactic structure and dynamics)	**SO6**. Constrain the temperatures and emissivities characterizing the Milky Way's interstellar dust (§ 2.5)	Intrinsic polarization fractions of Galactic dust components to accuracy better than 3% when averaged over $10'$ pixels	Intensity and polarized intensity as a function of frequency	Intensity and linear polarization maps in 12 frequency bands between 108 and 799 GHz.	Encompassed by S01–5		
	SO7. Determine if magnetic fields are the dominant cause of low Galactic star-formation efficiency (§ 2.5)	Ratio of cloud mass to maximum mass that can be supported by magnetic field ("Mass to flux ratio" μ); ratio of turbulent energy to magnetic energy (Alfvén Mach number $\mathscr{M}_A$) on scales 0.05–100 pc	The turbulence power spectrum on scales 0.05–100 pc; magnetic field strength (B) as a function of spatial scale and density; hydrogen column density; gas velocity dispersion[d]	Intensity and linear polarization with $<$ 1 pc resolution for thousands of molecular clouds and with < 0.05 pc for the 10 nearest molecular clouds; maps of polarization with 1' resolution over the entire sky	Encompassed by SO1–5, except: Angular resolution: $\leq 1.1'$ (at highest frequency) Sensitivity at 799 GHz: 27.4 kJy/sr		

[a] The values predicted include delensing and foreground subtraction; see § 2.2.1.
[b] Using τ and the power spectrum of the reconstructed lensing map (§ 2.3.2), both from PICO's measurements, and baryon acoustic oscillation data from DESI or Euclid.
[c] The constraint using clusters requires redshifts by future optical and IR surveys.
[d] Hydrogen column density and gas velocity dispersion will be measured by 21-cm surveys including HI4PI and GALFA-HI.

complete within 6 months. The sky scan pattern, which is optimized for control of polarimetric systematic uncertainties, ensures that the measured I, Q, and U Stokes parameters can be reconstructed by each of the 12,996 polarization-sensitive detectors. The large multiplicity of independent maps and sky surveys, and the stable environment will together give control of systematic uncertainties unmatched by any other platform.

The mission has a single instrument that surveys the sky with the same repeated pattern. The telescope is a 1.4 m entrance-aperture, two-reflector system, with ambient temperature primary, and 4.5 K actively cooled aperture-stop and secondary. The 0.1 K cooled focal plane is based on three-color pixels coupling the incident radiation to transition-edge-sensor bolometers that are read out using a time-domain multiplexed system. All of these technologies are either already in use by sub-orbital experiments, or are simple extensions to higher or lower frequency bands. We recommend continued support for technology development and maturation in the laboratory and by sub-orbital experiments.

The science PICO will deliver addresses NASA science objectives, is compelling, timely, and will enrich broad areas of astrophysics. There is a long heritage of space and sub-orbital measurements in these frequency bands; the PICO implementation is a conservative extension of past successes; the mission relies on today's technologies; no new fundamental developments are required. PICO is the only single-platform instrument with the combination of sensitivity, angular resolution, frequency bands, and control of systematic effects that can deliver the compelling, timely, and broad science. We recommend a start for the mission in the next decade. We also recommend support for continued technology development and sub-orbital experiments, and for studying the effects of foregrounds of systematic effects through analytic work and simulations.

2 Science

2.1 Introduction

The Probe of Inflation and Cosmic Origins (PICO) has seven science objectives (SOs) that derive from NASA's three science strategic goals: to explore how the Universe began; to discover how the Universe works; and to explore how the Universe evolved. The SOs, which include probing the inflationary epoch after the big bang, constraining the properties of fundamental particles and potentially detecting new ones, probing the structure and evolution of the Universe, and understanding the structure of our own Galaxy, require measurements in and around frequency bands in which the cosmic microwave background is most intense. The SOs and the measurement requirements derived from them are given in Table 1.3 and define the PICO 'baseline design'. This report focuses on the primary SOs listed in the Table but also describes the much broader set of science deliverables that the mission design enables.

The PICO mission consists of a single instrument: an imaging polarimeter that surveys the entire sky at 21 frequency bands spread between 21 and 799 GHz. The telescope has an aperture of 1.4 m giving diffraction-limited resolution between $38'$ and $1'$. The instrument incorporates a 0.1 K cooled focal plane that hosts 12,996 transition-edge-sensor (TES) bolometric detectors. The baseline design contains a margin of 40% in detector noise. We therefore include throughout this report performance estimates that are based also on our current estimate for the actual performance. Those are labeled current best estimate (CBE). Table 1.1 gives key mission parameters and Table 1.2 gives the frequency bands, resolution, and both baseline and CBE noise levels. Experience with past space missions, most recently with *Planck*, shows that pre-mission calculated detector performance is in fact achieved in space [*1*, *2*].

Mission operations throughout the 5-year duration of the survey are simple. The spacecraft spins around its symmetry axis at 1 rpm and the symmetry axis precesses around the anti-sun direction with a period of 10 hours. With this scan pattern, which repeats itself, the entire sky is scanned every 6 months giving ten independent full-sky maps of the intensity and polarization Stokes parameters T, Q and U. The scan pattern is optimized for polarization measurements as each sky pixel is scanned along multiple orientations. Therefore independent full-sky maps of all Stokes parameters can be reconstructed from the data of each of the 12,996 polarization-sensitive detectors.

Some of the PICO polarization science goals are more appropriately described in terms of E and B

polarization maps rather than Q and U [3–6]. This is because sources of polarization signatures that are scalar in nature, such as primordial density perturbations, can only produce E-mode polarization. Sources that are tensor in nature, such as gravitational waves, can produce both E- and B-mode polarization. The angular power spectra of E and B maps will be denoted as EE and BB.

This report assumes that PICO's Phase A will start in 2023. The science outcomes are expected to break new ground, and to be complementary to data sets available at the end of 2020s and the beginning of the following decade. Therefore we are including performance comparisons to funded projects that are in implementation and for which final design specifications and projections exist in the literature. Such next-generation US-based CMB experiments are collectively denoted as Stage-3 (S3) [7–13].

This section describes PICO's science objectives, places them in context of current knowledge, and provides performance forecasts (§ 2.2–2.6). It gives our estimates of the efficacy of separating the detected radiation into the several astrophysical sources of emission (§ 2.7); an assessment of anticipated systematic uncertainties (§ 2.8); a discussion of PICO's complementarity with ground-based measurements (§ 2.9); and the measurement requirements that derive from the combination of these topics (§ 2.10). § 3 describes the instrument, which consists of the telescope, the focal plane, the detector readout, and shielding and cooling hardware. The section also describes plans for integration and testing. § 4 describes the operations, including the instrument's survey of the sky, and the spacecraft. In § 5 we discuss the path to maturing the few technologies that are not yet at Technology Readiness Level (TRL) 6, and potential descopes. Project management, assessment of risk, and costs are presented in § 6.

2.2 Fundamental Physics

2.2.1 Gravitational Waves and Inflation

• **Targets** Measurements of the CMB together with Einstein's theory of general relativity imply that the observed density perturbations must have been created long before the CMB was released, and rather remarkably even before the Universe became filled with a hot and dense plasma of fundamental particles. Understanding the mechanism generating these perturbations, which evolved to fill the Universe with structures, is one of the most important open questions in cosmology. In addition to density perturbations, this mechanism may have also produced gravitational waves that would have left a B-mode polarization signature in the CMB [3, 4]. Any detection of primordial B-mode polarization by PICO will constitute evidence for gravitational waves from the same primordial period that created the density perturbations and will open a new window onto this early epoch. Because the dynamics of gravitational waves is essentially unaffected by the plasma, they would be a pristine relic from the earliest moments of our Universe, and their properties would shed light on the mechanism that created the primordial perturbations.

Inflation, a period of nearly exponential expansion of the early Universe [14–17], is the leading paradigm explaining the origin of the primordial density perturbations [18–22]. It predicts a nearly scale-invariant spectrum of primordial gravitational waves originating from quantum fluctuations [23]. Measurements of the CMB are the only foreseeable way to detect these gravitational waves.

The strength of the signal, quantified by the tensor-to-scalar ratio r, is a direct measure of the expansion rate of the Universe during inflation. Together with the Friedmann equation, it reveals one of the most important characteristics of inflation: its energy scale.[1] A detection of r "would be a watershed discovery", a quote from the 2010 decadal panel report [30]. The combination of data from *Planck* and the BICEP/Keck Array give the strongest constraint to date, $r < 0.06$ (95%) [31]. Next decade S3 efforts strive to reach $\sigma(r) = 2 \times 10^{-3}$ [11, 32].

PICO's goal is to detect primordial gravitational waves if inflation occurred at an energy scale of at least 5×10^{15} GeV, or equivalently $r = 5 \times 10^{-4}\,(5\sigma)$ (SO1 in Table 1.3 and Fig. 2.1). A detection will

[1] In some models of inflation the one-to-one correspondence between r and the energy scale of inflation does not hold because there are additional sources of gravitational waves [29]. However, in these models the signal is highly non-Gaussian and could be distinguished from quantum fluctuations.

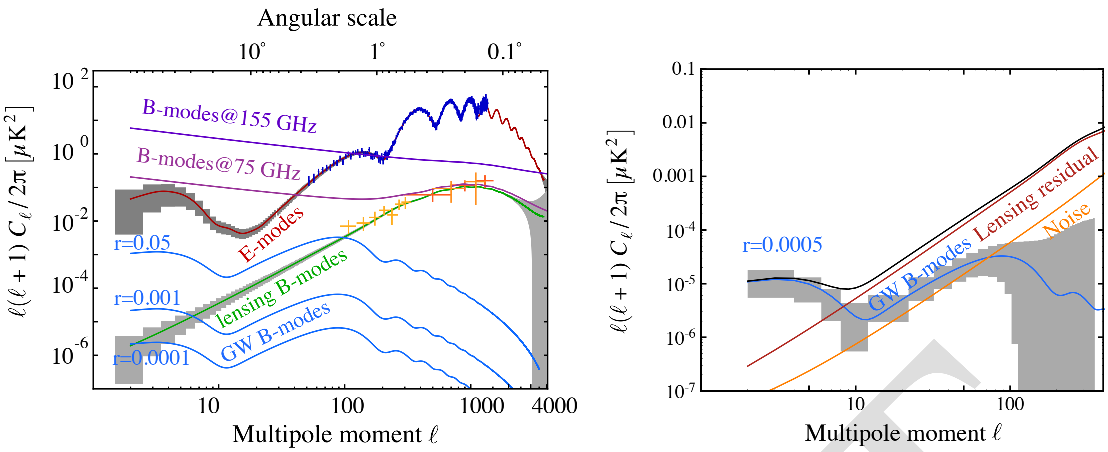

Figure 2.1: With PICO's baseline configuration we will measure the *EE* (left, red) and lensing *BB* (green) angular power spectra with high precision (grey). PICO's goal is to detect $r = 5\times10^{-4}\,(5\sigma)$ (right, grey). This forecast includes PICO's 80% delensing (red) and foreground separation. The baseline noise level (right, orange) allows detection of even lower levels; we expect foreground separation to limit performance. As an example we show the total *BB* spectra on the cleanest 60% of the sky at 75 and 155 GHz (left, purple). The foregrounds largely dominate the cosmological signals. Also shown are measurements of lensing from current experiments (left, orange) [24–27], *Planck*'s *EE* measurements (left, dark blue) [28], and the *BB* spectrum produced by an inflationary gravity wave (GW) signal with different values of r (cyan).

have profound implications for fundamental physics because it will provide evidence for a new energy scale tantalizingly close to the energy scale associated with grand unified theories, probe physics at energies far beyond the reach of terrestrial colliders, and be the first observation of a phenomenon associated with quantum gravity [33].

There are only two classes of slow-roll inflation in agreement with current data that naturally explain the observed value of the spectral index of primordial fluctuations n_s [34]. The first class is characterized by potentials of the form $V(\phi) \propto \phi^p$. This class includes many of the simplest models of inflation, some of which have already been strongly disfavored by existing observations. Select models in this class are shown as blue lines in Fig. 2.2. If the constraints on n_s tighten by about a factor of two with the central value unchanged, and the upper limit on r improves by an order of magnitude, this class would be ruled out.

The second class is characterized by potentials that approach a constant as a function of field value, either like a power law or exponentially. Two representative examples in this class are shown as the green and gray bands in Fig. 2.2. This class also includes R^2 inflation, which predicts a tensor-to-scalar ratio of $r \sim 0.004$. All models in this class with a characteristic scale in the potential that is larger than the Planck scale predict a tensor-to-scalar ratio of $r \gtrsim 0.001$.

Many microphysical models in this class possess a characteristic scale that is super-Planckian. PICO will either detect gravitational waves with high confidence or will exclude all models with a Planckian characteristic scale with high significance. But not all models have a super-Planckian characteristic scale. The Goncharov-Linde model is an example with a somewhat smaller characteristic scale. It predicts a tensor-to-scalar ratio of $r \sim 4\times10^{-4}$ [35], still within reach of PICO. In addition, there are models with significantly smaller values that are out of reach, but distinguishing between models with sub- and super-Planckian characteristic scales would provide much needed guidance to discriminate between classes of ideas for the earliest moments of our universe.

• **Observational Considerations** The *BB* angular power spectrum measured by PICO will have contributions from Galactic sources of emission and 'lensing' *B*-modes, created by gravitational lensing of *E*-modes as the CMB photons traverse the gravitational potentials throughout the Universe (Fig. 2.1 and § 2.3.2). In case of an r detection, there will be two additional features due to the inflationary signal. One is the 'recombination peak' at $\ell \sim 80$ and the other is the 'reionization peak' at multipoles of $\ell \lesssim 10$. PICO's strong

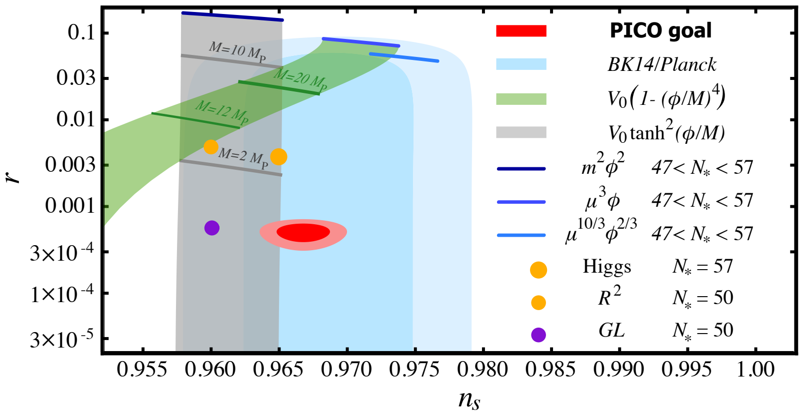

Figure 2.2: Current 1σ and 2σ limits on r and n_s (cyan) and forecasted constraints for a fiducial model with $r = 0.0005$ for PICO, together with predictions for selected models of inflation. Characteristic super-Planckian scales in the potentials are marked with darker lines.

constraints on r derive from using all available ℓ modes.

The Galactic signals act as foregrounds, and uncertainty in the characterization of these foregrounds already limits our ability to constrain r. An analytic performance forecast accounting for PICO's statistical noise level and a foreground model that has polarized emission from two components of dust, synchrotron radiation, and correlations between synchrotron and dust emission, gives $\sigma(r) = 2 \times 10^{-5}$, five times lower than our baseline requirement. This margin allows for degradation in foreground removal through inclusion of physical effects known to exist but not captured in the analytic forecasts. These effects are included in end-to-end, map-based simulations, which indicate that PICO will achieve its requirement; see Section 2.7.

When the tensor-to-scalar ratio $r \simeq 0.01$, the *BB* lensing and inflation spectra are comparable in magnitude at the recombination peak ($\ell \sim 80$). For lower levels of r, the lensing B-mode dominates, but the B-mode maps can be 'delensed' if the polarization maps are measured with few-arcmin resolution and sufficient depth [36, 37]. Forecasts for PICO show that at least 73% of the lensing B-mode power can be removed for the baseline configuration, after accounting for Galactic foreground separation. As much as 84% will be removed for the CBE and for milder foreground contamination. For measuring the recombination peak, delensing is essential to reach PICO's limits on r, and this was a driver in choosing the resolution of the instrument.

For the levels of r targeted by PICO, the *BB* reionization signal ($\ell \sim 5$) has a somewhat higher level than the lensing spectrum, but the map-level foregrounds at this angular scale are at least two orders of magnitude brighter. PICO's instrument temporal stability, absence of atmospheric noise, full-sky coverage, and unmatched capability to characterize and separate foregrounds make it the most suitable instrument to measure these lowest multipoles. No S3 experiments have measured or plan to measure B-modes at $\ell < 40$ that reach to $\sigma(r) < 0.006$ at the lowest multipoles [13, 38].

If an inflationary B-mode signal is detected, it is important to characterize its entire ℓ dependence in the predicted reionization and recombination peaks, in order to confirm – rather than assume – its expected dependence on angular scale. Furthermore, the PICO full-sky coverage will enable detection of the recombination peak in several independent patches of the sky, giving an important systematic cross-check.

• **Scalar Spectral Index and Non-Gaussianity** Models of the early Universe differ not only in their predictions for r and the scalar spectral index n_s, but also for the scale-dependence of n_s, a parameter commonly called 'the running of n_s' and labeled n_{run}. PICO will improve n_s and n_{run} constraints by a factor of three relative to *Planck* to achieve $\sigma(n_s) = 0.0015$ and $\sigma(n_{run}) = 0.002$. For many models of inflation, how reheating occurred is unknown, and this translates to different predictions for n_s and n_{run} [**?**]. PICO's precision is sufficient to distinguish between different possible reheating scenarios at $> 3\sigma$ (SO2).

The simplest models of inflation, in which there is a single inflaton field, predict primordial fluctuations that are very nearly Gaussian with $|f_{NL}^{local}| < 1$, where f_{NL}^{local} is a parameter quantifying the level of local non-Gaussianity [**?**]. A detection of $|f_{NL}^{local}| > 1$ points exclusively to models of inflation with multiple fields

(Fig. 2.3), making $\sigma(f_{\rm NL}^{\rm local}) \simeq 1$ a compelling target. *Planck* gives a constraint of $f_{\rm NL}^{\rm local} = 0.8 \pm 5\,(1\sigma)$ [39], and further measurements of the CMB alone cannot improve on this constraint by more than a factor of 2–3. However, it has been shown that correlating large-scale structure tracers that have different clustering bias factors can enhance the signature of non-Gaussianity [40–42]. Fig. 2.3 shows expected constraints from correlations between the PICO lensing potential maps (§ 2.3.2) and LSST galaxies. For $f_{\rm NL}^{\rm local} = 2$, 3σ evidence will be reached if large angular scale ($L \geq 8$)[2] auto- and cross-correlation spectra can be used. If LSST's auto-correlation can only be used on smaller angular scales $L \geq 20$, the 3σ evidence weakens to 2σ.

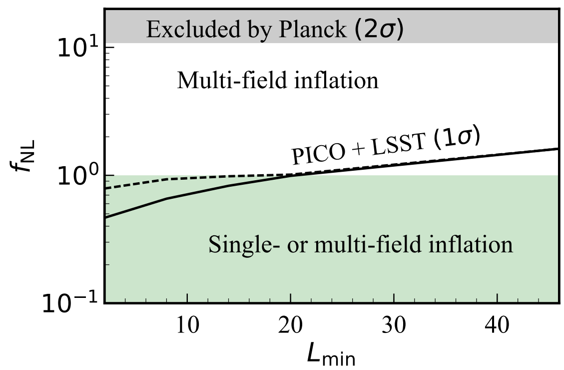

Figure 2.3: Cross-correlating PICO's lensing potential map with LSST galaxies will allow detecting or excluding $f_{\rm NL}^{\rm local} = 2$ with 3σ evidence if the data can be used at angular scales $L \geq 8$ (solid black). A detection above $|f_{\rm NL}^{\rm local}| = 1$ indicates that inflation is driven by multiple fields; single-field inflation has $|f_{\rm NL}^{\rm local}| < 1$ (green region). The *Planck* constraint is $f_{\rm NL}^{\rm local} < 10.8\,(2\sigma)$. The cross-correlations will allow excluding or detecting $f_{\rm NL}^{\rm local} = 2\,(2\sigma)$ if LSST data are used only for $L \geq 20$ (dash). Fig. 2.8 gives the assumptions for the LSST data.

2.2.2 Fundamental Particles: Light Relics, Dark Matter, and Neutrinos

• **Light Relics** In the inflationary paradigm, the Universe was reheated to temperatures of at least 10 MeV and perhaps as high as 10^{12} GeV. At these high temperatures, even very weakly interacting or very massive particles, such as those arising in extensions of the Standard Model of particle physics, can be produced in large abundances [43, 44]. As the Universe expands and cools, the particles fall out of equilibrium, an event referred to as 'decoupling', and characterized by a decoupling temperature T_F. The decoupling leaves observable signatures in the CMB power spectra. Through these effects the CMB is a sensitive probe of neutrino and other particles' properties.

One particularly compelling target is the effective number of light relic particle species $N_{\rm eff}$. The canonical value with three neutrino families is $N_{\rm eff} = 3.046$. Additional light particles contribute a change $\Delta N_{\rm eff}$ that is a function only of the decoupling temperature and the spin of the particle, g. The magnitude of $\Delta N_{\rm eff}$ is quite restricted, even for widely varying decoupling temperatures T_F. A range $0.027\,g \leq\ \Delta N_{\rm eff} \leq 0.07\,g$ corresponds to a range in T_F spanning decoupling during post-inflation reheating ($0.027g$) down to lower T_F with decoupling occurring just prior to the QCD phase transition ($0.07g$).

Information about $N_{\rm eff}$ is gleaned primarily from the TT, TE, and EE power spectra. For an experiment like PICO, which has sufficient resolution to reach a cosmic-variance-limited measurement[3] of EE up to $\ell = 2300$, the two additional most important parameters for improving constraints are the fraction of sky observed, $f_{\rm sky}$, and the noise (Fig. 2.4, left). The PICO baseline will use data from 70% of the sky to constrain $\Delta N_{\rm eff} < 0.06\,(95\%)$ (S04).[4] This constraint, which is a factor of 4.7 improvement relative to *Planck* ($\Delta N_{\rm eff} < 0.28$, 95%) and will not be matched by any currently funded effort, opens up a new range of temperatures in which to detect the signature of light relic species. If no new species are detected, then the lowest temperature T_F at which any vector particle could have fallen out of equilibrium will move up by a factor of 400 (Fig. 2.4, right).

While our theoretical target for $N_{\rm eff}$ is defined by particles that decoupled long before neutrinos did, there are a number of well-motivated scenarios in which the thermal evolution of the Standard Model is

[2] L refers to multipoles in galaxy clustering fields and in CMB lensing (§ 2.3.2), in contrast to the use of ℓ for the CMB itself.

[3] A measurement is cosmic-variance-limited when the measurement uncertainty is dominated by the statistics of observing the finite number of Fourier modes available in our Universe.

[4] The CMB EE and the Galactic foregrounds EE and BB spectra are comparable in level (Fig. 2.1). With 21 frequency bands PICO should be able to separate signals at the mild levels necessary for 70% of the sky (§ 2.7).

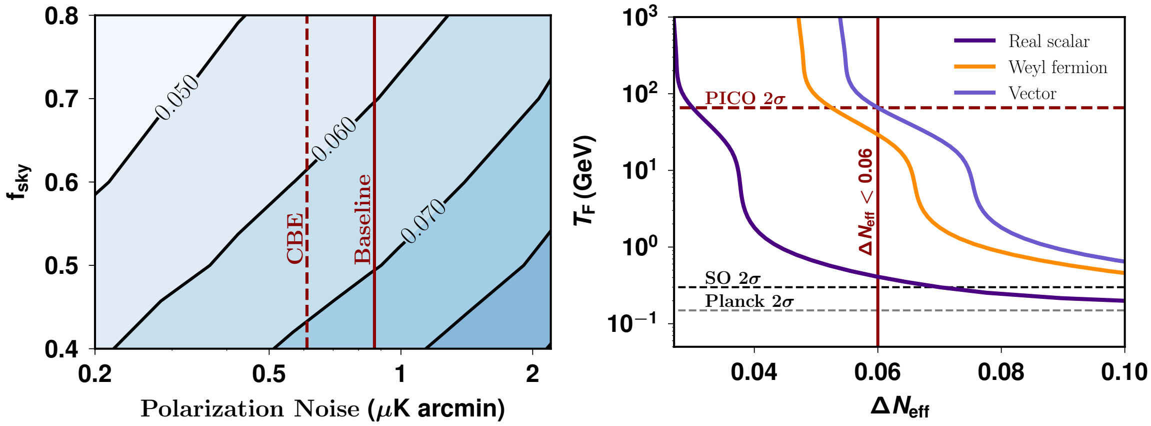

Figure 2.4: PICO will achieve a constraint $\Delta N_{\rm eff} < 0.06\,(95\%)$ (left, 2σ contours shown) in the baseline configuration (vertical solid) using its cosmic-variance-limited measurement of EE for $\ell \leq 2300$, and 21 frequency bands to utilize data over 70% of the sky ($5'$ resolution assumed). This constraint translates to moving up the lowest decoupling temperature T_F for vector, Weyl fermion, and scalar particles by factors of 400, 200, and 6, respectively, relative to *Planck* (right, dashed black, only T_F for vector particle is shown). We also show the projected vector particle limit for the Simons Observatory [32].

altered after the time of neutrino decoupling. These scenarios will change the relationship between $N_{\rm eff}$ as measured in the CMB and the value of $N_{\rm eff}$ that affects the primordial abundance of the helium fraction Y_p as inferred from big bang nucleosynthesis calculations. For example, the decay of a thermal relic into photons after nucleosynthesis would reduce $N_{\rm eff}$ in the CMB but could leave Y_p unaltered from its Standard Model value. PICO will make a simultaneous measurement of $N_{\rm eff}$ and Y_p with $\sigma(N_{\rm eff}) = 0.08$ and $\sigma(Y_p) = 0.005$, giving a 2% uncertainty on the value of Y_p. These uncertainties are equivalent to those available with other astrophysical measurements, but the systematic uncertainties are entirely different. Systematic uncertainties currently limit our knowledge of Y_p.

• **Dark Matter** Cosmological measurements have already confirmed the existence of one relic that lies beyond the Standard Model: dark matter. CMB experiments are effective in constraining dark matter candidates in the lower mass range, which is not available for terrestrial direct detection experiments [45, 46].

Interactions between dark matter and protons in the early Universe create a drag force between the two cosmological fluids, damping acoustic oscillations and suppressing power in density perturbations on small scales. As a result, the CMB temperature, polarization, and lensing power spectra are suppressed at high multipoles relative to a Universe without such drag forces. This effect has been used to search for evidence of dark-matter–proton scattering over a range of masses, couplings, and interaction models [47–54], to test the possibility of an interacting dark-matter sub-component [53], and to provide consistency tests of dark matter in the context of the anomalous 21-cm signal reported by the EDGES collaboration [53, 55–57].

PICO's constraining power comes primarily from making high SNR maps of the lensing-induced deflections of polarized photons, which are discussed in Section 2.3. For a spin-independent velocity-independent contact-interaction, chosen as our fiducial model, PICO will improve upon *Planck*'s dark matter cross-section constraints by a factor of 25 over a broad range of candidate masses that are largely unavailable for traditional direct detection experiments (Fig. 2.5, right).

The axion is another dark matter candidate that is well motivated by string theory [59] and that is consistent with straightforward extensions of the Standard Model of particle physics [60–62]. For an axion mass in the intermediate range $10^{-30} < m_a < 10^{-26}$ eV, current measurements constrain its fraction to be $\leq 2\%$ (1σ) of the total dark-matter density. If 2% of the total dark content is made of axions, PICO's measurement of the TT, TE and EE spectra with additional constraints from the lensing reconstruction will detect this species at between 7 and 13σ depending on the mass range. This is an average improvement of a factor of 10 relative to *Planck*.

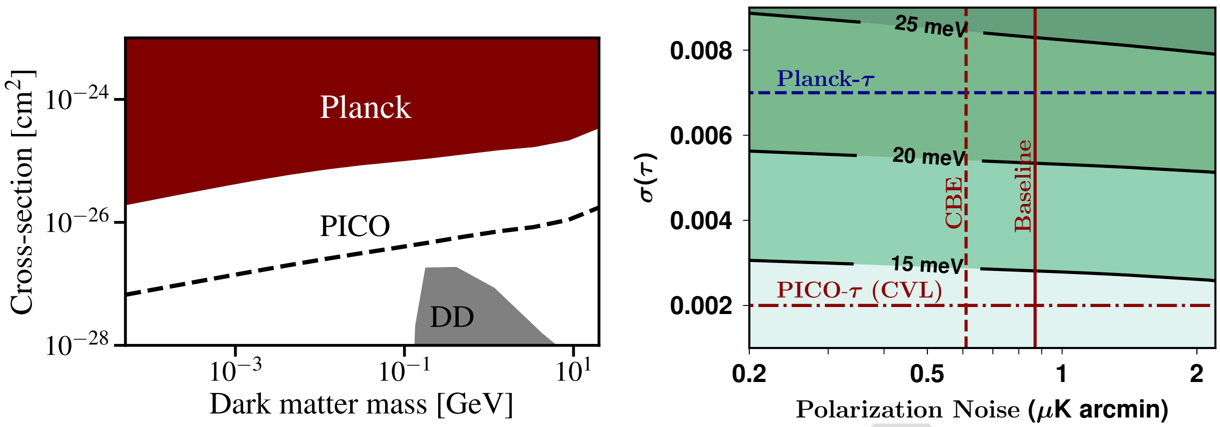

Figure 2.5: **Left:** PICO will give a factor of 25 more stringent constraint on spin-independent velocity-independent dark matter scattering cross-section (dashed) relative to current *Planck* 95% confidence limit (red) [50]. Terrestrial direct detection experiments are expected to give complementary and stronger constraints, but only for the higher dark matter masses (grey) [58]. **Right:** Using cosmic-variance-limited (CVL) measurement of τ, $\sigma(\tau) = 0.002$, BAO information from DESI, and 21 frequency bands to separate foregrounds over 70% of the sky, PICO will reach $\sigma(\Sigma m_\nu) = 14$ meV (contours) giving at least 4σ detection of the minimal expected sum of neutrino masses $\Sigma m_\nu =$ 58 meV.

• **Neutrino Mass** The origin and structure of the neutrino masses is one of the great outstanding questions about the nature of the Standard Model particles. Cosmology offers a measurement of the sum of the neutrino masses $\sum m_\nu$ through the gravitational influence of the non-relativistic cosmic neutrinos. The current measurement of $N_{\rm eff} = 2.99 \pm 0.17$ [63] already confirms the existence of these neutrinos at $> 10\sigma$ and their mass implies that they will contribute to the matter density at low redshifts. The best current mass constraint arises from a combination of *Planck* and BOSS BAO giving $\sum m_\nu < 0.12$ eV (95%) [63].

Cosmological measurements are primarily sensitive to the suppression of power on small scales after the neutrinos become non-relativistic, which can be measured via CMB lensing (§ 2.3.2), or weak lensing in galaxy surveys. However, these measurements are limited by our knowledge of the amplitude of the primordial fluctuation power spectrum A_s because they only constrain the combination $A_s e^{-2\tau}$, where τ is the optical depth to reionization. Although many astrophysical surveys hope to detect $\sum m_\nu$, any detection of the minimum value expected from particle physics, $\sum m_\nu = 58$ meV, at more than 2σ will require a better measurement of τ.

The strongest constraints on τ come from the EE spectrum at $\ell < 10$, which requires measurements over the largest angular scales and good separation of Galactic foreground sources of emission. The best current measurement with $\sigma(\tau) = 0.007$ is from *Planck* [63]. With this uncertainty in τ one is limited to $\sigma(\sum m_\nu) \gtrsim 25$ meV, after including forthcoming BAO information (Fig. 2.5, right); no other survey or cosmological probe will improve this constraint, unless a more accurate measurement of τ is made. One of the S3 experiments is attempting to measure the lowest ℓ's and improve upon the *Planck* precision by a factor of about two [38]. A space mission with its access to the entire sky and broad frequency coverage is the most suitable platform for the measurement (§ 2.7 and § 2.9). PICO will reach the cosmic-variance limit uncertainty on τ, $\sigma(\tau) = 0.002$ (§ 2.3.1), and using its deep CMB lensing map (§ 2.3.2) will therefore reach $\sigma(\sum m_\nu) = 14$ meV when combined with measurements of BAO from DESI or Euclid [64] This measurement will give a 4σ detection of the minimum sum (SO3).

2.2.3 Fundamental Fields: Primordial Magnetic Fields and Cosmic Birefringence

• **Primordial Magnetic Fields** One of the long-standing puzzles in astrophysics is the origin of observed 1–10 μG galactic magnetic fields [65]. Producing such fields through a dynamo mechanism requires a primordial seed field [66]. Moreover, μG-strength fields have been observed in proto-galaxies that are too young to have gone through the number of revolutions necessary for the dynamo to work [67]. A primordial magnetic field (PMF), present at the time of galaxy formation, could provide the seed or even eliminate the need for the dynamo altogether. Specifically, a 0.1 nG field in the intergalactic plasma would be adiabatically compressed in the collapse to form a $\sim$1 μG galactic field [68]. PMFs could have been generated in the aftermath of phase transitions in the early Universe [69], during inflation [70, 71], or at the end of inflation [72]. A detection of PMFs with the CMB would be a major discovery as it would establish the magnetic field's primordial origin, signal new physics beyond standard models of particle physics and cosmology, and discriminate among different theories of the early Universe [73–75].

The current CMB bounds on PMF strength are $B_{1\,\mathrm{Mpc}} < 1.2$ nG at 95% CL for the scale-invariant PMF spectrum [76–79], based on measurements of the TT, TE, EE and BB spectra.[5] The much more accurate measurement of BB by PICO would only marginally improve the PMF bound because CMB spectra scale as $B^4_{1\,\mathrm{Mpc}}$. However, Faraday rotation provides a signature that scales linearly with the strength of PMF [80]. It converts CMB E modes into B modes, generating mode-coupling EB and TB correlations. So far this signature has been out of reach because prior experiments did not have sufficient sensitivity. Using Faraday rotation, PICO will probe PMFs as weak as 0.1 nG (1σ), a precision that already includes the effects of imperfect lensing subtraction, Galactic foregrounds [81–83], and other systematic effects. With this precision, which is a factor of five stronger than achievable with S3 experiments, PICO can conclusively rule out the purely primordial (i.e., no-dynamo driven) origin of the largest galactic magnetic fields.

• **Cosmic Birefringence** A number of well-motivated extensions of the Standard Model involve (nearly) massless axion-like pseudo-scalar fields coupled to photons via the Chern-Simons interaction term [84–87]. These couplings also generically arise within quintessence models for dark energy [86], chiral-gravity models [88], and models that produce parity-violation during inflation [89]. Regardless of the source of the parity-violating coupling, its presence may cause cosmic birefringence – a rotation of the polarization of an electromagnetic wave as it propagates across cosmological distances [86, 90, 91]. Cosmic birefringence converts primordial E-modes into B-modes, producing TB and EB cross-correlations whose magnitude depends on the statistical properties of the rotation field in the sky [92–94]. Previous studies have constrained both a uniform rotation angle as well as anisotropic rotation described by a power spectrum [94]. The current bound on a uniform angle is $30'$ (68%) [95], and the bound on the amplitude of a scale-invariant rotation angle spectrum, which could be caused by fluctuations in a light pseudo-scalar field present during inflation [96], is 0.11 deg^2 (95%) [97]). Using the combination of five bands in the 70–156 GHz range, PICO will reduce the 95% CL bound on the uniform rotation angle by a factor of 300, to $0.1'$. The 95% CL bound on the amplitude of a scale-invariant rotation spectrum will be reduced by a factor of 275 to 4×10^{-4} deg^2, giving important constraints on string-theory-motivated axions [96, 98].

2.3 Cosmic Structure Formation and Evolution

2.3.1 The Formation of the First Luminous Sources

A few hundred million years after the Big Bang, the neutral hydrogen gas permeating the Universe was reionized by photons emitted by the first luminous sources to have formed. The nature of these sources and the exact history of this epoch are key missing links in our understanding of structure formation (SO5).

The reionization of the Universe imprints multiple signals in the temperature and polarization of the CMB. In polarization, the most important signature is an enhancement in the EE power spectrum at large angular scales $\ell \lesssim 10$ (Fig. 2.1). This signal gives a direct measurement of the optical depth to the reionization epoch τ and thus to the mean redshift of reionization z_{re}, with very little degeneracy with other cosmological parameters (Fig. 2.6).[6] *Planck*'s determination of the optical depth to reionization $\tau = 0.054 \pm 0.007\,(1\sigma)$ has indicated that reionization concluded by $z \sim 6$, but the measurement uncertainty leaves many unanswered questions including: were the ionizing sources primarily star-forming galaxies or more exotic sources such

[5] It is conventional to quote limits on the PMF strength smoothed over a 1 Mpc region in comoving units, i.e., rescaled to $z = 0$: $\mathbf{B}_{\mathrm{today}} = a^2\mathbf{B}(a)$.

[6] The mean redshift to reionization is the redshift when 50% of the cosmic volume was reionized.

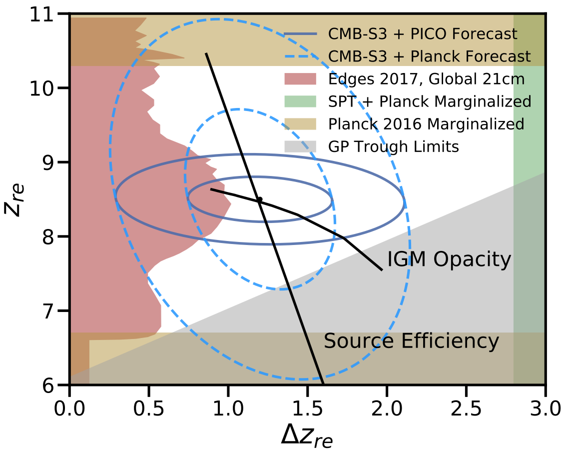

Figure 2.6: Contours of 1σ and 2σ constraints on the mean redshift and duration of reionization using PICO and CMB-S3 data (solid dark blue), and comparison with *Planck* and CMB-S3 (dash light blue). Source efficiency and IGM opacity (dark lines) are two physical parameters controlling the reionization process in current models. The PICO measurements, together with higher-resolution data of the kSZ effect, will significantly constrain the range of models allowed. We also include other constraints from *Planck*, EDGES, the Gunn–Peterson (GP) trough, and *Planck* + the South Pole Telescope [63, 99–101].

as supermassive black holes or annihilating dark matter? What was the mean free path of ionizing photons during this epoch? What was the efficiency with which such photons were produced by ionizing sources? Did the reionization epoch extend to $z \sim 15$–20, as has been claimed recently [102]? With ten independent maps of the entire sky, multiple frequency bands and ample sensitivity to remove foregrounds, PICO is uniquely suited to make the low ℓ EE-spectrum measurements, reach cosmic-variance-limited precision with $\sigma(\tau) = 0.002$, settle some of these questions, and significantly constrain the others (SO5).

Figure 2.6 presents forecasts for reionization constraints in the $z_{\rm re} - \Delta z_{\rm re}$ parameter space. These are obtained from PICO's measurement of τ in combination with S3 experiments' measurements of the "patchy" kinematic Sunyaev–Zeldovich (kSZ) effect, due to the peculiar velocities of free-electron bubbles around ionizing sources [103]. The figure includes curves of constant efficiency of production of ionizing photons in the sources, and of intergalactic-medium opacity, two parameters that quantify models of reionization. The curves shown are illustrative; families of models, that would be represented by parallel 'source efficiency' and 'IGM Opacity' lines, are allowed by current data. PICO's data will give simultaneous constraints on these physical parameters, yielding important information on the nature of the first luminous sources. For example, models in which the first sources are quasars rather than galaxies have significantly different IGM opacities and source efficiencies.

The process of reionization leaves specific non-Gaussian signatures in the CMB. In particular, patchy reionization induces non-trivial 4-point functions in both temperature and polarization [104, 105]. The temperature 4-point function can be used to separate reionization and late-time kSZ contributions. Combinations of temperature and polarization data can be used to build quadratic estimators for reconstruction of the patchy τ field, analogous to CMB lensing reconstruction (§ 2.3.2). These estimators generally require high angular resolution, but also rely on foreground-cleaned CMB maps. Data from PICO's high-frequency bands – which have better than 2 arcmin resolution and cover frequencies that are not suitable for observations from the ground – will enable these estimators to be robustly applied to high-resolution ground-based CMB data, a strong example of ground-space complementarity.

Decreasing the uncertainty on τ is important to break the degeneracy between this parameter and the amplitude of the primordial power spectrum $A_{\rm s}$, a degeneracy in the CMB power spectra that hinders all cosmological observables of the growth of structure (§ **??**). The degeneracy can only be broken through measurements of the low-ℓ EE power spectrum. PICO's cosmic-variance-limited polarization measurements will thus improve constraints on the sum of neutrino masses, dark energy, and modified gravity coming from all low-z growth measurements including galaxy lensing, velocity-field measurements, redshift-space distortions, and galaxy surveys.

2.3.2 Probing the Evolution of Structures via Gravitational Lensing and Cluster Counts

The particle content of the Universe, gravitational collapse, the effects of dark energy, and energetic feedback processes that recycle energy determine the evolution of structures in the Universe. The amplitude of linear fluctuations as a function of redshift, parameterized by $\sigma_8(z)$, is thus a sensitive probe representing the effects of physical processes affecting growth. CMB photons are affected by, and thus probe, $\sigma_8(z)$ as they traverse the entire Universe. PICO will tightly constrain $\sigma_8(z)$ through measurements of gravitational lensing and cluster counts.

• **Gravitational Lensing** Matter between us and the last-scattering surface deflects the path of photons through gravitational lensing, imprinting the three-dimensional matter distribution across the volume of the Universe onto the CMB maps. The specific quantity being mapped by the data is the projected gravitational potential ϕ that is lensing the photons. From the lensing map, which receives contributions from all redshifts between us and the CMB, with the peak of the distribution at $z \sim 2$, we infer the angular power spectrum $C_L^{\phi\phi}$ (Fig. 2.7). Both the temperature and polarization maps of the CMB, and by extension the angular power spectra, are affected by lensing.

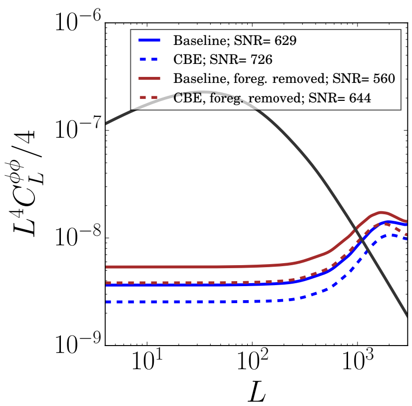

Figure 2.7: PICO will make a high SNR full-sky map of the projected gravitational potential ϕ due to all matter between us and the last scattering surface at all angular scales $2 \le L \lesssim 1000$ (Footnote 2) for which its noise (red and blue) is below the theoretically predicted power spectrum $C_L^{\phi\phi}$ (black). Noise predictions as a function of L and anticipated SNR values for the measurement of $C_L^{\phi\phi}$ are given for the baseline (solid) and CBE (dashed) cases, and without (blue) and with (red) a process of foregrounds separation, which degrades the SNR by $\sim$10 %.

Planck's ϕ map had SNR of $\sim$1 per L mode over a narrow range of scales, $30 < L < 50$. PICO will make a true map, with SNR $\gg 1$ for each mode in the range $2 \le L \lesssim 1000$. While *Planck* had an SNR of 40 integrated across the entire $C_L^{\phi\phi}$ power spectrum [*106*], PICO will give SNR of 560 and 644 for the baseline and CBE configurations, respectively; both values already account for foreground separation (Fig. 2.7).

PICO's ϕ map is a key ingredient in the delensing process that improves constraints on r (§ 2.2.1) and in extracting neutrino mass constraints (§ 2.2.2). It will also be used to constrain the properties of quasars and other high-redshift astrophysics. For example, cross-correlations with quasar samples from DESI will yield a precise determination of the quasar bias (and hence host halo mass) as a function of the quasar properties, such as (non-)obscuration. Such studies are not possible with any other lensing techniques, due to their sensitivity to lower redshifts.

• $\sigma_8(z)$ **from Gravitational Lensing** Cross-correlations between the PICO lensing-potential map and wide-field samples of galaxies and quasars provide a powerful technique to measure the time dependence of the amplitude of matter fluctuations $\sigma_8(z)$ in tomographic redshift bins. This is achieved by overcoming the limitations of auto-correlations of these data sets: The lensing ϕ map is sensitive to the projection of all matter back to the last scattering surface, so it cannot resolve the time dependence of fluctuations, while galaxies and quasars trace matter in an unknown biased way so that the matter amplitude cannot be determined. Cross-correlations of the two data sets, broken down to several tomographic redshift bins, will constrain how galaxies in each bin trace the dark matter, which will yield strong constraints on $\sigma_8(z)$ and thereby on structure formation and models of dark energy and modified gravity [*40*, *41*].

In the left panel of Fig. 2.8 we show projected 1σ errors on $\sigma_8(z)$ when using cross-correlations with LSST's gold sample of galaxies [*107*]. Sub-percent accuracy is obtainable with PICO's resolution which will

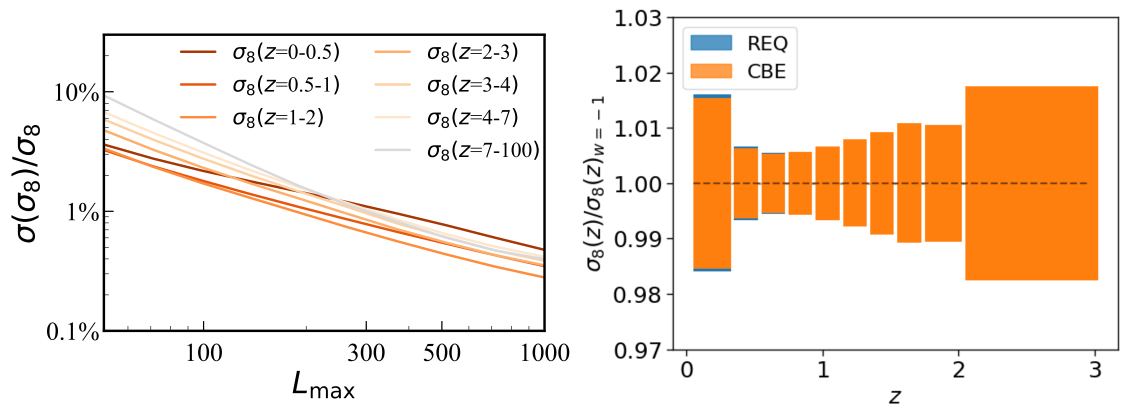

Figure 2.8: Sub-percent constraints on the evolution of σ_8 as a function of redshift will come from two independent PICO products: Correlations between PICO's deep gravitational lensing map (Fig. 2.7) and LSST's gold sample of galaxies (left) and cluster counts (right). Fractional uncertainties in σ_8 relative to fiducial ΛCDM values are given as a function of the finest angular scale $L_{\max}$ of the correlation analysis for seven redshift bins (left). The baseline and CBE configurations give essentially the same fractional errors of $\sigma_8(z)$ using cluster counts (right). LSST assumptions: 10 years, 50% sky fraction, 55 galaxies per arcmin^2 at redshift $z < 3$ with magnitude limit $i < 25.3$ [*107*], and dropout galaxies at $z > 3$ [*109*] extrapolating recent Hyper Suprime-Cam observations [*110*–*112*], with linear bias $b(z) = 1 + z$.

give information extending to $L = 1000$.[7] This accuracy will be used to constrain dark energy or modified gravity, in the context of specific models, and to give a neutrino mass constraint that is independent from and competitive with that inferred from the CMB lensing auto-power spectrum (§ 2.2.2) [*108*] .

• **Cluster Counts** The distribution of galaxy clusters in redshift is one consequence of the evolution of structures and is thus a sensitive measure of $\sigma_8(z)$. The observational quantity of interest is $dN/(dz\,dm)$, the number of observed clusters per redshift and per mean mass, from which constraints on $\sigma_8(z)$ can be derived. Galaxy clusters found by PICO via the thermal Sunyaev–Zeldovich (tSZ) effect (§ 2.3.3) provide a catalog with a selection function that is simple to model and thus straightforward to use for cosmological inference. PICO's catalog will provide all clusters with masses above $\sim 3 \times 10^{14} M_\odot$ out to redshifts $z \sim 3$, as long as the clusters have started to virialize. We forecast that PICO will find ∼150,000 galaxy clusters, assuming the cosmological parameters from *Planck* and using the 70% of sky not obscured by the Milky Way. Redshifts will be provided by future optical and infrared surveys. Cluster masses will be inferred by optical weak lensing for clusters with $z < 1.5$ and by PICO's own CMB halo lensing data at higher redshifts (see next paragraph). This catalog will provide σ_8 with sub-percent precision for $0.5 < z < 2$ (Fig. 2.8, right), and a neutrino mass constraint $\sigma(\sum m_\nu) = 14$ meV that is independent from the one coming from the combination of optical depth and lensing measurements (SO3, § 2.2.2).

Calibrating the masses of clusters, that is determining $m(z)$, is the most uncertain step in inferring σ_8 and other cosmological parameters using cluster counts. PICO will provide calibration using 'CMB halo lensing', an approach that uses the small-scale effects of gravitational lensing due to dark matter halos around clusters and proto-clusters [*113*–*115*]. The technique is particularly effective for measuring halo masses out to high redshifts where gravitational lensing of background objects no longer works because there are no background sources. The approach is illustrated in Fig. 2.9, which gives the 1σ uncertainty in a halo mass measurement as a function of the object's redshift. PICO will measure the mass of individual low-mass clusters ($\sim 10^{14}$ M$_\odot$) over a wide redshift range, and by stacking will determine the mean mass of smaller halos, with masses of $\sim 10^{13}$ M$_\odot$, which include those hosting individual galaxies. Because the vast majority of clusters have masses that are larger than $\sim 10^{14}$ M$_\odot$, the PICO data will provide mass calibration for all objects of interest. The flattening at high redshift reflects the fact that the technique is sensitive over

[7] PICO's resolution is sufficient to give information for $L > 1000$, but at these scales structures are non-linear and will not be used to constrain $\sigma_8(z)$.

a broad range of redshifts. The high-frequency PICO data, for which the resolution matches ground-based instruments' resolution at lower frequencies, will play an essential role in cleaning foregrounds, particularly those derived from the temperature-based estimator, which is most contaminated by foregrounds.

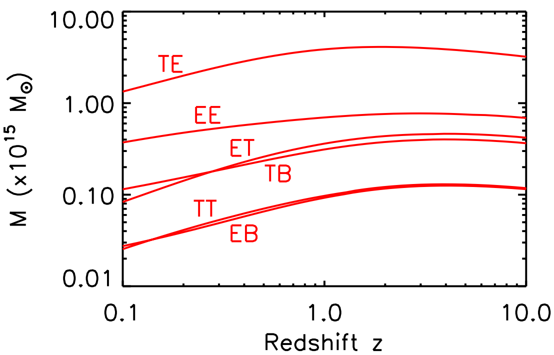

Figure 2.9: PICO will provide mass calibration for individual clusters and proto-clusters with mass as low as $10^{14} M_\odot$ at $z > 2$ using 'halo lensing'. Curves for different CMB signal correlations (red) give the 1σ sensitivity of an optimal mass filter [116] as a function of z. The curves are flat at high redshift, demonstrating that the technique probes a broad range of redshifts. For PICO, the EB and TT estimators are equivalent, offering important cross-validation of measurements because the systematics are very different for temperature and polarization.

Beyond its role in calibrating masses for cluster counts, PICO's halo lensing measurements will also be a unique tool for measuring the relation between galaxies and their dark matter halos during the key epochs of cosmic star formation at $z \geq 2$, which is not reachable by other means. This will provide valuable insight into the role of environment on galaxy formation during the rise to and fall from the peak of cosmic star formation at $z \sim 2$.

2.3.3 Constraining Feedback Processes through the Sunyaev–Zeldovich Effect

Not all CMB photons propagate through the Universe freely; about 6% are Thomson-scattered by free electrons in the intergalactic medium (IGM) and intercluster medium (ICM). These scattering events leave a measurable imprint on CMB temperature fluctuations, which thereby contain a wealth of information about the growth of structures and the thermodynamic history of baryons. A fraction of these photons are responsible for the thermal and kinetic Sunyaev–Zeldovich effects (tSZ and kSZ) [117, 118]. The amplitudes of the tSZ and kSZ signals are proportional to the integrated electron pressure and momentum along the line of sight, respectively. They thus contain information about the thermodynamic properties of the IGM and ICM, which are highly sensitive to astrophysical feedback. Feedback is the process of energy injection into the IGM and ICM from accreting supermassive black holes, supernovae, stellar winds, and other sources. Feedback processes are the most uncertain, yet crucial, ingredient in modern theories of galaxy formation; they are required in order to match observations of the stellar properties of galaxies, but the underlying details of the physical processes involved are still highly uncertain.

Multifrequency CMB data also allow the reconstruction of full-sky 'Compton-y maps' of the tSZ signal. With low noise and broad frequency coverage, which is essential for separating out other signals, PICO will yield a definitive Compton-y map over the full sky, with a total SNR of 1270 for the CBE and $\approx 10\%$ lower for the baseline configurations (Fig. 2.10). This is nearly two orders of magnitude higher SNR than *Planck*, which already gave data with much higher SNR than ground-based experiments. The tens of thousands of clusters forecast to be detected by PICO will be found in the y map (§ 2.3.2).

Strong constraints on models of astrophysical feedback will be obtained from the analysis of the PICO y-map, both from its auto-power spectrum and from cross-correlations with galaxy, group, cluster, and quasar samples. As an example, we forecast the detection of cross-correlations between the PICO y-map and galaxy weak-lensing maps constructed from LSST and WFIRST data. Considering the LSST gold weak-lensing sample, with a source density of 26 galaxies/arcmin^2 covering 40% of the sky, we forecast a detection of the tSZ–weak-lensing cross-correlation with SNR = 3000. Cross-correlations with the galaxies themselves will be measured at even higher SNR. At this immense significance, the signal can be broken down into dozens of tomographic redshift bins, precisely tracing the evolution of thermal pressure over cosmic time. For PICO and WFIRST (assuming 45 galaxies/arcmin^2 covering 5.3% of the sky), we forecast SNR = 1100

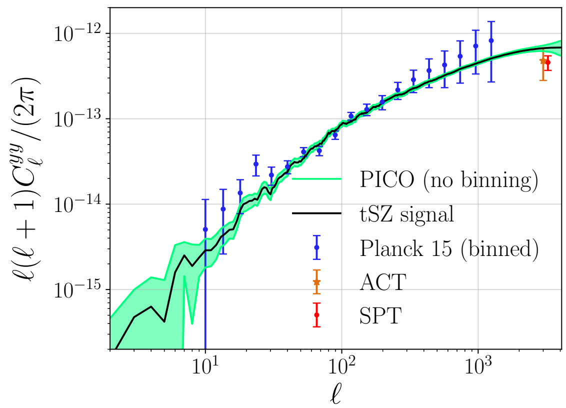

Figure 2.10: The PICO y-map will give a tSZ power spectrum with an SNR of 1270 (green, 1σ per ℓ mode), which is nearly 100 times larger than from *Planck* (blue). Binning the data (not shown) as was done for *Planck* would further increase the SNR. We include current measurements by the ground-based SPT and ACT [*119*, *120*]. In these forecasts we reconstruct the Compton-y field from maps that include Galactic foregrounds, CMB fluctuations, and PICO CBE noise using the needlet internal linear combination algorithm [*121*]. The input maps use the *Planck* sky model [*122*].

for the tSZ-weak lensing cross-correlation. The WFIRST galaxy sample extends to higher redshift, and thus this high-SNR measurement will allow the evolution of the thermal gas pressure to be probed to $z \approx 2$ (the peak of the cosmic star formation history) and beyond. These measurements will revolutionize our understanding of galaxy formation and evolution by distinguishing between models of feedback energy injection at high significance. Additional cross-correlations of the PICO y-map with quasar samples, filament catalogs, and other large-scale structure tracers will provide valuable information on baryonic physics that is complementary to inferences from the lensing cross-correlations described earlier.

2.4 Testing ΛCDM

The current cosmological model, as encoded by ΛCDM, provides a reasonably good fit to current data. A host of cosmological observations including the CMB fit within the model that consists of only six parameters [*28*]. But the model is phenomenological and it leaves fundamental questions open. Premier among them is the unknown content of the majority of the Universe. Approximately 95% of the Universe appears to be composed of dark matter and dark energy of unknown nature, both of which are necessary to explain observations at scales ranging from that of a galaxy to that of the Hubble volume. Yet, there are no detection of dark matter particles, and as for dark energy, it even lacks a compelling theoretical motivation.

In this context, tension between measurements of any ΛCDM parameter obtained by different probes compel additional stringent tests and investigation of alternatives to the prevailing paradigm. Examples of emerging tensions are the 3.5σ?? need value and reference discrepancy between the CMB- and supernovae-based measurements of the Hubble constant [**?**]; and the 2.5σ?? need value and reference discrepancy between *Planck* and weak lensing surveys in the measurement of the amplitude of late time perturbations σ_8. Such tensions, while perhaps only indicating the presence of systematic effects in the measurements, may in fact point toward new physics. One way to search for new physics is to better constrain the current measurements and to test for extensions beyond the base six-parameter set.

Given PICO's baseline noise and angular resolution, and an input set of N fiducial ΛCDM parameters, it is straightforward to calculate the uncertainty with which PICO will constrain this set [*123*]. A figure of merit (FOM) that quantifies the strength of the constraint is the volume of the uncertainty region in the N-dimensional space [**?**].[8] The FOM is defined such that a larger value linearly corresponds to *smaller* volume and thus to smaller parameter errors. what else are we including? delensing? foreground separation? Can we point to other papers in which this specific code and FOM have been used? what 'cmb' information is used? only spectra? what about phi? Can we invert the FOM? it is more intuitive to have smaller numbers correspond to smaller volumes.

The six-parameter ΛCDM model that is constrained by current measurements includes the baryon density, the dark matter density, the amplitude and spectral index of a power-law spectrum of initial perturba-

[8]The FOM is determined by the covariance of the Fisher information matrix, $\mathrm{FoM} = (\det[\mathrm{cov}(p_i)])^{-1/2}$, $i = 1,\ldots,N$, where p is the parameter set.

tions, the angular scale of acoustic oscillations, and the optical depth to reionization. To this set we added: N_{eff} the effective number of light relics (§ 2.2.2), two dark energy parameters[9] need to fill footnote, the tensor to scalar ratio r (§ 2.2.1), the sum of neutrino masses $\sum m_\nu$ (§ 2.2.2), and α_1 is this running?. For this 12-parameter set and for the PICO baseline configuration we find that the FOM is 3×10^9 larger than that calculated for *Planck*. For the CBE the value increases to 9.5×10^9. Excluding an inflationary signal by fixing $r=0$, the values are 5×10^6 and 7×10^6. Even stronger improvements will be obtained when the PICO CMB data will be combined with available data sets in the next decade including weak lensing, BAO, and cluster of galaxies.

These improvements will test ΛCDM so stringently that it is hard to imagine it surviving such a scrutiny if it is not fundamentally correct. It would be equally exciting if ΛCDM failed and a new cosmological model emerged.

2.5 Galactic Structure and Star Formation

Planck enabled an immense step forward in Galactic astrophysics [124]. With seven full-sky polarization maps at frequencies between 30 and 353 GHz and a highest resolution of 5′, *Planck* provided entirely new and surprising data about the structure of the interstellar medium (ISM); the data have a lasting legacy for the foreseeable future. PICO will provide an even greater leap forward. It will produce 21 polarization maps of Galactic emission, and in the bands already probed by *Planck* they will be much deeper; for example, PICO's map at 321 GHz will be 105 times deeper than *Planck*'s mean map depth at 353 GHz, and PICO's map at 30 GHz will be 17 times deeper than *Planck*'s. At 799 GHz PICO will have five times the resolution of *Planck*'s highest resolution map (Fig. 2.11). Such a data set can only be obtained from space. These data will complement a rich array of other polarization observations forthcoming in the next decade, including stellar polarization surveys to be combined with Gaia astrometry, and Faraday rotation measurements from observations at radio wavelengths with the Square Kilometer Array (SKA) and its precursors.

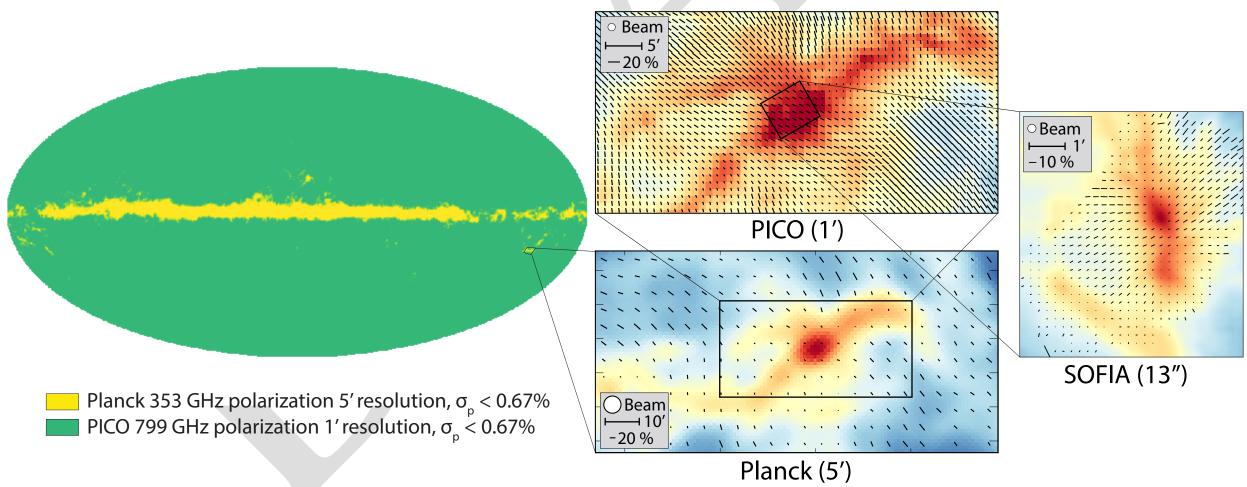

Figure 2.11: *Planck*'s 353 GHz polarization map gave a resolution of 5′ and sensitivity to polarization intensity of $\sigma_p < 0.67\%$ over a small portion of the sky (left, yellow). At 799 GHz, the PICO baseline mission will give a polarization map of the *entire sky* and with 5 times higher resolution (left, green). The *Planck* map of the Orion region overlaid with vectors that are aligned with the inferred magnetic field (lower panel), and a simulated PICO observation (upper panel) illustrate the leap in information content (vector lengths are proportional to polarization fraction). With this map, and maps at other frequencies, PICO will characterize Galactic magnetized turbulence at scales spanning the diffuse ISM down to dense star forming cores, which will be mapped with high-resolution polarimetry by instruments such as HAWC+/SOFIA [125] (right panel) and ALMA [126].

While the PICO data will likely provide many new insights and surprises, we focus here on two particularly important science objectives that are integral to NASA's science goal to explore how the Universe

[9] give dark energy parametrization

evolved; they relate to the structure and evolution of the Milky Way. These science objectives can only be achieved by the PICO dataset.

(1) *Test models of the composition of interstellar dust:* Less than 1 μm in size, dust grains are intermediate in the evolution from atoms and molecules to large solid bodies such as comets, asteroids, and planets. Encoded in the composition of dust are the pathways through which grains formed and grew. Dust grains also participate directly in interstellar chemistry, for example by catalyzing the formation of H_2 and organic molecules on their surfaces, in ways that depend upon their chemical makeup. Thus, the composition of dust grains is an essential aspect of the chemical evolution of interstellar matter from the formation of complex molecules in space to the growth of planets. Through vastly improved spectral characterization of Galactic polarization, the PICO data will discriminate among models of Galactic dust composition to elucidate the chemical evolution of the Galaxy (SO6, § 2.5.1). The data will also guide the construction of methods for separating diffuse dust emission from cosmological signals of interest, particularly the inflationary signal.

(2) *Determine how magnetic fields affect molecular cloud and star formation:* Stars are formed through interactions between gravitational and magnetic fields, turbulence, and gas over more than four orders of magnitude of spatial scales, which span the diffuse ISM (kpc scale), molecular clouds (10 pc), and molecular cloud cores (0.1 pc). However, the role magnetic fields play in the large-scale structure of the diffuse ISM and in the observed low star-formation efficiency has been elusive owing to the dearth of data. By virtue of the strong dynamical coupling of dust and gas and the systematic alignment of dust grains with magnetic fields, PICO's dust polarization measurements will for the first time probe the large-scale Galactic magnetic field with resolution to trace the role of magnetic fields through the entirety of the star formation process (SO7, § 2.5.2).

2.5.1 Test Models of the Composition of Interstellar Dust

Strong extinction features at 9.7 μm and 18 μm indicate that much of interstellar dust is in the form of amorphous silicates, while features at 217.5 nm, 3.3 μm, and 3.4 μm attest to abundant hydrocarbons. It is unknown, however, whether the silicate and carbonaceous materials coexist on the same grains or whether grains of each composition grow through distinct, parallel pathways dictated by their surface chemistry.

Some data suggest that the populations are distinct. Spectropolarimetry of dust extinction reveals robust polarization in the 9.7 μm silicate feature [e.g., *127*], indicating that the silicate grains are aligned with the interstellar magnetic field. In contrast, searches for polarization in the 3.4 μm carbonaceous feature have yielded only upper limits, even along sightlines where silicate polarization is observed [*128*, *129*]. These data are consistent with silicate and carbonaceous materials existing on separate grains that have different alignment properties.

At odds with the spectropolarimetric evidence from dust extinction are current measurements of the polarization fraction of the far-infrared dust emission with *Planck* [*130*] and BLASTPol [*131*]. They show little to no frequency dependence, whereas substantial frequency dependence would be expected if two components with distinct polarization properties were contributing to the total emission.

With excellent polarization sensitivity, even in diffuse regions, PICO will provide a definitive test of the two-component paradigm [*132*]. In this case, the PICO baseline mission will determine the intrinsic polarization fractions of each of the two components to a precision of 3%. With this level of precision the data will validate or reject state-of-the-art dust models [e.g. *133*, *134*], test for the presence of additional grain species with distinct polarization signatures, such as magnetic nanoparticles [*135*], and will be used as a crucial input for the foreground separation necessary to extract cosmological E and B-mode science.

Anomalous Microwave Emission (AME) is a component of Galactic emission peaking in the 20–30 GHz range that has been tentatively identified with small, rapidly-spinning dust grains [*136*]. As only upper limits have been placed on its polarization, its role as a foreground for cosmological B-mode science remains unclear; even small levels of polarization could prove challenging (§ 2.7). PICO will finely sample the AME SED with its bands at 21, 25, 30, 36, and 43 GHz. Combined with ground-based maps at lower frequencies, for example C-BASS at 5 GHz [137], PICO will be used to efficiently separate the AME from synchrotron and free-free emission and either detect or place stringent upper limits on its polarization. Further, the enhanced frequency coverage will allow changes in the AME SED with interstellar environment to be characterized and thus elucidate its underlying physics.

2.5.2 Determine How Magnetic Fields Affect Molecular Cloud and Star Formation

Stars form out of dense, gravitationally unstable regions within molecular gas clouds, which themselves form through the flow of diffuse, atomic-phase gas to denser regions. Magnetic fields play an important role throughout this process.

On the largest scales, magnetized turbulence mediates the flow of the gaseous ISM from the atomic to the denser, molecular phase. Recent observations suggest that the structure of the diffuse medium is highly anisotropic, and strongly coupled to the local magnetic field [138–141]. As molecular gas clouds collapse to form stars, magnetic fields can slow the process of star formation by inhibiting movement of gas in the direction perpendicular to the field lines. Observations to date suggest that the outer envelopes of clouds can be supported against gravity by magnetic fields and turbulence, but in dense cores gravity tends to dominate, and so these dense structures can collapse to form stars [142]. The degree to which magnetic fields affect the formation of molecular clouds, as well as stars within these clouds, is poorly constrained, in large part due to the difficulty of making detailed maps of magnetic fields in the ISM.

• **Formation of Magnetized Molecular Clouds from the Diffuse Interstellar Medium** A comprehensive understanding of the magnetized diffuse ISM is challenging because of its diverse composition, its sheer expanse, and the multi-scale nature of the physics that shapes it. To understand how matter and energy are exchanged between the diffuse and dense media, it is essential to measure the properties of the magnetic field over more than four orders of magnitude in column density. PICO is unique in its ability to provide the necessary data. *Planck* achieved measurements of the diffuse sky at $60'$ resolution, resulting in $\sim$30,000 independent measurements of the magnetic field direction. With $1.1'$ resolution PICO will expand the number of independent polarization measurements to 86,000,000 (Fig. 2.11). The data will thus robustly characterize turbulent properties like the Alfvén Mach number, $\mathscr{M}_A$, across a previously unexplored regime of parameter space.

PICO's observations will complement recently completed high-dynamic-range neutral hydrogen surveys, such as HI4PI [143] and GALFA-HI [144], as well as planned surveys of interstellar gas, most prominently with the SKA and its pathfinders. One of the open questions in diffuse structure formation is how gas flows within and between phases of the ISM. A planned all-sky absorption line survey with the forthcoming SKA-1 will increase the number of measurements of the ISM gas temperature by several orders of magnitude [145]. Quantitative comparisons of the ISM temperature distribution from SKA-1 and estimates of the magnetic field strength and coherence length scale from PICO will elucidate the role of magnetized turbulence in the flow of matter in the ISM from diffuse regions to regions of denser molecular gas.

• **Formation of Stars within Magnetized Molecular Clouds** The role of the magnetic field in star formation is quantified by the ratio of the energies stored in magnetic and gravitational fields, and the ratio of the energy stored in the magnetic field to that stored in turbulence. The first ratio is parameterized through a mass-to-flux ratio μ, and the second through $\mathscr{M}_A$.

With full-sky coverage and a resolution of $1.1'$, PICO will map all the molecular clouds out to a distance of 3.4 kpc with better than 1 pc resolution. Extrapolating from the Bolocam Galactic Plane Survey [BGPS, 146], PICO is expected to make highly detailed magnetic field maps of over 2,000 molecular clouds with 10^3–10^5 independent polarization measurements per cloud. These are the *only foreseeable* measurements that will give μ and $\mathscr{M}_A$ over a statistically significant sample of molecular clouds. *Planck*, for example, mapped only ten nearby clouds to a similar level of detail [147]. A large sample of clouds is crucial because (1) dust polarization observations are sensitive only to the magnetic field projected on the plane of the sky, and therefore polarization maps will look very different for molecular clouds observed at different viewing angles; and (2) the relative importance of the magnetic field will likely be a function of cloud age and mass. By observing thousands of molecular clouds PICO will determine μ and $\mathscr{M}_A$ for different sub-classes of cloud age and mass.

2.5.3 Galactic Legacy Science

PICO will also produce legacy datasets that will revolutionize our understanding of how magnetic fields influence physical processes ranging from planet formation to galaxy evolution. For ten clouds closer than 500 pc, PICO will resolve magnetic fields on scales of 0.1 pc. This is the scale of dense cores and filaments for these clouds, and thus the observations will constrain how magnetic fields on these scales influence the formation of cloud cores. Currently no experiment has the sensitivity and resolution to observe both the the large-scale (few parsec) and core-scale magnetic fields. By comparing the orientation of the core-scale magnetic fields with the orientation and sizes of proto-planetary disks, PICO will probe whether magnetic braking influences the growth of such disks [*148*, *149*] and provide complementarity to higher angular resolution instruments such as ALMA and SOFIA [*126*, *150*] (Fig. 2.11).

Key processes in the diffuse ISM, including heat transport, streaming of cosmic rays, and magnetic reconnection depend strongly on the level of the environment's magnetization [*151*–*153*]. PICO will give information about these processes with tens of millions of independent measurements of magnetic field orientation over the entire Galaxy. The measurements will also enable studies of the physical processes that generate magnetic fields through a combination of turbulence and large-scale gas motions [*154*].

Finally, PICO observations will create detailed magnetic field maps of about 70 nearby galaxies, with $\sim$100 or more measurements of magnetic field directions per galaxy. Currently, polarized dust emission has only been observed in M82 and NGC 253 using SOFIA [*155*]. The PICO observations will determine how interaction between large-scale magnetic fields, turbulence, and feedback from previous generations of star formation affect galaxy evolution and star-formation efficiency.

2.6 Legacy Surveys

PICO was designed to respond to requirements posed by the seven SOs listed in Table 1.3. It will also generate a rich catalog of hundreds of thousands of new sources consisting of proto-clusters, strongly lensed galaxies, and polarized radio and dusty galaxies. An abundance of information about galaxy and cluster evolution, dark matter, the physics of jets of active galactic nuclei, and magnetic fields of dusty galaxies will be stored in this catalog (Table 2.1). The catalog will be mined in future years through subsequent analysis and follow-up observations.

2.6.1 Early Phases of Galaxy Evolution

PICO's catalog of high-z strongly-lensed galaxies will provide answers to major open issues in galaxy formation and evolution. What are the main physical mechanisms shaping the properties of galaxies [*156*, *157*]: in situ processes, interactions, mergers, or cold flows from the intergalactic medium? And how do feedback processes work? To settle these issues we need direct information on the structure and dynamics of high-z galaxies. But these are compact, with typical sizes of 1–2 kpc [*158*]), corresponding to angular sizes of 0.1–0.2$''$ at $z \simeq 2$–3. Thus they are hardly resolved, even by ALMA or by HST. If they *are* resolved, high enough SNR per resolution element is only achieved for the brightest galaxies, which are probably not representative of the general population.

Strong gravitational lensing provides a solution to these problems. Since lensing conserves the surface brightness, the effective angular size is stretched on average by a factor of $\mu^{1/2}$, where μ is the gravitational magnification, thus substantially increasing the resolving power. A spectacular example is ALMA observations of the *Planck*-discovered, strongly lensed galaxy PLCK_G244.8+54.9 at $z \simeq 3.0$ with $\mu \simeq 30$ [*159*]. ALMA observations with a 0.1$''$ resolution reached an astounding spatial resolution of 60 pc, substantially smaller than the size of Milky Way giant molecular clouds. CO spectroscopy of this object, measuring the kinematics of the molecular gas, gave an uncertainty of 40–50 km s^{-1}. Such precision allows a high

Table 2.1: **Legacy Surveys**

Catalog	**Impact**	**Science**
Strongly lensed galaxies	Discover 4500[a] strongly lensed and highly magnified dusty galaxies across redshift. Current knowledge: 13 sources confirmed in *Planck* data; few hundred candidates in *Herschel*, SPT and ACT data.	Gain information about the physics governing early, $z \simeq 5$, galaxy evolution, taking advantage of magnification and extra resolution enabled by gravitational lensing; learn about dark matter sub-structure in the lensing galaxies.
Proto-clusters	Discover 50,000[a] mm/sub-mm proto-clusters distributed over the sky out to $z \sim 4.5$. Current knowledge: *Planck* + ACT/SPT data expected to yield a few tens.	Probe the earliest phases of cluster evolution, well beyond the reach of other instruments; test the formation history of the most massive virialized halos; investigate galaxy evolution in dense environments.
Nearby galaxies	Detect 30,000 galaxies at $z \lesssim 0.1$ at frequencies above 300 GHz. Current knowledge: 3400 (280) source candidates with *Planck* 857 (353) GHz band.	Using frequencies that match cold (15 − 25 K) dust emission, give its spectral energy distribution as a function of galaxy properties to enable correlations with star formation activity.
Polarized point sources	Detect 2000[b] radio and several thousand dusty galaxies in polarization. Current knowledge: about 200 radio sources up to 100 GHz; one polarization measurement of a dusty galaxy.	Study the physics of jets of extragalactic sources, close to their active nuclei; determine the large-scale structure of magnetic fields in dusty galaxies; determine the importance of polarized sources as a foreground for CMB polarization science.
Cosmic infrared background	Provide eight maps of the anisotropy from dusty star-forming galaxies for frequencies $\nu > 200$ GHz, and with $1'$ resolution at 800 GHz. Current knowledge: Three *Planck* (higher noise) maps between 300 and 900 GHz with $5'$ resolution.	Improve constraints on the parameters describing universal star-formation history. Construct a tracer of large-scale structure for CMB de-lensing. Cross-correlate with galaxy surveys and CMB lensing map.

[a] Confusion (not noise) limited [b] Noise and confusion limited

SNR detection of the predicted $\sim$1000 km s^{-1} outflows capable of sweeping the galaxy clear of gas that would otherwise be available for star formation [160]. In this specific case, there were no clear indications that mergers or cold flows shaped the galaxy, but similar spectroscopy of another strongly lensed galaxy at $z = 5.3$ detected a fast (800 km s^{-1}) molecular outflow due to feedback [161].

PICO will detect thousands of early forming galaxies whose flux densities are boosted by large factors due to strong lensing (Fig. 2.12, right). Currently there are reports of just a few other high-z galaxies that are spatially resolved thanks to gravitational lensing, albeit with less extreme magnifications [162–164]. PICO's catalog will be transformative as it will probe the spectral energy distribution (SED) of the lensed galaxies at their peaks. Two examples of known sources are shown in the left panel of Figure 2.12. While ground-based instruments observe at frequencies up to $\nu = 10^{11.45}$ Hz, PICO's data will extend to the peak of the SED, up to $\nu = 10^{11.9}$ Hz.

A straightforward extrapolation of the *Herschel* counts to the 70% non-Galactic sky gives a detection of 4,500 strongly-lensed galaxies with a redshift distribution peaking at $2 \lesssim z \lesssim 3$ [165], but extending up to $z > 5$ (Fig. 2.12, left panel). If objects like the $z = 5.2$ strongly lensed galaxy HLS J091828.6+514223 exist at higher redshifts, they will be detectable by PICO out to $z > 10$. At the 600 GHz detection limit, about 25% of all detected extragalactic sources will be strongly lensed; for comparison, at optical/near-IR and radio wavelengths, where intensive searches have been carried out for many years, the yield is only about 0.1%, more than two orders of magnitude lower [166]. To add to the extraordinary sub-mm lensing bonanza, the selection of PICO-detected strongly lensed galaxies will be extremely easy because of their peculiar sub-mm colors (Fig. 2.12, left panel), resulting in a selection efficiency close to 100% [167]. The

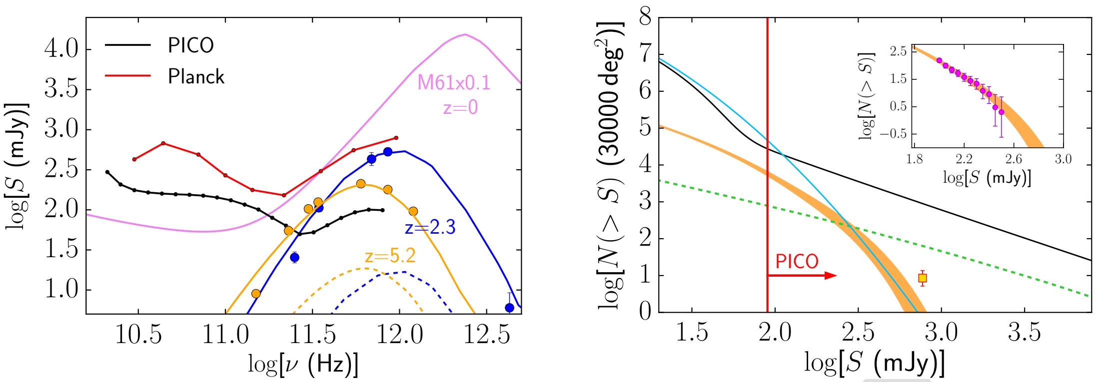

Figure 2.12: **Left:** PICO will detect thousands of new strongly lensed galaxies near the peak of their spectral energy distributions (SEDs), such as SMM J2133−0102 (blue) at $z = 2.3$ [168] and HLS J091828.6+514223 (orange) at $z = 5.2$ [169]. The dashed lines are the SEDs before magnification by lensing. PICO's higher resolution gives point-source detection limits (black line) that are up to 10 times fainter than *Planck*'s 90% completeness limits (red line [170]). High-frequency measurements ($\nu > 300$ GHz) of 30,000 low-z galaxies, like M61 (magenta, SED was scaled down by a factor of ten), will give a census of their cold dust. **Right:** Integral counts of unlensed (black) and strongly lensed, high-z (orange) star-forming galaxies for 70% of the sky away from the Galactic plane at 600 GHz based on fits of *Herschel* counts over 1000 deg^2 (inset [165]). The PICO detection region (right of vertical red line) will yield a factor of 1000 increase in strongly lensed galaxies relative to *Planck* (yellow square), as well as about 50,000 proto-clusters (blue) and 2,000 radio sources (green) [171].

survey will find the brightest objects over the entire sky, maximizing the efficiency of selecting sources for follow-up observations.

The intensive high spectral and spatial resolution follow-up campaign of this large sample will enable a leap forward in our understanding of the processes driving early galaxy evolution and open up other exciting prospects, both on the astrophysical and on the cosmological side [e.g., 166].

2.6.2 Early Phases of Cluster Evolution

PICO will open a new window for the investigation of early phases of cluster evolution, when their member galaxies were actively star forming (and dusty), but the hot IGM was not necessarily in place. In this phase, traditional approaches to cluster detection (X-ray and SZ surveys, and searches for galaxy red sequences) work only for the more evolved clusters, which do include hot IGM; indeed these methods have yielded only a handful of confirmed proto-clusters at $z \gtrsim 1.5$ [172].[10] *Planck* has demonstrated the power of low-resolution surveys for the study of large-scale structure [173], but its resolution was too poor to detect individual proto-clusters [171]. Studies of the high-z two-point correlation function [171, 174] and *Herschel* images of the few sub-mm bright protoclusters detected so far, at $z \leq 4$ [175–177], all of which will be detected by PICO, indicate sizes of $\simeq 1'$ for the proto-cluster cores, nicely matching the PICO FWHM at the highest frequencies.

PICO will detect 50,000 proto-clusters as peaks in the high-frequency maps, which are not available for ground-based instruments (Table 2.1; blue line in the right-hand panel of Fig. 2.12). The redshift distribution will extend out to $z \sim 4.5$. This catalog will be augmented by 150,000 evolved clusters, detected by the SZ effect. This will constitute a breakthrough in the observational validation of the formation history of the most massive dark-matter halos, traced by clusters, representing a crucial test of models for structure formation. Follow-up observations will characterize the properties of member galaxies, probing galaxy evolution in dense environments and shedding light on the complex physical processes driving it.

2.6.3 Additional Products of PICO Surveys

PICO will yield a complete census of cold (15–25 K) dust, available to sustain star formation in the nearby universe, by detecting tens of thousands of galaxies mostly at $z \lesssim 0.1$; the SED of M61 is a typical example

[10] More high-z proto-clusters have been found by targeting the environment of tracers of very massive halos, such as radio-galaxies, QSOs, and sub-mm galaxies. These searches are, however, obviously biased.

(Fig. 2.12, left). With a statistical population, and information only available using data at frequencies above 300 GHz, we will investigate the spectral energy distribution of the dust as a function of galaxy properties, such as morphology and stellar mass.

PICO will increase by an order of magnitude the number of blazars selected at sub-mm wavelengths and will determine the SEDs of many hundreds of them up to 800 GHz and up to $z > 5$. Blazar searches are the most effective way to sample the most massive black holes at high z because of the Doppler boosting of their flux densities. PICO's surveys of the largely unexplored mm/sub-mm spectral region will also offer the possibility to discover new transient sources or events, such as blazar outbursts [178].

PICO will make a leap forward in the determination of the polarization properties of both radio sources and dusty galaxies over a frequency range where ground-based surveys are impractical or impossible. It will find 1,200 radio sources and 350 dusty galaxies above a flux density limit of 4 mJy at 320 GHz, and 500 radio sources and 15,000 dusty galaxies above 6 mJy at 800 GHz. These data will give information on the structure and ordering of large-scale magnetic fields in dusty galaxies. In the case of radio sources, emission at higher frequencies comes from regions closer to the central engine, providing information on the innermost regions of the jets close to the active nucleus.

The anisotropy of the cosmic infrared background (CIB), produced by dusty star-forming galaxies over a wide redshift range $0 < z \lesssim 5$, is an excellent probe of the history of star-formation across time. The *Planck* collaboration derived values for parameters describing the rate of star-formation out to $z \sim 4$ [179–181]). PICO's lower noise and twice the number of frequency bands will give an order of magnitude improvement on the statistical errors for these parameters [182]. Similar improvement will be achieved in constraining $M_{\rm eff}$, the galaxy halo mass that is most efficient in producing star-formation activity. PICO's increased sensitivity to Galactic dust polarization will enhance the separation of signals coming from the largely unpolarized CIB and polarized Galactic dust; an effective separation of signals currently limits making reliable, legacy-quality CIB maps. By providing a nearly full-sky map of matter fluctuations traced by dusty star-forming galaxies, such a set of maps could be used for delensing the CMB [183], for measuring local primordial non-Gaussianity from CIB auto-correlations [184], or for cross-correlations with CMB lensing and with galaxy surveys [110].

2.7 Signal Separation

2.7.1 The Signal Separation Challenge

In the PICO frequency range there are Galactic and Extra-Galactic sources of emission. Galactic emissions are due to free-free, synchrotron, and dust, which arise respectively from photon-mediated free electron-proton scattering, free electrons spiraling around Galactic magnetic field lines, and from $\sim$20 K elongated interstellar dust grains partially aligned with the local magnetic field. Free-free emission is expected to have negligible polarization. The emission from synchrotron and dust are linearly polarized, and has both E and B components (Fig. 2.13). Extra-Galactic sources of emission include the CMB, which has both E and B-modes, and point sources of various types whose polarization level and type are not well constrained. The task of 'separating the signal to its components' (sometimes shortened to 'component separation') is to decompose the detected signal to its constituent sources. The precision of signal separation is determined by the requirement to detect or set an upper limit on the inflationary B-mode, which is the faintest among PICO's targeted signals. In that context, the terms 'foreground separation' and 'foreground cleaning' are used as equivalents to 'signal separation'.

Galactic emission dominates the sky's polarized intensity on large angular scales ($\ell \lesssim 10$), it dominates the cosmological B-modes signals for $\ell \lesssim 150$ for all allowed levels of r, and it is expected to be significant even at $\ell \simeq 1000$, posing challenge for reconstructing the B-mode signal from lensing. This is illustrated in Figs. 2.1 and 2.13, which show Galactic emission power spectra calculated for the cleanest – that is, the least Galactic-emission-contaminated – 60% of the sky. But even in small patches of the sky, far from the Galactic plane and with the least foreground contamination, Galactic emission levels are substantial relative to an inflationary signal of $r \sim 0.01$ and overwhelm it for $r \lesssim 0.001$ [185]. Separating the cosmological and Galactic emission signals is *the* primary challenge facing any next-decade experiment attempting to reach these levels of constraints on r, along with control of systematic uncertainties.

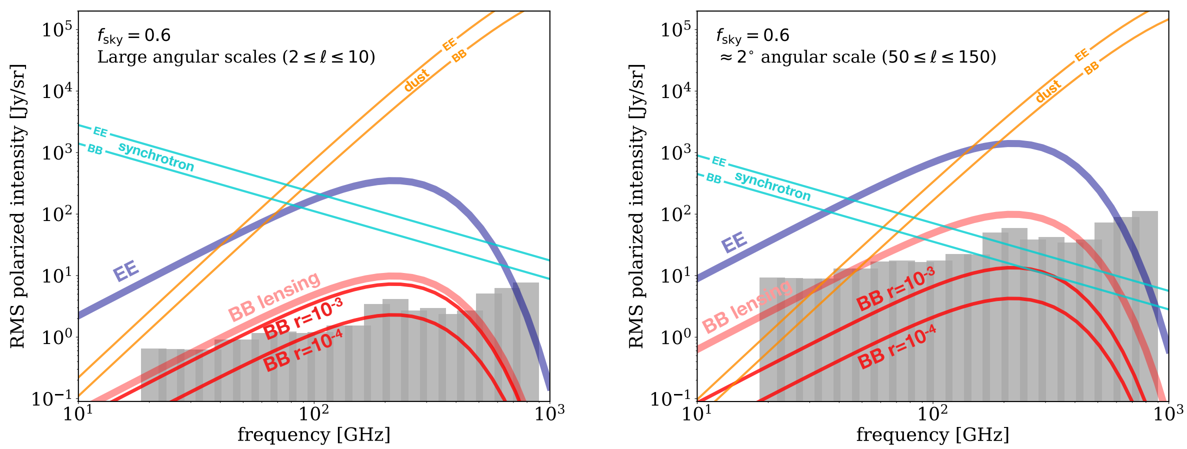

Figure 2.13: Polarization *BB* spectra of Galactic synchrotron and dust, compared to CMB polarization *EE* and *BB* spectra of different origins for two values of r and for two ranges of angular scales: large-scale, $\ell \lesssim 10$, corresponding to the reionization peak (left panel); and intermediate $50 \lesssim \ell \lesssim 150$, corresponding to the recombination peak (right panel). Data from *Planck* indicate that for Galactic emission the level of E-mode is approximately twice that of B [185]. The PICO baseline noise (grey bands) is low compared to the Galactic emission components, and thus they will be measured with high SNR in many frequency bands.

Foreground separation is challenging because the spatial power spectra and frequency spectra of the foregrounds are not known to sufficient accuracy anywhere across the sky. To a first approximation, the spectrum of synchrotron emission is a power law $I_{\rm sync} \propto \nu^{\alpha}$, with $\alpha \simeq -1$. The spectrum of dust emission is $I_{\rm dust} \propto \nu^{\beta} B_{\nu}(T_{\rm dust})$, where $\beta \simeq 1.6$, $T_{\rm dust} \simeq 20\,{\rm K}$, and $B_{\nu}(T)$ is the Planck function; this is referred to as 'modified blackbody emission'. If those models exactly reflected the properties of emitting sources, then in principle an experiment that had six frequency bands could determine the three emission parameters, as well as the three amplitudes corresponding to that of dust, synchrotron, and the CMB. However, recent observations have shown that neither emission law is universal, that spectral parameters are not necessarily the same for intensity and polarization and that they vary across the sky [186–188], and thus that the analytic forms and parameter values given above are only approximately valid for averages across the sky [189]. Also, while both emission laws are well-motivated phenomenological descriptions, the fundamental physics of emissions from grains of different materials, sizes, and temperatures, and of electrons spiraling around magnetic fields implies that these laws are expected to be neither exact, nor universal.

At the low levels of r targeted by PICO and by other next-decade experiments, even small inaccuracies in foreground modeling and characterization lead to biases and false detections. For example, several publications have demonstrated that fitting complicated dust temperature profiles using a simple one- or two-temperature model will bias the fitted CMB signal at levels $\delta r \lesssim 10^{-3}$, which is significant compared to PICO's goal [190–194].

Further complicating the foreground-separation challenge is the fact that additional polarized foregrounds may exist. Anomalous microwave emission (AME), dust-correlated emission peaking in intensity near 30 GHz, is an important low-frequency foreground in total intensity. It has been tentatively attributed to small, rapidly-spinning dust grains [136]. Very few measurements of AME polarization exist, and there are only loose constraints on its fractional polarization; it is less than 3% (2σ) at 18 GHz in one 0.5% region of the sky [195]. If AME is 1% polarized, left uncorrected it would give rise to a bias of $\delta r \simeq 5 \times 10^{-4}$ [196]. Astrophysical emission from CO lines at mm wavelengths is expected to be 0.1–1 % polarized [197, 198]. Extragalactic radio sources show a median polarization of 2% [199–201], and

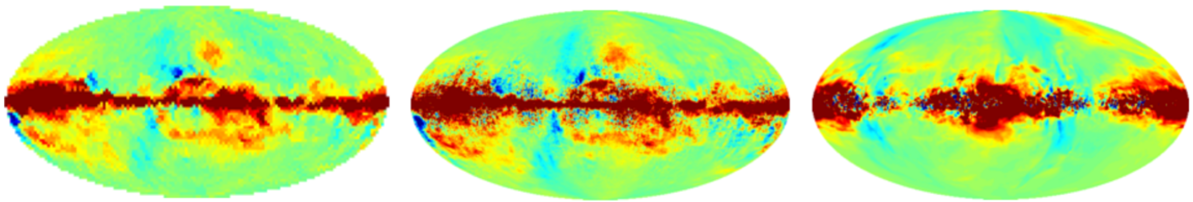

Figure 2.14: Foreground maps: *Planck* measured sky (left) at 143 GHz, models at 155 GHz from PySM (middle) [210] and Galactic MHD simulations (right). The model generated by MHD simulations is only constrained to match *Planck* Galactic foregrounds spatial power spectra, not the actual spatial realization.

there is significant uncertainty about the polarization of dusty galaxies emitting in the PICO wavebands. Initial quantitative estimates show that ignoring radio sources and dusty galaxies may each lead to a bias $\delta r > 3\times10^{-3}$ [199, 202, 203] at low and high frequencies, respectively, and ignoring the CO $J = 1 \rightarrow 0$ line could lead to a bias $\delta r > 2\times10^{-3}$ [198] at 115 GHz. These levels are appreciable compared to the goals of PICO and other next-decade experiments.

2.7.2 Foreground Separation Assessment and Methodology

Two broad approaches are used for foreground separation and for assessment of its precision. In the parametric approach the foregrounds are assumed to follow emission laws described by a number of free parameters. Parametric models use the frequency dependence of the data in each line of sight to determine the values of the parameters [204]. Since the CMB spectrum is well determined, measurements with a sufficient number of frequency bands and appropriately broad frequency coverage can distinguish foreground emission from the CMB using their different spectral dependences. Non-parametric techniques, in contrast, rely on the fact that CMB emission is uncorrelated with the foregrounds and thus correlations within a given spatial/frequency data-cube can be used to separate the two distinct sources of emission [121, 205–208]. Simulated data are used to assess the efficacy of both techniques as the complexity of the assumed foreground emission is increased. For the parametric models, we can also employ analytic methods to estimate the uncertainty on emission parameters as a function of instrument noise, but specific assumptions must be made about the underlying nature of the emission laws [209].

To investigate the efficacy of PICO to address the foreground-separation challenge, we used both an analytic forecast and map-domain simulations.

• **Analytic Forecast** The analytic forecast relies on an established, documented, publicly available, cosmological parameters forecasting code [209]. The code uses *Planck*-reported Galactic emissions; it assumes that the foreground spectral indices are constant across patch sizes of $\sim 15^\circ$ on a side; it employs a parametric maximum-likelihood approach to remove the foregrounds and to forecast $\sigma(r)$; and it uses the cleanest 60% of the sky. Lensing B-modes are included in the input spectra (and are partially removed via delensing, taking into account noise and residual foregrounds), but the input for the inflationary signal is $r = 0$. Results from the publicly available code have been verified using an independent code that uses similar analytic calculations.

• **Map-Domain Simulations** Map-domain simulations have become the 'gold standard' in the community. In this approach, we simulate sky maps that are constrained by available data, but otherwise have a mixture of foreground properties. We 'observe' these maps just like a realistic experiment would do, and then apply foreground separation techniques – both parametric and non-parametric – to separate the Galactic and CMB emissions.

To test the results we constructed a variety of full-sky models. All the models were broadly consistent with available data and with uncertainties from WMAP and *Planck*, but they differed in their degrees of Galactic emission complexity. Models included spectral parameters varying spatially and along the line of sight, anomalous microwave emission up to 2% polarized, dust polarization that rotates slightly as a function of frequency because of projection effects, or dust SEDs that depart from a simple modified blackbody. All the foreground maps were generated at native resolution of 7′ pixels [*211*] with widely-used and thoroughly-tested map-generation codes [*122*, *210*]. Fig. 2.14 shows two of the eight models and data from *Planck*. The right panel is constructed to mimic the *Planck* Galactic emissions statistically. The middle panel is constructed to mimic the observed spatial distribution of Galactic emission. The differences between these and the *Planck* map illustrate that different realizations of the sky are allowed by current data, and highlight the level of current Galactic emission uncertainties.

For each of the eight models, we added CMB signals in both intensity and polarization, matching a ΛCDM universe. The input inflationary signal was $r = 0$, i.e., no signal, and the *BB*-lensing matched the level after 85% delensing as forecasted for PICO. Each of these sky models had 50 realizations of the PICO noise level. The sky models were analyzed with a variety of techniques, which were based on the two broad categories described above. Because of limited resources for this study not all models were analyzed with all techniques, and not all realizations were used.

2.7.3 Results and Discussion

When using the PICO baseline noise levels with the analytic forecasts we find that $\sigma(r) = 2\times10^{-5}$, a level that is five times lower than required ($\sigma(r) = 1\times10^{-4}$, see SO1). We consider this forecast optimistic because it assumes strictly white noise, a specific model for the underlying foregrounds that has only eight parameters[11] per 15×15 deg^2 pixel, and Gaussian parameter likelihood functions. The foregrounds may be more complex, requiring more parameters (for example, spatially varying temperature for the dust, or more than a single spectral index per source of emission), and may have stronger spatial variations. The parameter likelihoods may not be Gaussian.

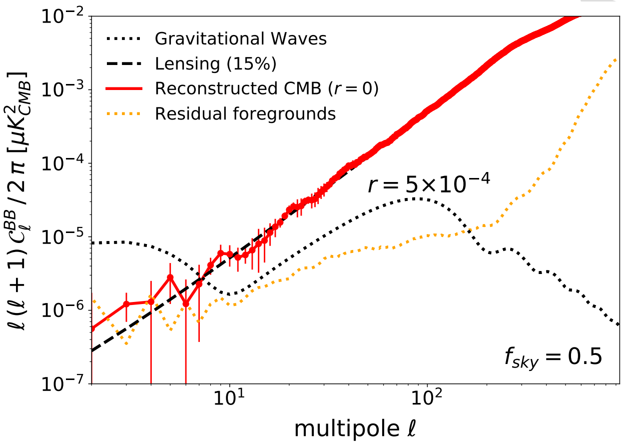

Figure 2.15: Angular power spectra of *BB* due to the CMB and of residual foregrounds after an end-to-end map-based foreground-separation exercise. The PICO low noise levels and breadth in frequency coverage enable suppression of foregrounds such that the residual foreground spectrum (yellow dotted) is a factor of ten (four) [which?] below a *BB* inflationary signal with $r = 5\times10^{-4}$ (black dotted). Within errors, the recovered CMB (red) matches the input CMB, which consists of only lensing *BB* (dashed black), over all angular scales $\ell \gtrsim 6$. In this exercise we used 50% of the sky. Lower foreground residual levels are obtainable with smaller, cleaner patches of ∼10% of sky, which would reduce the residual foregrounds at $\ell \simeq 80$.

The 'gold-standard' map-based simulations give initial evidence that the combination of PICO's sensitivity and broad frequency coverage are effective in foreground removal and that PICO will reach the requirement of $r = 5\times10^{-4}(5\sigma)$. Fig. 2.15 shows the result of a foreground-separation exercise over 50% of the sky, with one representative model of Galactic emissions. This exercise used GNILC, one of the non-parametric techniques [*208*], tuned to give low foregrounds on the largest angular scales, that is, the lowest ℓ modes. The input CMB *BB* signal, consisting of only lensing *B*-modes, is reconstructed within errors for all $\ell \gtrsim 6$. The residual foreground *BB* power spectrum, encoding the levels of remaining foreground emission after foreground separation, is a factor of 50 below the CMB at $\ell = 100$ and a factor of five at $\ell = 10$. Most importantly, the residual foreground is a factor of ten below an inflationary *BB* signal for $r = 5\times10^{-4}$ at $\ell \simeq 4$. These are the angular scales at which the inflationary signal is stronger than the signal from lensing. Comparing the residual foreground at this ℓ to the input *BB* foregrounds at, for example, 155 GHz (Fig. 2.1) we find a suppression of $\sim10^6$ in μK^2 (a factor of 1000 in temperature), which is a consequence of using

[11] Six amplitudes for the Q and U Stokes parameters of the CMB, dust, and synchrotron emission, and two spectral indices, for dust and synchrotron.

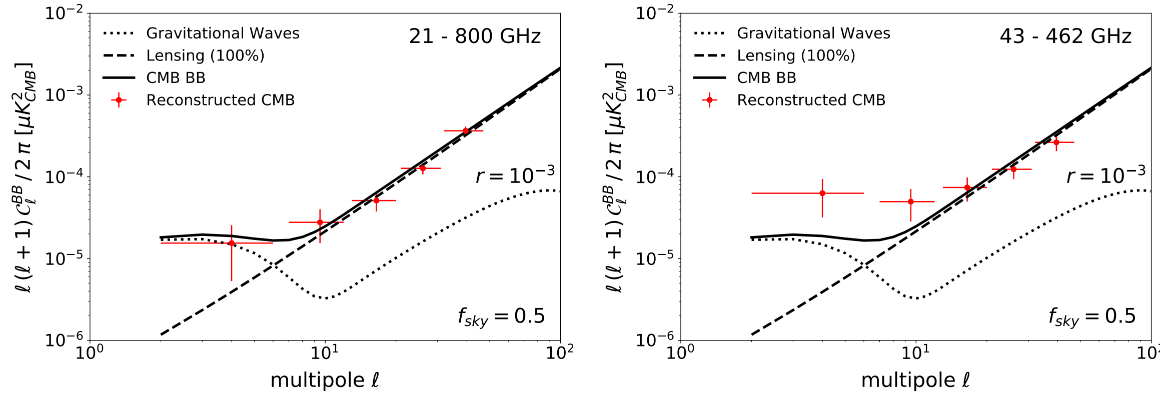

Figure 2.16: **Left:** Foreground separation with all of PICO's 21 frequency bands recovers the input CMB *BB* power spectrum (solid black) without bias (red). The input CMB spectrum has a contribution from lensing (dashed) and an inflationary signal with $r = 0.001$ (dotted). This exercise uses a parametric approach [204] with foregrounds varying on 4° pixels, and using 50% sky fraction. **Right:** Running the same foreground separation algorithm on the same sky but using only PICO's bands between 43 and 462 GHz produces an output spectrum (red) that is biased at low multipoles relative to the input. With real data, such a bias would be erroneously interpreted as a higher value of r.

all of PICO bands.

At intermediate angular scales, $\ell \simeq 80$, the residual foreground is a factor of four lower than the inflationary signal. We expect lower residuals when GNILC is optimized for this ℓ range. And for reconstructing signals at this ℓ range, it is sufficient to analyze data from smaller ~3% regions of the sky. These will have lower mean foreground levels, making the foreground-separation exercise easier, and pushing residuals to levels lower than already demonstrated here for 50% of the sky. With its full-sky coverage, PICO will have access to several independent 3% sky patches, and will thus make several independent detections of its r target.

Some of our results validate the need for a broad frequency coverage with a strong lever arm on Galactic emissions outside the primary CMB bands. Fig. 2.16 shows that removing several of PICO's frequency bands, particularly those that monitor dust at high frequencies and synchrotron at low frequencies, can significantly bias the extracted *BB* power spectrum, especially at the lowest multipoles. In this exercise the input CMB contained the lensing signal *and* an inflationary signal with $r = 0.001$, and a specific parametric technique was used for foreground separation [204].

While these results suggest that PICO's frequency coverage and sensitivity will be adequate for this level of r, more work should be invested to gain complete confidence. For example, some of the other sky models give a level of residual foregrounds that would give biased measurements reflecting much larger values of r, even with PICO's low noise and broad frequency coverage; and some of the foreground-separation techniques appear to give consistently higher foreground residuals than others. To make progress, it is important to continue the simulations and algorithm development program, by running numerous realizations of different sky models and analyzing them with various approaches; optimizing sky masks; and potentially using a combination of techniques to handle large, intermediate, and small angular scale foregrounds differently. It would also be valuable to continue measurements of Galactic emissions with ground- and balloon-based experiments to further reduce the current level of Galactic emission uncertainties.

2.8 Systematic Uncertainties

Having flown two space missions (WMAP and *Planck*) and fielded numerous sub-orbital experiments to measure polarization, the mm/sub-mm wavelength community has gained extensive experience with systematic uncertainties that occur in various experimental configurations. A rich literature investigates the types of systematic errors due to the environment, the instrumentation, observation strategies, and data analysis that could confound polarization measurements by creating a bias or an increased variance [212–219]. Teams have used the accumulated experience to incorporate technological solutions during the design phase, and to optimize data analysis techniques to identify and compensate for systematic errors.

Just as requirements on signal separation (§ 2.7) are determined by the need to reach the faintest inflationary signal, so are the requirements on control of systematic uncertainties. Since an inflationary *BB* power spectrum with $r = 5 \times 10^{-4}$ has a peak signal level of 7 nK, systematic effects need to be controlled to a level of $\sim$1 nK. It has long been recognized that exquisite control of systematic uncertainties will be required from any experiment attempting to reach levels of $r \lesssim 1 \times 10^{-3}$, and it is widely accepted that the stability provided aboard a space platform makes it best suited to control systematic uncertainties compared to other platforms. This is one of the most compelling reasons to observe from space. As WMAP and *Planck* demonstrated, an L2 orbit offers excellent thermal stability, as well as flexibility in the choice of scan strategy.

Sources of systematic effects and their ultimate degree of severity are a function of the instrument implementation, the spacecraft scan strategy, and mitigations methods developed during the data analysis pipeline. Thus, a proper assessment requires end-to-end simulation of the mission. Such a simulation should include realistic instabilities and non-idealities of the spacecraft, telescope, and instrument, as well as folding in data post-processing techniques. Developing such a simulation is a significant undertaking, which took years for the *Planck* mission, and was beyond the scope of this study. We have instead opted to (1) implement design features within PICO that would provide strong data redundancy and enable cross-checks during the data analysis (§ 2.8.5), and (2) enumerate the sources of possible systematic errors, assess their effects, and investigate three that were deemed the highest risk (§ 2.8.1–§ 2.8.4).

2.8.1 Potential Systematics Effects

The systematic effects faced by PICO can be grouped into three broad categories: (1) Coupling between signals; (2) stability; and (3) stray light. For the first category, the most important are the intensity coupling into polarization (both E and B) and E coupling into B. This is because T (denoting intensity) is approximately ten times stronger than E, which is approximately ten times stronger than B. The systematic effects are listed in Table 2.2 and were prioritized for further study using a risk factor incorporating a PICO Systematics Working Group's assessment of how mission-limiting the effect is, how well these effects are understood by the community and whether mitigation techniques exist.

We used simulations to investigate the following three effects that had risk level 5: error in the absolute calibration of polarization angle; error in the relative calibration between orthogonally oriented detectors, and the effect of the telescope sidelobes. We adapted tools developed for *Planck* [220] and in the context of a European-led mission concept [221]. To understand the severity of the effects, we analyzed each in isolation, and in most cases without complicating effects such as inclusion of foreground-separation steps. More detailed studies of the combination of effects and the inclusion of a foreground-separation step are important but are left to the future.

2.8.2 Absolute Polarization Angle Calibration

In PICO, each of the Stokes Q and U parameters along any line of sight is evaluated through having sensitivity to two orthogonal polarization states. The relative designation of Q and U is derived from having sensitivity to pairs of polarization orientations that are 45° apart. A systematic error in the implementation (or estimation) of these angles by an amount α causes signals in Q and U, and thus in E and B to mix. Because the CMB E is much larger than B, mixing between E and B leads to the generation of a spurious BB angular power spectrum that mirrors the shape of the EE spectrum (Fig. 2.17). The level of spurious BB is proportional to $\alpha^2 \times EE$. At angular multipoles $\ell \lesssim 100$ a systematic error $\alpha \approx 10'$ will result in a spurious BB level that is approximately equivalent to $r \sim 1 \times 10^{-4}$ [213, 222]. The mixing of E and B also leads to spurious cross-spectra EB and TB, that respectively mimic the EE and TE spectra.

The systematic error is most usefully split to two contributions: an overall 'absolute' error in the assumed instrument's sensitivity to polarization orientations relative to fixed sky coordinates, and a 'relative' rotation error between various pairs of detectors. For PICO, the relative rotation of the detectors will be measured

Table 2.2: Enumeration of potential systematic errors anticipated in PICO's measurements together with their assessed risk level, their effects on the measurements, and subsections with further discussion for effects with risk level 5.

Name	Risk[a]	Effect[b]	
Coupling of Signals			
Polarization angle calibration	5	$E \to B$	§ 2.8.2
Bandpass mismatch	4	$T \to P$, $E \to B$	
Beam mismatch	4	$T \to P$, $E \to B$	
Time response accuracy and stability	4	$T \to P$, $E \to B$	
Readout cross-talk	4	spurious P	
Chromatic beam shape	4	spurious P	
Gain mismatch	3	$T \to P$	
Cross-polarization	3	$E \to B$	

Name	Risk[a]	Effect[b]	
Stability			
Gain stability	5	$T \to P$, $E \to B$	§ 2.8.3
Pointing jitter	3	$T \to P$, $E \to B$	
Straylight			
Far sidelobes	5	spurious P	§ 2.8.4
Other			
Residual correlated noise (1/f, cosmic ray hits)	3	increased variance	

[a] Level 5 indicates a highly significant, design-driving effect; it may have limited past measurements, or is not well understood. Level 4 is an effect that is either known to be large but is understood reasonably well, or is a smaller effect that requires precise modeling. In Level 3 we expect the effect to be small, but it is not sufficiently well understood and detailed modeling will be done during Phase A study. Level 2 indicates a well-understood or minimal effect that may not need modeling, and Level 1 is for an effect that is not significant and does not need modeling. [b] $T \to P$ denotes coupling of the intensity signal (labeled as T to denote temperature) into polarization, which would generally be both E and B. Similar meaning holds for $E \to B$.

to $\sim 0.1'$ by comparing the measured polarization signals between many independent detectors and pairs. However, directly measuring the overall rotation in flight – which is the process of calibrating the polarization angles – is challenging as there are no sufficiently well calibrated polarized astronomical sources. For example, Aumont et al. [222] showed that the current uncertainty of $0.33°$ on the Crab polarization orientation limits measurements to $r \sim 0.01$, which is much larger than PICO's target.

PICO will overcome this potential source of error through using its high SNR measurement of the polarization to identify and reduce it below relevant levels in data analysis. Yadav et al. [214] showed that because the T and E signals are much stronger than B, an experiment that searches for a specific level of cosmological BB will have high SNR for detecting the spurious EB and TB cross-spectra. Applying their method to the PICO baseline specifications we find that with PICO we will constrain overall rotation to a level of $\alpha = 0.2'$ and $0.6'$ (3σ) using the EB and TB spectra, respectively, suppressing this systematic effect to negligible levels (Fig. 2.17). The constraints quoted include delensing level of 73%, which is the PICO forecast including foreground separation.

2.8.3 Differential Gain

Photometric calibration is the process of converting the raw output of each detector – typically given in digital detector readout units – to physical units via a calibration factor $C(t)$, which is a function of time. One straightforward way for PICO to derive Q and U is through differencing detectors that are sensitive to two orthogonal polarization states A and B. A systematic error in the determination of either of the A or B calibration factors will translate to a biased Q or U. We investigated whether the anticipated error on $C_{A,B}(t)$ is adequate for PICO's requirements on measuring the faint inflationary signal.

The inflationary signal will be extracted from data in the primary CMB bands between 60 and 300 GHz. Detectors in these bands will be calibrated using measurements of the CMB dipole, a signal that will be measured once per minute as the telescope scans the sky (§ 4.1.2). We evaluated the combined impact of the scan strategy and white- and 1/f-noise in the estimation of $C(t)$. The simulation included signals from the anisotropy of the CMB, including the dipole and BB lensing. Full details of the simulation pipeline are available in the PICO website [223]. Fig. 2.17 demonstrates that the power spectrum due to error in $C_{A,B}(T)$ is much lower than the PICO requirement of $\sigma(r) = 1 \times 10^{-4}$.

2.8.4 Far Sidelobes

Differences between the assumed and actual antenna pattern of the detectors will give rise to systematic errors. *Planck*'s ground-based measurements mapped the antenna response to levels down to -90 dB from the main lobe give range from Karl. The best in-flight measurements, made through repeated passes of solar system planets reached levels of -60 dB karl check [**?**]. Thus in-flight measurements were only useful to

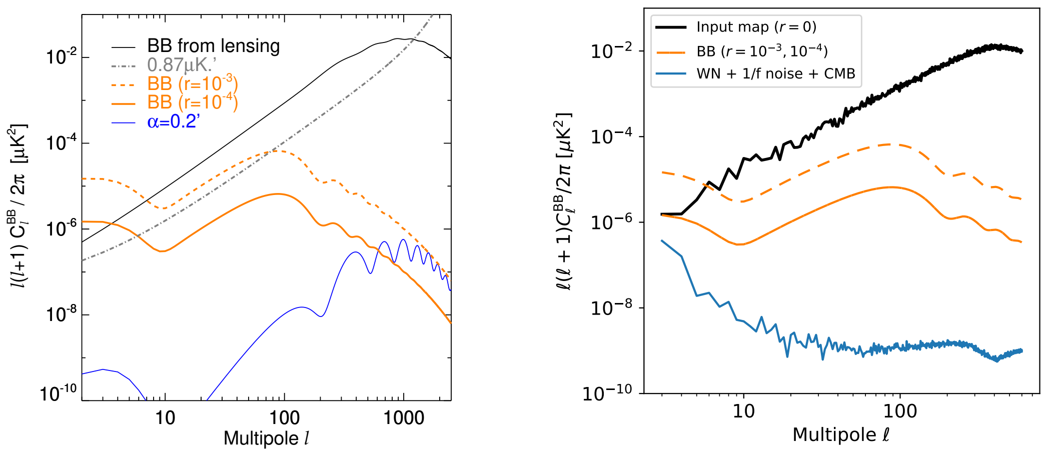

Figure 2.17: Two of the initially-estimated highest risk systematic effects for PICO can be suppressed to low levels relative to requirements; we show inflationary signals with $r = 1 \times 10^{-4}$ and 1×10^{-3} (solid and dash orange, respectively), and *BB* lensing (black, theory on the left; realization on right). Left: The residual spurious *BB* spectrum due to $0.2'$ mis-calibration of PICO's angles of polarization sensitivity (solid blue) has the shape of the *EE* spectrum, and is small compared to the requirement for $\ell < 200$ and compared to the baseline statistical noise level (grey dash). Right: simulated residual *BB* power after accounting for calibration drifts (solid blue).

reconstruct in-flight antenna pattern within a region of few degrees of the main lobe, not in the 'far sidelobes' of the antenna response.

Far-sidelobe response can couple to bright Galactic signals when the telescope points tens of degrees away from the Galactic plane. If such far-sidelobe response is not known, the signals could be interpreted as faint cosmological signals and bias estimates of their magnitude. To evaluate PICO's susceptibility to this systematic effect we used the same physical optics software as used by *Planck* to compute PICO's 4π sr antenna response for four 155 GHz detectors located at the center of the focal plane. We simulated the time domain response of the detectors as they scanned the sky over a year of PICO observations. We convolved their antenna response with a full-sky Galactic emission model [*210*], reconstructed maps of I, Q, and U, and calculated the resulting *BB* angular power spectrum when using a *Planck* Galactic mask excluding 60% of sky [**?**].

The largest sidelobe in the antenna response is at a level of -80 dB from the main lobe. We find that if that sidelobe is known with SNR of 20, or further suppressed by that factor, the contamination from the sidelobe is suppressed to more than a factor of ten below the requirement of $\sigma(r) = 5 \times 10^{-4}$. This suppression can be achieved by adjusting the instrument design, e.g. adding baffles, or by modeling, measuring, and removing the sidelobe pickup during data analysis.

2.8.5 Key Findings

Properly modeling, engineering for, and controlling systematic effects are key for the success for any experimental endeavor striving to achieve $\sigma(r) \lesssim 1 \times 10^{-4}$. Based on extensive community experience with both hardware and analysis of data collected in space and in sub-orbital experiments we note the following points:

- Relative to other platforms, a space-based mission provides the most thermally stable platform, and thus the pre-requisite for improved control of systematic effects. PICO's orbit at $L2$ is among the most thermally stable of possible orbits.
- PICO's sky scan pattern will give strong data redundancy, which will enable numerous cross-checks. Each of the 12,996 detectors will make independent maps of the I, Q, and U Stokes parameters enabling many comparisons within and across frequency bands, within and across sections of the focal plane, and within and across bolometers that have the same (or different) polarization sensitivities. Half the sky is scanned every two weeks, and the entire sky is scanned in 6 months. Thus combinations of maps con-

Table 2.3: Relative characteristics of ground, balloon, and space platforms for experiments in the CMB bands.

Characteristic	Ground	Balloon	Space
Sky coverage	Partial from single site	Partial from single flight	Full
Frequency coverage	70 GHz inaccessible,[a] $\nu \geq 300$ GHz unusable, limited atmospheric windows	70 GHz inaccessible,[a] otherwise, almost unlimited	Unrestricted
Angular resolution at 150 GHz [b]	$1\overset{\prime}{.}5$ with 6 m telescope	$6'$ with 1.5 m telescope	$6'$ with 1.5 m telescope
Detector noise [c]	$265\,\mu K_{CMB}\sqrt{s}$	$162\,\mu K_{CMB}\sqrt{s}$	$38\,\mu K_{CMB}\sqrt{s}$
Integration time	Unlimited, with interruptions	Weeks, continuous	Several years, continuous
Repairability, Upgradeability	Good	None; multiple flights possible	None

[a] 70 GHz is the frequency at which large angular scale *B*-mode Galactic emissions have a minimum (Fig. 2.13). [b] We give representative telescope apertures. Significantly larger apertures for balloons and in space result in higher mass, volume, and cost. [c] The noise-equivalent temperatures given are illustrative of general capabilities. Detailed comparisons depend on detector heat sink temperatures, bandwidths, and other factors that differ among specific implementations. Ground – median detector noise at 95 GHz from BICEP3 [224]; balloon – median detector noise at 94 GHz from SPIDER [225]; space – 90 GHz from PICO CBE.

structed at different times during of the mission will be differenced to search for residual time-dependent systematic effects.

- The PICO scan pattern gives almost continuous scans of planets; *Planck* observed each of the planets with a 6 month cadence. This will significantly improve antenna pattern characterization. The scan pattern also has the benefit of nearly continuous large-amplitude CMB dipole signals, which will give high SNR calibration.
- We showed that two of the highest risk factor systematic effects can be controlled to levels that are small compared to requirements. More analysis and planning is required to address systematic uncertainties arising from the far sidelobe response of the telescope.

Undoubtedly, more work is required to analyze other systematic effects, their combination, and their coupling with foreground separation. We strongly recommend that support be provided for such activities. Specifically, support for suborbital efforts is essential to continue the development of means to identify systematic effects, and to develop new techniques to mitigate them. In addition, we endorse support for the development of a complete end-to-end software simulation facility, which is the only to quantify mission trade-offs under the influence of a combination of systematic effects that are coupled to the task of signal separation.

2.9 Complementarity with Sub-Orbital Measurements

Since the first CMB measurements, more than 50 years ago, important observations have been made from the ground, from balloons, and from space. Each of the CMB satellites flown to date – COBE, WMAP, and *Planck* – has relied crucially on technologies and techniques that were first proved on ground and balloon flights, making these also crucial to the success of PICO. The phenomenal success and the immense science outcomes of past space missions is a direct consequence of their relative advantages (Table 2.3). In every respect, with the exception of repairability and upgradeability, space has the advantage.

When the entire sky is needed, as for fluctuations on the largest angular scales, space is by far the most suitable platform. When broad frequency coverage is needed, space will be required to reach the ultimate limits set by astronomical foregrounds. As Figs. 2.1 and 2.13 demonstrate, Galactic emissions overwhelm the inflationary signal on large and intermediate angular scales ($\ell \leq 150$), and they are significant even at high ℓ, potentially limiting the process of delensing that is necessary for reaching $r \lesssim 0.001$. The stability offered in space can not be matched on any other platform, and it translates to superb control of systematic uncertainties. There is a consensus within the CMB community that for levels of $r \lesssim 0.001$ the challenges in the measurement are the ability to control systematic uncertainties and to remove Galactic emissions;

modern focal plane arrays like the one employed by PICO have ample raw sensitivity. The PICO goal of reaching $\sigma(r) = 5 \times 10^{-4}\,(5\sigma)$ is beyond the reach of sub-orbital observations in the foreseeable future.

For science requiring higher angular resolution, such as observations of galaxy clusters with ~ 1 arcmin resolution at 150 GHz, the ground has an advantage. An appropriately large aperture on the ground will also provide high resolution information at lower frequencies, which may be important for separating Galactic emissions at high ℓ.

The relative advantages of a space mission used to come with higher costs relative to sub-orbital experiments. However, with the advent of massive ground-based efforts this balance shifts; the costs for a next generation ground-based CMB experiment planned for the next decade are squarely within the cost window of this Probe. A recommended plan for the next decade is therefore to pursue a space mission, and complement it with an aggressive ground program that will overlap in ℓ space, and will add science at the highest angular resolution, beyond the reach of a space mission.

Balloon observations have been exceedingly valuable in the past. They co-led discoveries of the temperature anisotropy and polarization, provided proving grounds for the technologies enabling the success of COBE, WMAP and *Planck*, and trained the scientists that then led NASA's space missions. There are specific areas for which balloon missions can continue to play an important role, despite their inherently limited observing time. Balloon payload can access frequency bands above 280 GHz; currently there are no plans for any ground program to conduct observations at higher frequencies. These frequency bands will provide important, and perhaps critical information about polarized emission by Galactic dust, a foreground that is currently known to limit knowledge of the CMB signals. With flights above 99% of the atmosphere, balloon-borne observations are free from the noise induced by atmospheric turbulence, making them good platforms for observations of the low ℓ multipoles, and for characterizing foregrounds on these very large angular scales. From a technology point of view, the near-space environment is the best available for elevating detector technologies to TRL6; and balloon-platforms continue to be an excellent arena for training the scientists of tomorrow.

2.10 Measurement Requirements

The set of physical parameters and observables that derive from the PICO SOs place requirements on the depth of the mission, the fraction of sky the instrument scans, the frequency range the instrument probes and the number of frequency bands, the angular resolution provided by the reflectors, and the specific pattern with which PICO will observe the sky.

• **Depth** We quantify survey depth in terms of the RMS fluctuations that would give a signal-to-noise ratio of 1 in a sky pixel that is $1'$ on a side. The science objective driving the depth requirement is SO1, the search for the inflationary signal, which requires a combined depth of 0.87 μK$\cdot$arcmin. This requirement is a combination of the low-level of the signal, the need to separate the various signals detected in each band, and the need to detect and subtract systematic effects to anticipated levels. The map depth requirement flows to instrument sensitivity requirements (Table 1.3 and to the mission duration requirement (5 years, assuming >= 95% survey efficiency).

• **Sky Coverage** There are several SOs driving a full-sky survey for PICO. The term 'full-sky' here refers to the entire area of sky available after separating other astrophysical sources of confusion. In practice this implies an area of 50-70% of the full sky for probing non-Galactic signals, and the rest of the sky for achieving the Galactic science goals.

(1) Probing the optical depth to the epoch of reionization (SO5) requires full sky coverage as the signal peaks in the *EE* power spectrum on angular scales of 20° to 90° $(2 \leq \ell \leq 10)$. Measuring this optical depth to limits imposed by the statistics of the small number of available ℓ modes is key for minimizing the error on the neutrino-mass measurement.

(2) If $r \neq 0$, the inflationary *BB* power spectrum (SO1) has local maxima on large angular scales 20° to 90°, $(2 \leq \ell \leq 10$, the reionization peak), and around 1° ($\ell \simeq 80$, the recombination peak) (Figure 2.1). A de-

tection would strongly benefit from confirmation at *both* angular scales. Measurements of the reionization peak are currently beyond the capabilities of ground-based instruments. A detection would also strongly benefit from confirmation *in several independent patches of the sky*. This is achievable with PICO through observing the recombination peak in several small (3-5% sky fraction) patches of the sky. No similar capability is currently planned for any next-decade instrument.

(3) The PICO constraint on N_{eff} (SO4) requires a determination of the EE power spectrum to limits imposed by the statistics of available ℓ modes. Full sky coverage is required to achieve this limit.

(4) Achieving the targeted neutrino mass limits (SO3), giving two independent 4σ constraints on the minimal sum of 58 meV, requires a lensing map, and cluster counts from as large a sky fraction as possible.

(5) PICO's survey of the Galactic plane and regions outside of it is essential to achieving its Galactic structure and star-formation science goals (SO6, 7).

• **Frequency Bands** The multitude of astrophysical signals that PICO will characterize determine the frequency range and number of bands that the mission requires. The Galactic and cosmological signal are separable using their spectral signatures. The cosmological signals peak in the frequency range between 60 and 300 GHz. Galactic signals, specifically the make-up of Galactic dust (SO6), require spectral characterization in frequencies between 100 and 800 GHz. Simulations indicate that 21 bands, each with 25% bandwidth, that are spread across the range of 20 - 800 GHz can achieve the separation between Galactic and cosmological signals at the level of fidelity required by PICO (§ 2.7).

• **Resolution** Several SOs require an aperture of 1.4 m, and, as a consequence, the resolution per frequency listed in Table 1.1. To reach $\sigma(r) = 1 \times 10^{-4}$ we will need to 'delens' the E- and B-mode maps, as described in Sections 2.2 and 2.3.2. Delensing efficacy is a function of noise and resolution. For PICO, the combination of the two gives $\sim$80% delensing, which is adequate for achieving our SOs. The process of delensing may be affected by contamination from Galactic dust. It is thus required to map Galactic dust to at least the same resolution as in the main CMB bands GHz. Higher resolution is mandated by SO6 and 7, which require resolution of $1'$ at 800 GHz.

The constraints on the number of light relics (SO4) will be extracted from the EE power spectrum at multipoles $2 \lesssim \ell \lesssim 4000$. Resolution enabled by a 1.4 m telescope is required to achieve the high end of this ℓ range.

• **Sky Scan Pattern** Control of polarization systematics uncertainties at anticipated levels is enabled by: (1) making I, Q, and U Stokes-parameter maps of the entire sky from each independent detector; (2) by enabling sub-percent absolute gain calibration of the detectors through observations of the CMB dipole; and (3) by enabling cross-checks on the results through comparing multiple cuts of the data, a process known as 'jack-knife test'. With these requirements we chose a sky scan pattern (§ 4.1.2) that enables each detector to scan a given pixel of the sky in a multitude of directions, satisfying requirement (1). The scan gives large amplitude CMB dipole signals in spacecraft rotations throughout the lifetime of the mission, satisfying requirement (2). With PICO's sky scan pattern, more than 50% of the sky is scanned within two weeks of the start of the survey. The entire sky is surveyed within 6 months, and then this pattern repeats. Thus the PICO scan pattern gives multiple ways to perform data jack-knives, satisfying requirement (3).

3 Instrument

PICO meets all of its science-derived instrument requirements (Table 1.3) with a single instrument: an imaging polarimeter with 21 logarithmically spaced frequency bands centered between 21 and 799 GHz. The instrument is built around a two-reflector Dragone-style telescope (§ 3.1 and Fig. 3.1) with an internal aperture stop between the primary and secondary. The focal plane is populated by 12,996 TES bolometers (§ 3.2) read out using a time-domain multiplexing scheme (§ 3.3). The instrument employs a single science observing mode: fixed rate imaging while scanning the sky (§ 4.1.2).

The instrument is configured inside the shadow of a V-grooves assembly that thermally and optically shields it from the Sun (Fig. 3.1). The V-groove assembly consists of 4 nested radiation shields that provide

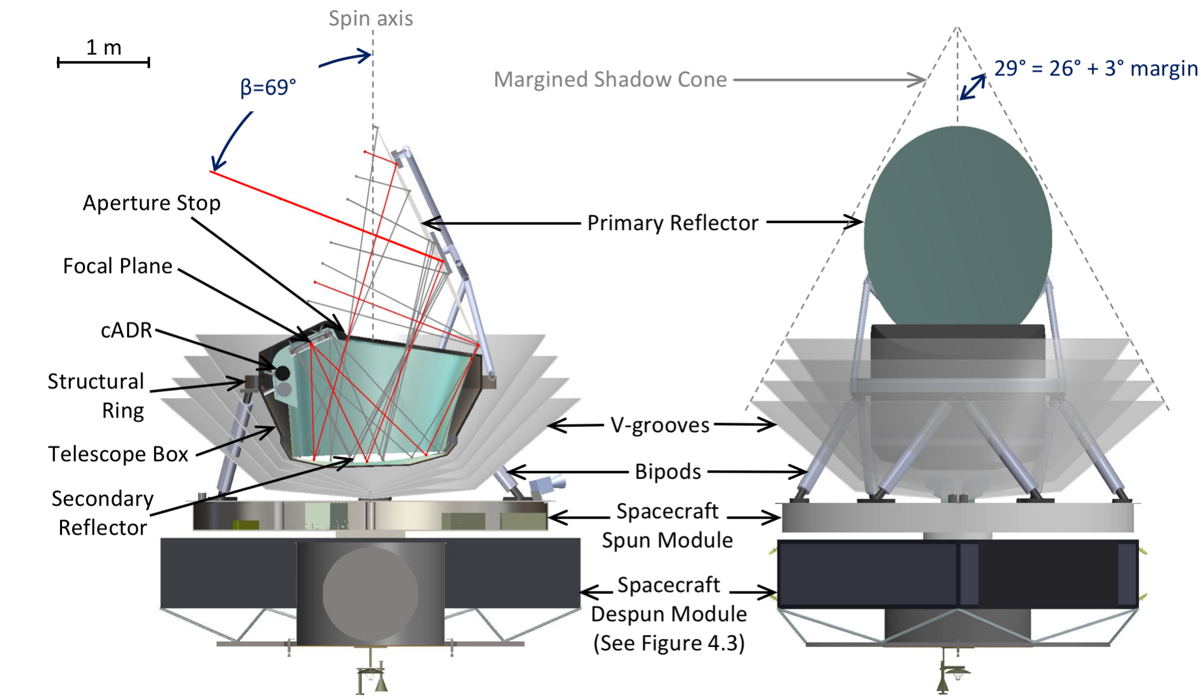

Figure 3.1: Detailed PICO instrument configuration. *Left*: Side view in cross section. *Right*: Front view with V-Groove assembly shown semi-transparent. The spacecraft spun module accommodates warm instrument components: the 4 K cooler compressor and drive electronics, the sub-K cooler drive electronics, and the detector warm readout electronics.

passive cooling (§ 3.4.3). The sun shadow cone depicted in Fig. 3.1 is 29°. The angle to the Sun during the survey, $\alpha = 26^\circ$ (§ 4.1.2 and Fig. 4.2), is supplemented with a margin of 3° to account for the radius of the sun ($0\overset{\circ}{.}25$), pointing control error, design margin, and alignment tolerances.

The V-groove assembly is attached to the bipod struts that support the instrument structural ring. The ring supports the primary reflector and telescope box. The telescope box contains the actively cooled components (§ 3.4.1, § 3.4.2), including the secondary reflector, the focal plane and sub-kelvin adiabatic refrigerator structures. Just inside the box, a thermal liner serves as a cold optical baffle and aperture stop. Instrument integration and test (I&T) are described in § 3.5.

During the survey, the instrument is spun at 1 rpm (§ 4.1.2). Spacecraft control is simplified by mounting the instrument on a spinning spacecraft module, while a larger non-spinning module houses most spacecraft subsystems (§ 4.3). Instrument elements that act as heat sources are accommodated on the spinning module of the spacecraft.

3.1 Telescope

The PICO telescope design is driven by a combination of science requirements and physical volume limits. The science requirements are: a large diffraction-limited field of view (DLFOV) sufficient to support $\sim 10^4$ detectors, arcminute resolution at 800 GHz, low spurious polarization, and low sidelobe response. All requirements are met with PICO's 1.4 m aperture modified open-Dragone design. There are no moving parts in the PICO optical system.

The PICO optical design was selected following a trade study examining cross-Dragone, Gregorian Dragone, and open-Dragone designs [*226*]. The open-Dragone and crossed-Dragone offer more diffraction-limited focal plane area than the Gregorian Dragone [*227*], and are able to support enough detectors to provide the required sensitivity. The open-Dragone does not require the massive and voluminous baffles that the cross-Dragone does, and hence can satisfy the aperture size requirement within the shadow cone.

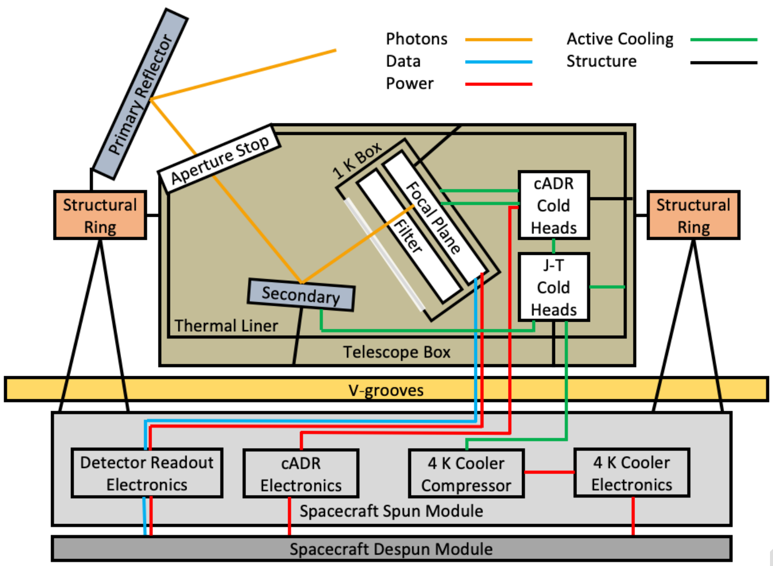

Figure 3.2: PICO instrument block diagram. Active coolers provide cooling to the 100 mK focal plane, the surrounding 1 K box, the 4.5 K secondary reflector, and the 4.5 K thermal liner that acts as a cold aperture stop. Data from the focal plane flows to (redundant, cross-strapped) warm readout electronics on the spun module of the spacecraft bus.

PICO's initial open-Dragone design has been modified by adding an aperture stop and adding corrections to the primary and secondary reflectors to enlarge the DLFOV. The detailed geometric parameterization of the PICO optical design is described in [*226*]. The primary reflector (270 cm $\times$ 205 cm) is passively cooled and the secondary reflector (160 cm $\times$ 158 cm) is actively cooled. The highest frequency (900 GHz) sets the surface accuracy requirement of the reflectors at $\sim \lambda/14 = 24\,\mu$m. The focal ratio is 1.42. The slightly concave focal surface, which has a radius of curvature of 4.55 m, is telecentric to within $0.^\circ12$ across the entire FOV.

An actively cooled circular aperture stop between the primary and secondary reflectors reduces detector noise and shields the focal plane from stray radiation. Stray-light analysis of the PICO open-Dragone design using GRASP confirms that the focal plane is protected from direct view of the sky, and that spillover past the primary is suppressed by 80 dB relative to the main lobe for both co-pol and cross-pol beams. Detailed baffle design will be performed during mission formulation.

3.2 Focal plane

PICO's focal plane is populated by an array of TES bolometers operating in 21 frequency bands, each with 25% fractional bandwidth, and band centers ranging from 21 to 799 GHz. Polarimetry is achieved by differencing the signals from pairs of two co-pointed bolometers that are sensitive to two orthogonal polarization states. A conceptual layout of the PICO focal plane is shown in Fig. 3.3 and detailed in Table 3.1.

Bolometers operating in the mm/sub-mm wave band are photon-noise limited. Therefore, increase in sensitivity is achieved through an increase in detector count. The PICO focal plane has 12,996 detectors, 175 times the number flown aboard *Planck* thereby providing a breakthrough increase in sensitivity with a comparably sized telescope. This breakthrough is enabled by development and demonstration in suborbital projects, which now commonly operate arrays of 10^3–10^4 detectors (§ 5).

3.2.1 21–462 GHz Bands

Several optical coupling technologies have matured over the past ten years to efficiently use focal plane area: horns with ortho-mode transducers (OMTs) [*228*], lithographed antenna arrays [*229*], and sinuous antennas under lenslets [*230*]. Horn-coupling and sinuous antenna/lenslet-coupling deliver quantum efficiency $> 70\,\%$ over more than an octave of bandwidth, which can be partitioned into two or three colors per pixel. Alternatively, antenna-array coupling has only demonstrated single-color pixels to date, but uniformly illuminated feeds enable much smaller pixels and therefore more densely packed focal planes.

The PICO baseline focal-plane design employs three-color sinuous antenna/lenslet-coupling [*231*] for

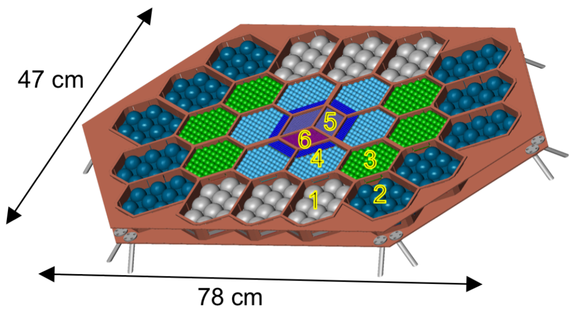

Figure 3.3: PICO focal plane. Detectors are fabricated on six types of tiles (shown numbered and colored as in Table 3.1). The wafers are located on the focal plane such that higher frequency bands, which require better optical performance, are placed nearer to the center.

Table 3.1: PICO makes efficient use of the focal area with multichroic pixels (three bands per pixel, § 3.2.1). The sampling rate is based on the smallest beam (Table 3.2), with 3 samples per FWHM at a scan speed $(360^\circ/\mathrm{min})\sin(\beta = 69^\circ) = 336^\circ/\mathrm{min}$. Scaling from sub-orbital experience, we anticipate that TES bolometers can support these sampling rates with a factor of $\sim 4\times$ margin.

Tile type	N_{tile}	Pixels/ tile	Pixel type	Bandcenters [GHz]	Sampling rate [Hz]
1	6	10	A	21, 30, 43	45
2	10	10	B	25, 36, 52	55
3	6	61	C	62, 90, 129	136
4	6	85	D	75, 108, 155	163
		80	E	186, 268, 385	403
5	2	450	F	223, 321, 462	480
6	1	220	G	555	917
		200	H	666	
		180	I	799	

the 21–462 GHz bands. Niobium microstrips mediate the signals between the antenna and detectors, and partition the feed's wide continuous bandwidth into three narrow channels using integrated micro-machined filter circuits [232]. The technology maturation required for PICO is described in $ 5.1.

3.2.2 555–799 GHz Bands

PICO's highest three frequency channels are beyond the niobium superconducting band-gap, rendering microstrip filters a poor solution for defining the optical passband. In this regime, PICO instead measures a single band with each pixel using feedhorn-coupled polarization-sensitive bolometers. Radiation is coupled through horns directly to absorber in the throat of a waveguide. TES bolometers detect the incident power. The waveguide cut-off defines the lower edge of the band, and quasi-optical metal-mesh filters define the upper edge. Numerous experiments have successfully used similar approaches [233–235]. The technology maturation required for PICO is described in § 5.2.

3.2.3 Sensitivity

PICO's Current Best Estimate (CBE) sensitivity meets the requirements of the baseline mission with $> 40\,\%$ margin (Table 3.2).

We developed an end-to-end noise model of the PICO instrument to predict mission sensitivity and provide a metric by which to evaluate mission design trades. The model includes four noise sources per bolometer: photon, phonon, Johnson, and readout (from both cold and warm readout electronics). To validate our calculations, we compared two independent software packages that have been validated with several operating CMB instruments. The calculations agreed within 1% both for individual noise terms and for overall mission noise. A detailed description of the PICO noise model and its inputs is available in Young et al. [226]; small differences between that publication and Table 3.2 are due to refinements of the primary mirror and stope temperatures.

Laboratory experiments have demonstrated that TES bolometers can be made background-limited in the low loading environment they would experience at L2 [236]. For PICO, the primary contributor to noise is the optical load. The sources of optical load are the CMB, reflectors, aperture stop, and low-pass filters. The

Table 3.2: PICO has 21 partially overlapping frequency bands with band centers (ν_c) from 21 GHz to 799 GHz and each with bandwidth $\Delta\nu/\nu_c = 25\,\%$. The beams are single mode, with FWHM sizes of $6\overset{\prime}{.}2 \times (155\,\mathrm{GHz}/\nu_c)$. The CBE per-bolometer sensitivity is photon-noise limited (§ 3.2.3). The total number of bolometers for each band is equal to (number of tiles) × (pixels per tile) × (2 polarizations per pixel), from Table 3.1. Array sensitivity assumes 90 % detector operability. The map depth assumes 5 yr of full sky survey at 95 % survey efficiency, except the 25 and 30 GHz frequency bands, which are conservatively excluded during 4 hr/day Ka-band (26 GHz) telecom periods (§ 4.2).

Band Center [GHz]	Beam FWHM [arcmin]	CBE Bolo NET [$\mu\mathrm{K_{CMB}\,s^{1/2}}$]	N_{bolo}	CBE Array NET [$\mu\mathrm{K_{CMB}\,s^{1/2}}$]	Baseline Array NET [$\mu\mathrm{K_{CMB}\,s^{1/2}}$]	Baseline polarization map depth [$\mu\mathrm{K_{CMB}}$ arcmin]	[$\mathrm{Jy\,sr^{-1}}$]
21	38.4	112	120	12.0	17.0	23.9	8.3
25	32.0	103	200	8.4	11.9	18.4	10.9
30	28.3	59.4	120	5.7	8.0	12.4	11.8
36	23.6	54.4	200	4.0	5.7	7.9	12.9
43	22.2	41.7	120	4.0	5.6	7.9	19.5
52	18.4	38.4	200	2.8	4.0	5.7	23.8
62	12.8	69.2	732	2.7	3.8	5.4	45.4
75	10.7	65.4	1020	2.1	3.0	4.2	58.3
90	9.5	37.7	732	1.4	2.0	2.8	59.3
108	7.9	36.2	1020	1.1	1.6	2.3	77.3
129	7.4	27.8	732	1.1	1.5	2.1	96.0
155	6.2	27.5	1020	0.9	1.3	1.8	119
186	4.3	70.8	960	2.0	2.8	4.0	433
223	3.6	84.2	900	2.3	3.3	4.5	604
268	3.2	54.8	960	1.5	2.2	3.1	433
321	2.6	77.6	900	2.1	3.0	4.2	578
385	2.5	69.1	960	2.3	3.2	4.5	429
462	2.1	133	900	4.5	6.4	9.1	551
555	1.5	658	440	23.0	32.5	45.8	1580
666	1.3	2210	400	89.0	126	177	2080
799	1.1	10400	360	526	744	1050	2880
Total			12 996	0.43	0.61	0.87	

CMB and stop account for at least 50% of the optical load at all frequencies up to and including 555 GHz. At higher bands emission from the primary mirror dominates.

The sensitivity model assumes white noise at all frequencies. Sub-orbital submillimeter experiments have demonstrated TES detectors that are stable to at least as low as 20 mHz [237], meeting the requirements for PICO's scan strategy (§ 4.1.2).

3.3 Detector Readout

Suborbital experiment teams over the past ten years have chosen to use voltage-biased TESs because their current readout scheme lends itself to Superconducting Quantum Interface Device (SQUID) based multiplexing. Multiplexing reduces the number of wires to the cryogenic stages and thus the total thermal load that the cryocoolers must dissipate. This approach also simplifies the instrument design.

In the multiplexing circuitry, SQUIDs function as low-noise amplifiers and cryogenic switches. The current baseline for PICO is to use a time-domain multiplexer (TDM), which assigns each detector's address in a square matrix of simultaneously read columns, and sequentially cycles through each row of the array [238]. The PICO baseline architecture uses a matrix of 128 rows and 102 columns. The thermal loading on the cold stages from the wire harnesses is subdominant to conductive loading through the mechanical support structures.

Because SQUIDs are sensitive magnetometers, suborbital experiments have developed techniques to shield them from Earth's magnetic field using highly permeable materials and superconducting materials [239]. Total suppression factors better than 10^7 have been demonstrated for dynamic magnetic fields [240].

Table 3.3: Projected cooler heat lift capabilities offer more than 100 % heat lift margin, complying with cooler technology best practices [247].

Component	Temperature [K]		Active Heat Lift [mW]		
	Required	CBE	Required per model[a]	Capability today	Projected capability
Primary reflector	< 40	17	N/A (radiatively cooled)		
Secondary reflector	< 8	4.5	42 at 4.5 K	> 55 at 6.2 K[b]	> 100 at 4.5 K[c]
Aperture stop	4.5	4.5			
cADR heat rejection[d]	4.5	4.5			
Focal plane enclosure and filter	1.0	1.0	0.36	1.0	N/A[e]
Focal plane	0.1	0.1	5.7×10^{-3}	32×10^{-3}	N/A[e]

[a] The required loads were calculated using Thermal Desktop. Reference [248] was used to estimate the thermal conductive loads through mechanical supports. In addition to the listed components, the total 4.5 K heat load includes the intercept on the focal plane mechanical supports. [b] Reference [249]. [c] Both NGAS and Ball project > 100 mW lift capability at 4.5 K using higher compression-ratio compressors currently in development (§ 3.4.2 and Fig. 3.4). [d] The cADR lift capability at 1 K and 0.1 K is from a Goddard quote. [e] Capability today already exceeds requirement.

PICO will use these demonstrated techniques to shield SQUID readout chips from the ambient magnetic environment, which is 20,000 times smaller than near Earth, as well as from fields generated by on-board components including the cADR (§ 3.4.1). The cADR is delivered with its own magnetic shielding which reduces the field to less than 0.1 G (less than that experienced by suborbital experiments).

SQUIDS are also sensitive to radio-frequency interference (RFI). Several suborbital experiments have demonstrated RFI shielding using aluminized mylar wrapped at cryogenic stages to form a Faraday cage around the SQUIDs [241–243]. Cable shielding extends the Faraday cage to the detector warm readout electronics.

Redundant warm electronics boxes perform detector readout and instrument housekeeping using commercially available radiation hardened analog-to-digital converters (ADCs), requiring 75 W total. The readout electronics compress the data before delivering them to the spacecraft, requiring an additional 15 W. PICO detectors produce a total of 6.1 Tbits/day assuming 16 bits/sample, sampling rates from Table 3.1, and bolometer counts from Table 3.2. *Planck* HFI typically achieved 4.7× compression in flight with information loss increasing noise by $\sim 10\,\%$ [244, 245]. Suborbital work has demonstrated 6.2× lossless compression [246]. PICO assumes 4× lossless compression.

3.4 Thermal

Like the *Planck*-HFI instrument, PICO's focal plane is maintained at 0.1 K to ensure low detector noise with straightforward cooling technology (§ 3.4.1). To minimize detector noise due to instrument thermal radiation, the aperture stop and reflectors are cooled using both active and radiative cooling (§ 3.4.2, § 3.4.3, Fig. 3.2). All thermal requirements are met with robust margins (Table 3.3).

3.4.1 cADR Sub-Kelvin Cooling

A multi-stage continuous adiabatic demagnetization refrigerator (cADR) maintains the PICO focal plane at 0.1 K and the surrounding enclosure, filter, and readout components at 1 K. The cADR employs three refrigerant assemblies operating sequentially to absorb heat from the focal plane at 0.1 K and reject it to 1 K. Two additional assemblies, also operating sequentially, absorb this rejected heat at 1 K, cool other components to 1 K, and reject heat at 4.5 K. This configuration provides continuous cooling with small temperature variations at both the 0.1 K and 1 K. Heat straps connect the two cADR cold sinks to multiple points on the focal plane assembly, which has high thermal conductance paths built in, to provide spatial temperature uniformity and stability during operation. The detector arrays are thermally sunk to the mounting frame. Heat loads in the range of 30 μW at 0.1 K and 1 mW at 1 K (time-average) are within the capabilities of

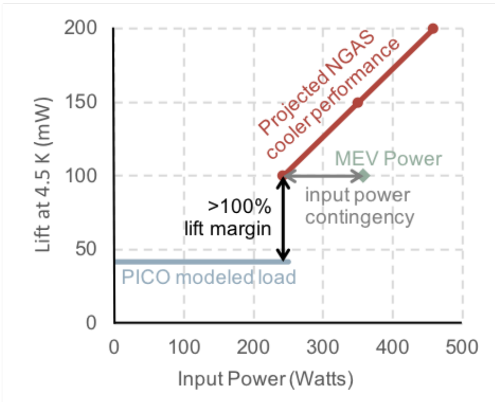

Figure 3.4: Projected performance of the NGAS cooler using a multi-stage compressor and ^{4}He circulating gas [253] meets PICO's requirements with $> 100\,\%$ margin. PICO requires heat lift of 42 mW at 4.5 K (Table 3.3). With 250 W of input power the NGAS cooler is projected to provide 100 mW of heat lift. We conservatively specify a maximum expected value (MEV) of 350 W as the compressor's input power, giving 100 W of additional input power contingency.

current cADRs developed by GSFC (§ 6.3) [250, 251]. The PICO sub-kelvin heat loads are estimated at less than half of this capability (Table 3.3).

3.4.2 4.5 K Cooler

A cryocooler system similar to that used on JWST to cool the MIRI detectors [252, 253] removes the heat rejected from the cADR and cools the aperture stop and secondary reflector to 4.5 K. Both NGAS (which provided the MIRI coolers) and Ball Aerospace have developed such coolers under the NASA-sponsored Advanced Cryocooler Technology Development Program [254]. NGAS and Ball use slightly different but functionally-equivalent hardware approaches. A 3-stage precooler provides ~ 16 K precooling to a separate circulated-gas loop. The circulated-gas loop utilizes Joule–Thomson (J-T) expansion, further cooling the gas to 4.5 K. The J-T expansion point is located close to the cADR heat rejection point and provides it the lowest temperature. Subsequently, the gas flow intercepts heat conducted to the focal plane enclosure, then cools the aperture stop and the secondary reflector before returning to the circulation compressor.

NGAS and Ball are actively working on increasing the flow rate and compression ratio of the J-T compressor, which should result in higher system efficiency and greater heat-lift relative to the current MIRI cooler. NGAS uses ^{4}He as the circulating gas, as was used for MIRI. Ball uses a somewhat larger compressor and ^{3}He as the circulating gas. Both employ re-optimized heat exchangers. The NGAS project has completed PDR-level development, and is expected to reach CDR well before PICO begins Phase-A. The projected performance of this cooler is shown in Fig. 3.4; it gives 100 mW at 250 W input power, which is more than $100\,\%$ heat lift margin relative to PICO's requirements (Table 3.3). For PICO we assumed an input power of 350 W.

The entire precooler assembly and the J-T circulator compressor are located on the warm spacecraft spun module (Fig. 3.2). All waste heat rejected by the cooler compressors and drive electronics is transferred to the spacecraft heat rejection system. Unlike JWST, the PICO cooler does not require deployment of the remote cold head.

3.4.3 Radiative Cooling

A set of four V-groove radiators provides passive cooling. This is standard technology, with origins dating to more than 30 years ago (§ 6.3). The outermost of the four V-groove shields shadows the interior shields from the Sun. The V-grooves radiate to space, each reaching successively cooler temperatures. The V-groove assembly provides a cold radiative environment to the primary reflector, structural ring, and telescope box, so radiative loads on those elements are smaller than the conductive loads through the mechanical support structures.

3.5 Instrument Integration and Test

PICO instrument I&T planning benefits greatly from heritage experience with the *Planck* HFI instrument [255].

PICO screens detector wafer performance prior to selection of flight wafers and focal plane integration. The cADR and 4 K cryocooler are qualified prior to delivery. The relative alignment of the two reflectors under thermal contraction is photogrammetrically verified in a thermal vacuum (TVAC) chamber.

PICO integrates the flight focal plane assembly and flight cADR in a dedicated sub-kelvin cryogenic testbed. Noise, responsivity, and focal-plane temperature stability are characterized using a representative optical load for each frequency band (temperature-controlled blackbody). Polarimetric and spectroscopic calibration are performed.

The focal plane is integrated with the reflectors and structures, and alignment verified photogrammetrically at cold temperatures in a TVAC chamber. The completely integrated observatory (instrument and spacecraft bus) is tested in TVAC to measure parasitic optical loading from the instrument, noise, microphonics, and radio-frequency interference (RFI). The observatory is 4.5 m in diameter and 6.1 m tall, with no deployables.

4 Design Reference Mission

The PICO design reference mission is summarized in Table 4.1.

4.1 Concept of Operations

The PICO concept of operations is similar to that of the successful *WMAP* [256] and *Planck* [257] missions. After launch, PICO cruises to a quasi-halo orbit around the Earth–Sun L2 Lagrange point (§ 4.1.1). A two-week decontamination period is followed by instrument cooldown, lasting about two months. After in-orbit checkout is complete, PICO begins the science survey.

Table 4.1: PICO carries margin on key mission parameters. Maximum Expected Value (MEV) includes contingency.

Orbit type	Sun-Earth L2 Quasi-Halo
Mission class	Class B
Mission duration	5 years
Propellant (hydrazine)	213 kg (77 % tank fill)
Launch mass (MEV)	2147 kg (3195 kg capability)
Max power (MEV)	1320 W (with 125 % margin on available solar array area)
Onboard data storage	4.6 Tb (3 days of compressed data, enabling retransmission)
Survey implementation	Instrument on spin table
Attitude control	Zero-momentum 3-axis stabilized

PICO has a single science observing mode, surveying the sky continuously for 5 years using a pre-planned repetitive survey pattern (§ 4.1.2). Instrument data are compressed and stored on-board, then returned to Earth in daily 4-hr Ka-band science downlink passes (concurrent with science observations). Because PICO is observing relatively static Galactic, extragalactic, and cosmological targets, there are no requirements for time-critical observations or data latency. Presently, there are no plans for targets of opportunity or guest observer programs during the prime mission. The PICO instrument does not require cryogenic consumables (as the *Planck* mission did), permitting consideration of significant mission extension beyond the prime mission.

4.1.1 Mission Design and Launch

PICO performs its science survey from a quasi-halo orbit around the Earth–Sun L2 Lagrange point. Predecessor missions *Planck* and *WMAP* both operated in L2 orbits.

L2 orbits provide favorable survey geometry (relative to Earth orbits) by mitigating viewing restrictions imposed by terrestrial and lunar stray light. The PICO orbit around L2 is small enough to ensure than the Sun–Probe–Earth (SPE) angle is less than 15°. This maintains the telescope boresight $> 70^\circ$ away from the Earth (Fig. 4.2, $70^\circ = 180^\circ - \alpha - \beta -$ SPE).

High data rate downlink to the Deep Space Network (DSN) is available from L2 using near-Earth Ka bands. L2 provides a stable thermal environment, simplifying thermal control. The PICO orbit exhibits no post-launch eclipses.

NASA requires that Probes be compatible with an Evolved Expendable Launch Vehicle (EELV). For the purpose of this study, the Falcon 9 [258] is used as the reference vehicle. Figure 4.1 shows PICO configured for launch in a Falcon 9 fairing. The Falcon 9 launch capability for ocean recovery exceeds PICO's 2147 kg total launch mass (including contingency) by a $\sim 50\,\%$ margin.

Insertion to the halo manifold and associated trajectory correction maneuvers (TCMs) require $150\,\mathrm{m\,s^{-1}}$ of total ΔV by the spacecraft. Orbit maintenance requires minimal propellant (statistical $\Delta V \sim 2\,\mathrm{m\,s^{-1}\,year^{-1}}$). The orbital period is ~ 6 months. There are no disposal requirements for L2 orbits, but spacecraft are customarily decommissioned to heliocentric orbit.

4.1.2 Survey Design

PICO employs a highly repetitive scan strategy to map the full sky. During the survey, PICO spins with a period $T_{\mathrm{spin}} = 1$ min about a spin axis oriented $\alpha = 26^\circ$ from the anti-solar direction (Fig. 4.2). This spin axis is forced to precess about the anti-solar direction with a period $T_{\mathrm{prec}} = 10$ hr. The telescope boresight is oriented at an angle $\beta = 69^\circ$ away from the spin axis (Fig. 3.1). This β angle is chosen such that $\alpha + \beta > 90^\circ$, enabling mapping of all ecliptic latitudes. The precession axis tracks with the Earth in its yearly orbit around the Sun, so this scan strategy maps the full sky (all ecliptic longitudes) within 6 months.

PICO's $\alpha = 26^\circ$ is chosen to be substantially larger than the *Planck* mission's α angle (7.5°) to mitigate systematic effects by scanning across each sky pixel with a greater diversity of orientations [259]. Increasing α further would decrease the sun-shadowed volume available for the optics and consequently reduce the telescope aperture size. A deployable sun shade was considered but found not to be required, and was thus excluded in favor of a more conservative and less costly approach.

The instrument spin rate, selected through a trade study, matches that of the *Planck* mission. The study balanced low-frequency ($1/f$) noise subtraction (improves with spin rate) against implementation cost and heritage, pointing reconstruction ability (anti-correlated with spin rate), and data volume (linearly correlated with spin rate). The CMB dipole appears in the PICO data timestream at the spin frequency (1 rpm = 16.7 mHz). Higher multipole signals appear at harmonics of the spin frequency starting at 33 mHz, above the knee in the detector low-frequency noise (§ 3.2.3). A destriping mapmaker applied in data post-processing effectively operates as a high-pass filter, as demonstrated by *Planck* [260]. PICO's spin axis precession frequency is $> 400\times$ faster than that of *Planck*, greatly reducing the effects of any residual $1/f$ noise by spreading the effects more isotropically across pixels.

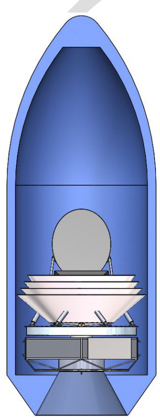

Figure 4.1: PICO is compatible with the Falcon 9.

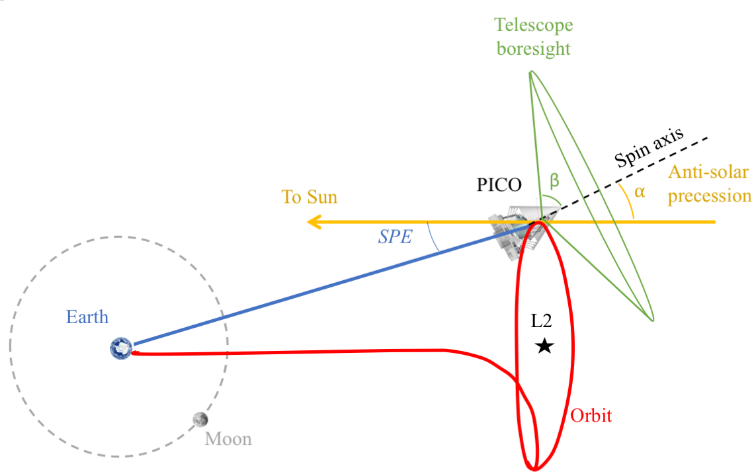

Figure 4.2: PICO surveys by continuously spinning the instrument about a precessing axis.

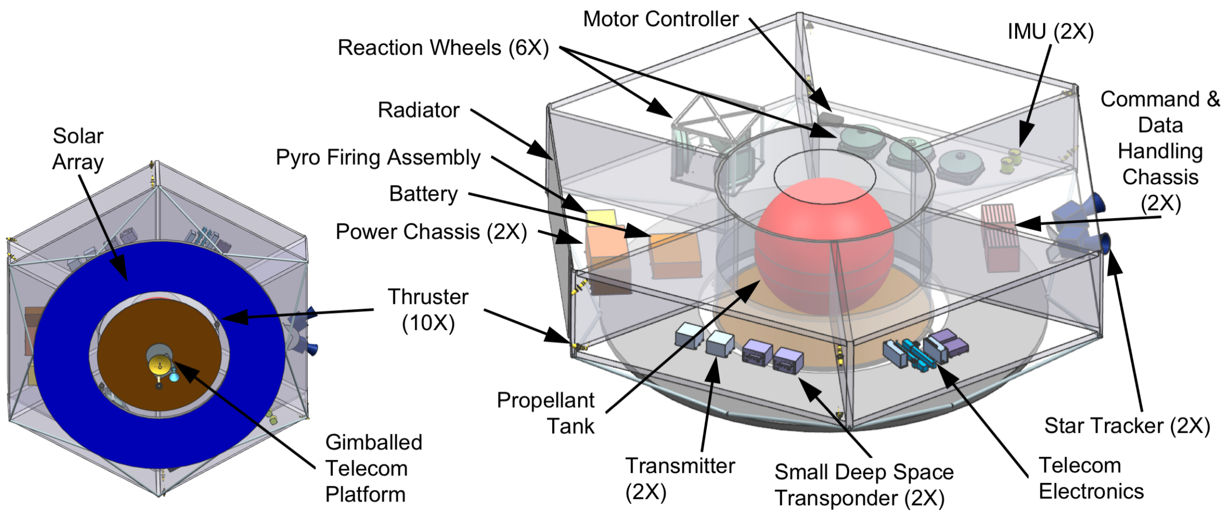

Figure 4.3: Modular equipment bays provide easy access to all components in the spacecraft de-spun module and enable parallel integration of spacecraft subsystems.

4.2 Ground Segment

The PICO Mission Operations System (MOS) and Ground Data System (GDS) can be built with extensive reuse of standard tools. The PICO concept of operations is described in § 4.1. All space-ground communications, ranging, and tracking are performed by the Deep Space Network (DSN) 34 m Beam Wave Guide (BWG). X-band is used to transmit spacecraft commanding, return engineering data, and provide navigation information (S-band is a viable alternative, and could be considered in a future trade). Ka-band is used for high-rate return of science data. The baseline 150 Mb/s transfer rate (130 Mb/s information rate after CCSDS encoding) is an existing DSN catalog service [*261*]. The instrument produces 6.1 Tb/day, which is compressed to 1.5 Tb/day (§ 3.3). Daily 4 hr DSN passes return PICO data in 3.1 hr, with the remaining 0.9 hr available as needed for retransmission or missed-pass recovery.

4.3 Spacecraft

The PICO spacecraft bus is Class B and designed for a minimum lifetime of 5 years in the L2 environment. Mission critical elements are redundant. Flight spares, engineering models and prototypes appropriate to Class B are budgeted.

The aft end of the spacecraft (the "de-spun module") is comprised of six equipment bays that house standard components (Fig. 4.3). The instrument and V-grooves are mounted on bipods from the spacecraft "spun module," which contains hosted instrument elements (Fig. 3.1). A motor drives the spun module at 1 rpm to support the science survey requirements (§ 4.1.2). Reaction wheels on the despun module cancel the angular momentum of the spun module and provide three-axis control (§ 4.3.1).

The bipods that mechanically support the instrument are thermally insulating. The passively radiating V-groove assembly thermally isolates the instrument from solar radiation and from the bus (§ 3.4.3). Like *Planck* [*257*], the V-grooves are manufactured using honeycomb material. Additional radiators on the spun and despun spacecraft modules ($\sim$ 1 m^2 each) reject heat dissipated by spacecraft subsystems and hosted instrument elements.

PICO's avionics are dual-string with standard interfaces. Solid state recorders provide three days of science data storage (4.6 Tbit), enabling retransmission of missed data.

PICO employs a fully redundant Ka- and X-band telecommunications architecture. The Ka-band system uses a 0.3 m high-gain antenna to support a science data downlink information rate of 130 Mb/s to a

34 m BWG DSN ground station with a link margin of 4.8 dB. The X-band system provides command and engineering telemetry communication through all mission phases using medium and low gain antennas. Amplifiers, switches, and all three antennas are on a gimballed platform, enabling Ka and X-band downlink concurrent with science observations.

The heritage power electronics are dual-string. A 74 A-hr Li-ion battery is sized for a 3 hr launch phase with 44 % depth of discharge. After the launch phase, the driving mode is telecom concurrent with science survey (1320 W including 43 % contingency). Solar cells on the aft side of the bus (5.8 m^2 array, $\alpha = 26°$ off-Sun) support this mode with positive power, and unused area in the solar array plane (7.4 m^2 more area by growing to 4.5 m diameter) affords 125 % margin (Fig. 4.3).

The propulsion design is a simple mono-propellant blow-down hydrazine system with standard redundancy. Two aft-pointed 22 N thrusters provide ΔV and attitude control for orbit insertion and maintenance (§ 4.1.1), requiring 140 kg of propellant. Eight 4 N thrusters provide reaction wheel momentum management and backup attitude control authority (60 kg of propellant). Accounting for ullage (14 kg), the baseline propellant tank fill fraction is 77 %.

4.3.1 Attitude Determination and Control

PICO uses a zero net angular momentum control architecture with heritage from the SMAP mission (§ 6.3). PICO's instrument spin rate (1 rpm) matches that of the *Planck* mission, but the precession of the spin axis is much faster (10 hr vs 6 months), and the precession angle much larger (26° vs 7.5°). These differences make the spin-stabilized *Planck* control architecture impractical because of the amount of torque that would be required to drive precession.

The PICO 1 rpm instrument spin rate is achieved and maintained using a spin motor. The spin motor drive electronics provide the coarse spin rate knowledge used for controlling the spin rate to meet the ± 0.1 rpm requirement. Data and power are passed across the interface using slip rings.

Based on mass properties derived from the PICO CAD model, PICO requires ~ 220 N m s to cancel the angular momentum of the instrument and spacecraft spun module (including mass contingency) at 1 rpm. Three Honeywell HR-16 reaction wheel assemblies (RWAs), each capable of 150 N m s, are mounted on the despun module parallel to the instrument spin axis, and spin opposite to the instrument to achieve zero net angular momentum. The despun module is three-axis stabilized. The spin axis is precessed using three RWAs mounted normal to the spin axis in a triangle configuration. Each set of three RWAs is sized such that two could perform the required function with margin, providing single fault tolerance.

Spin axis pointing and spin rate knowledge are achieved and maintained using star tracker and inertial measurement unit (IMU) data. The attitude determination system is single-fault tolerant, with two IMUs each on the spun and despun modules, and two star trackers each on the spun and despun modules. Two sun sensors on the despun module are used for safe-mode contingencies and instrument Sun avoidance. All attitude control and reconstruction requirements are met, including spin axis control < 60 arcmin with < 1 arcmin/min stability, and reconstructed pointing knowledge < 10 arcsec (each axis, 3σ).

Additional pointing reconstruction is performed in post-processing using the science data. The PICO instrument will observe planets (compact, bright sources) nearly every day. By fitting the telescope pointing to the known planetary ephemerides, the knowledge of the telescope boresight pointing and the relative pointing of each detector will improve to better than 1 arcsec (each axis, 3σ). *Planck*, with fewer detectors, making lower signal-to-noise ratio measurements of the planets, and observing with a scan strategy that acquired measurements of each planet only once every 6 months, demonstrated 0.8 arcsec (1σ) pointing reconstruction uncertainty in-scan and 1.9 arcsec (1σ) cross-scan [262].

5 Technology Maturation

PICO builds off of the heritage of *Planck*-HFI and *Herschel*. Since *Planck* and *Herschel*, suborbital experiments have used monolithically fabricated TES bolometers and multiplexing schemes to field instruments with thousands of TES bolometers per camera (Fig. 5.1). By the time PICO enters Phase A, the Simons Observatory plans to be operating 60,000 TES bolometers [263].

The remaining technology developments required to enable the PICO baseline design are:

1. Extension of three-color antenna-coupled bolometers down to 21 GHz and up to 462 GHz (§ 5.1).
2. Construction of high-frequency direct absorbing arrays and laboratory testing (§ 5.2).
3. Beam line and 100 mK testing to simulate the cosmic ray environment at L2 (§ 5.3).
4. Expansion of time-division multiplexing to support 128 switched rows per readout column (§ 5.4).

All of these developments are straightforward extensions of technologies already available today. We recommend APRA and SAT support to complete development of these technologies through the milestones described in Table 5.1.

5.1 21–462 GHz Bands

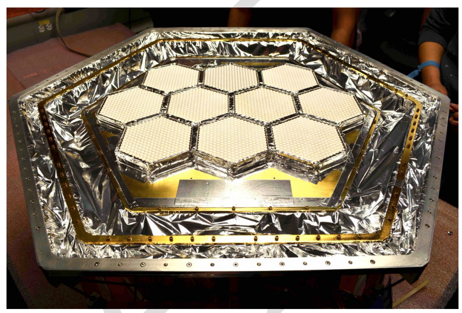

Figure 5.1: SPT-3G operates a focal plane with sinuous antenna-coupled, three-band pixels with 16,000 bolometers [264]. Each pixel couples radiation to bands at 95, 150, and 220 GHz.

Suborbital teams have successfully demonstrated a variety of optical coupling schemes, including horns with orthomode transducers (OMTs), lithographed antenna arrays, and sinuous antennas under lenslets (Table 5.2). All have achieved background-limited performance in suborbital instruments with sufficient margin on design parameters to achieve this performance in the lower background environment at L2. All have been packaged into modules and focal plane units in working cameras representative of the PICO integration. Experiments have covered many of PICO's observing bands between 27 GHz and 270 GHz (Table 5.2). To date, suborbital experiments have achieved statistical map depths of 3 μK_{CMB} arcmin on degree-scaled modes over small parts of the sky, within an order of magnitude of what PICO achieves over the entire sky (Table 3.2), and have demonstrated systematic control better than this level through full-pipeline simulations and null-test analysis (jackknife tests).

The baseline PICO instrument requires three-color dual-polarized antenna-coupled bolometers covering bands from 21 to 462 GHz (§ 3.2.1. The sinuous antenna has the bandwidth to service three bands per pixel, whereas horns and antenna arrays have only been used for two. Our baseline is to use a three-band sinuous antenna, although we have a design for PICO that uses two-bands per pixel and has the same baseline noise as PICO. It has a total of 19 bands instead of PICO's 21. SPT-3G has used the PICO-baselined three-color pixel design to deploy 16,000 detectors covering 90–150–220 GHz [264].

The extension to lower frequencies requires larger antennas and therefore control of film properties and lithography over larger areas. Scaling to higher frequencies requires tighter fabrication tolerances and materials tend to exhibit higher losses. Current anti-reflection technologies for the lenslets need to be extended with thicker and thinner layers to cover the lowest and highest frequency channels. These developments will require tight control of cleanliness and understanding of process parameters. All developments require careful characterization of beam properties.

The direction of polarization sensitivity of the sinuous antenna varies with frequency. Over 25% bandwidth, the variation is approximately ± 5 deg. There are potential solutions to this in the focal plane design, analysis, and free parameters of the antenna geometry. Systematics studies for field demonstrations will be particularly important. The PICO concept is robust to any challenges in developing three-color pixels; § 5.5

Table 5.1: PICO technologies can be developed to TRL 5 prior to a 2023 Phase A start using the APRA and SAT programs, requiring a total of about $ 13M. Per NASA guidance, these costs are outside the mission cost (§ 6.5).

Task	Current status	Milestone A	Milestone B	Milestone C	Current funding	Required funding	Date TRL5 achieved
1a. Three-color arrays $\nu < 90$ GHz	2-color lab demos $\nu > 30$ GHz	Field demo of 30–40 GHz (2020)	Lab demos 20–90 GHz (2022)	–	APRA & SAT funds	$2.5M over 4 yr (1 APRA + 1 SAT)	2022
1b. Three-color arrays $\nu > 220$ GHz	2-color lab demos $\nu < 300$ GHz	Field demo of 150–270 GHz (2021)	Lab demos 150-460 GHz (2022)	–	APRA & SAT funds	$3.5M over 4 yr (2 SATs)	2022
2. Direct absorbing arrays $\nu > 50$ GHz	0.1–5 THz unpolarized	Design & prototype of arrays (2021)	Lab demo of 555 GHz (2022)	Lab demo of 799 GHz (2023)	None	$2M over 5 yr (1 SAT)	2023
3. Cosmic ray studies	250 mK w/ sources	100 mK tests with sources (2021)	Beamline tests (2023)	–	APRA & SAT funds	$0.5–1M over 5 yr (part of 1 SAT)	–
4a. Fast readout electronics	MUX66 demo	Engineering and Fab of electronics (2020)	Lab demo (2021)	Field demo (2023)	No direct funds	$4M over 5 yr (1 SAT)	2023
4b. System engineering; 128× MUX demo	MUX66 demo	Design of cables (2020)	Lab demo (2021)	Field demo (2023)	No direct funds		

describes an option to descope to two-color horn-coupled pixels.

5.2 555–799 GHz bands

The baseline PICO instrument requires single-color, horn-coupled, dual-polarization, direct-absorbing bolometers from 555 to 799 GHz (§ 3.2.2). *Planck*and *Herschel* demonstrated the architecture of horns coupled to direct absorbing bolometers (Fig. 5.2). Ground experiments with similar designs have deployed focal planes with hundreds of horn-coupled spiderweb bolometers, replacing the *Planck* and *Herschel* NTD-Ge thermistors with TESs, and adjusting time constants as necessary (Table 5.3). *Planck*-HFI, SPT-pol, and BICEP demonstrated dual-polarized detectors. *Herschel* and SPT-SZ demonstrated monolithic unpolarized detectors. PICO will require detectors that merge these two designs in monolithic dual-polarized arrays. Since all the components of the technology already exist, the remaining necessary development is the packaging. Filled arrays of detectors such as Backshort Under Ground (BUG) bolometers are also an option [265].

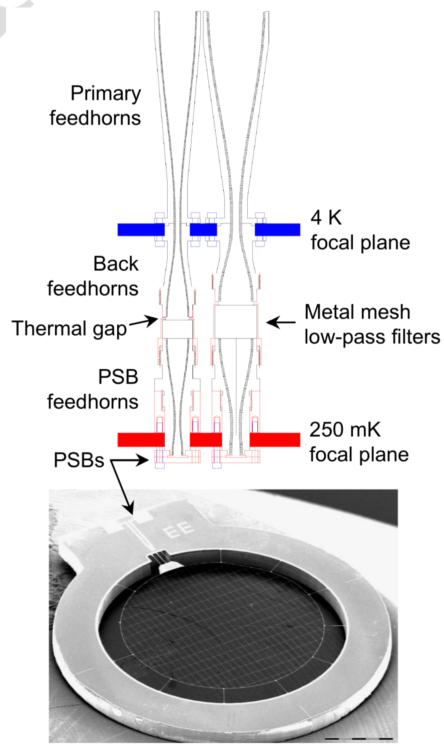

Figure 5.2: Top: *Planck* used horns to couple the electromagnetic radiation to its detectors. Horn coupling has been used in other experiments, and is the baseline for PICO's coupling between 555 and 799 GHz. Bottom: The photograph shows a dual-polarization, direct-absorbing bolometer from BICEP. The technology was also used with SPT-Pol and *Planck*-HFI for 143–343 GHz bands.

5.3 Environmental Testing

Laboratory tests and in-flight data from balloons suggest that TES bolometer arrays may be more naturally robust against cosmic rays than the individual NTD-Ge bolometers used in *Planck*. PICO will leverage lessons learned from *Planck* and ensure robust thermal sinking of detector array substrates. Cosmic ray glitches have fast recovery times and low coincidence rates [266, 267]. Residual risk

Table 5.2: Multiple active suborbital efforts are advancing technologies relevant to PICO.

Project	Type	Optical Coupling	ν_c [GHz]	Colors per pixel	N_{bolo}	Significance	Reference
PICO baseline	Probe		21 – 462	Three	11,796		§ 3.2.1
SPT-3G	Ground	Sinuous	90 – 220	Three	16,260	Trichroic	[264]
Advanced ACT-pol	Ground	Horns	27 – 230	Two	3,072	Dichroic	[270]
BICEP/Keck	Ground	Antenna arrays	90 – 270	One	5,120	50 nK-deg	[31]
Berkeley, Caltech, NIST	Lab	Various	30 – 270	Various	–	Band coverage	[239, 271, 272]
SPIDER	Balloon	Antenna arrays	90 – 150	One	2,400	Stable to 10 mHz	[237]

Table 5.3: PICO high-frequency detectors leverage development and demonstration by *Planck*, *Herschel*, and SPT.

Project	Type	Polarized	Mono-lithic?	ν_c [GHz]	Colors per pixel	N_{bolo}	Significance	Reference
PICO baseline	Probe	Yes	Yes	555 – 799	One	1,200		§ 3.2.2
Planck HFI	Flight	143–343 GHz	No	143 – 857	One	48	TRL 9 polarized	[235]
Herschel	Flight	No	Yes	570 – 1200	One	270	TRL 9 monolothic	[273]
SPT-SZ	Ground	No	Yes	90 – 220	One	840	Monolithic array TESs	[233]
SPT-pol-90	Ground	Yes	No	90	One	180	Dual pol absorbing TESs	[274]

can be retired with 100 mK testing where the array heat sinking may be weaker, and beam-line tests to simulate the expected flight environment.

5.4 Multiplexing

More than ten experiments have used time-domain multiplexer (TDM) readout. SCUBA2 on JCMT has 10 000 pixels, nearly as many detectors as planned for PICO [268]. Most of these experiments have used 32-row multiplexing. Recently ACT has expanded this to 64-row multiplexing [238].

PICO's sensitivity requirements dictate the use of $\sim$ 13 000 transition-edge-sensor bolometers, requiring a highly multiplexed system. The PICO baseline design calls for TDM with 128 switched rows per readout column (TDM-128$\times$). The leap to TDM-128$\times$ requires:

- development of fast-switched room temperature electronics; and
- system engineering of room temperature to cryogenic row select cabling to ensure sufficiently fast row switch settling times.

The historical row revisit rate for bolometric instruments using 32$\times$ TDM has been 25 kHz [e.g., 229]. However, x-ray instruments using TDM routinely switch between rows at a rate of 160 ns [269]. The PICO baseline assumes a 160 ns switch rate and TDM-128$\times$, which dictates a row revisit rate (effective sampling rate) of 48.8 kHz. To limit aliased noise, PICO implements L/R filters in each readout channel with a bandwidth of 6 kHz, dictated by detector stability considerations and the required $\sim$ 1 kHz signal bandwidth. With these parameters and using the same TDM multiplexer SQUID design, the increased total noise due to aliasing will be limited to 15 %. The system engineering study will culminate in a demonstration of TDM-128$\times$ SQUID aliased noise below PICO detector sensitivity requirements.

5.5 Technology Descopes

A descope from three-color sinuous antenna/lenslet-coupled pixels to two-color horn-coupled pixels remains a viable alternative should the three-color technology not mature as planned. Descope studies suggest that a PICO-size focal plane using two-color horn-coupled pixels at the lower frequencies and the baseline one-color pixels at the higher frequencies would contain 8,840 detectors (compared to the baseline 12,966) and map in 19 colors (baseline 21). Because horns have a 2.3 : 1 bandwidth, each of the two bands in a pixel has 35 % bandwidth (compared to the baseline 25 %), which compensates for pixel count, resulting in 0.61 μK_{CMB} arcmin aggregate CBE map depth, which matches the PICO CBE map depth, and affords $> 40\,\%$ margin against the 0.87 μK_{CMB} arcmin baseline requirement (Table 3.2), but with coarser spectral resolution. Detailed analysis could be performed to assess the impact on signal component separation (§ 2.7).

5.6 Enhancing Technologies

The following technologies are neither required nor assumed by the PICO baseline concept. They represent opportunities to extend scientific capabilities or simplify engineering.

PICO baselines TDM readout because of its relative maturity and demonstrated sensitivity and stability in relevant science missions. Lab tests of Frequency Domain Multiplexing (FDM) suggest comparable performance with higher multiplexing factors and lower loads on cryogenic stages relative to TDM. Suborbital experiments such as SPT-3G have used frequency division multiplexing (FDM) to readout focal planes comparable in size to PICO.

Microwave frequency SQUID multiplexing can increase the multiplexing density and reduce the number of lines between the 4 K and ambient temperature stages [275, 276]. Kinetic Inductance Detectors (KIDs) and Thermal KIDs (TKIDs) can further reduce the wire count, obviate the SQUIDs, and dramatically simplify integration by performing multiplexing on the same substrate as the detectors themselves [277–279]. The cost to develop these technologies is $3–4M/year, with a high chance of reaching TRL-5 before Phase A.

6 Project Management, Heritage, Risk, and Cost

6.1 PICO Study Participants

The PICO study was open to the entire mm/sub-mm science community. Seven working groups were led by members of PICO's Executive Committee, which met weekly under the leadership of PI Shaul Hanany. More than 60 people participated in-person in two community workshops (November 2017 and May 2018).

The PICO engineering concept definition package was generated by Team X (the JPL concurrent design lab). The Team X study was supported by inputs from a JPL engineering team and Lockheed Martin.

The full list of study report contributors and endorsers is on page i.

6.2 Project Management Plan

PICO benefits from the experience of predecessor missions such as *Planck* and *WMAP*, as well as many years of investment in technology development and a multitude of suborbital experiments. In addition to demonstrated science and engineering capabilities, this heritage has developed a community of people with the expertise required to field a successful mission.

This study assumes mission management by JPL with a Principal Investigator leading a single science team. A Project Manager provides project oversight for schedule, budget, and deliverables. A Project Systems Engineer leads systems engineering activities and serves as the Engineering Technical Authority. A Mission Assurance Manager serves as the Independent Technical Authority. The PICO mission development schedule is shown in Fig. 6.1.

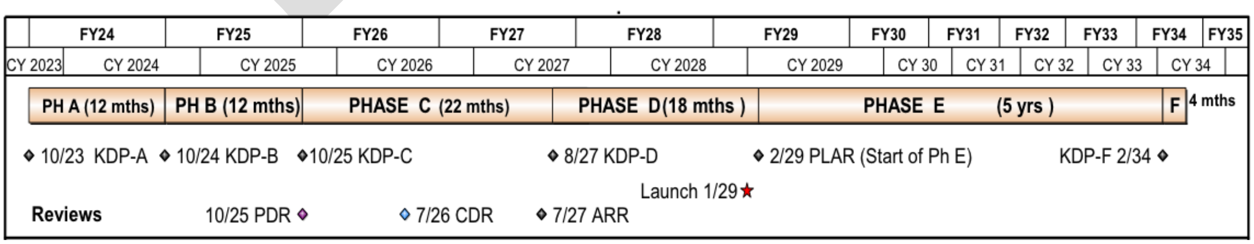

Figure 6.1: The PICO baseline schedule is based on historical actuals from similarly-sized missions such as Juno and SMAP. Per NASA direction, Probe studies assume a Phase A start in October 2023.

Probes are medium-class missions, similar in cost scope to NASA's New Frontiers missions, which are Category 1 and Risk Classification A or B, with Phase A–D costs capped at $\sim$ $850M (not including the launch vehicle). JPL is well-prepared to manage Probe missions, having managed the Juno New Frontiers mission (launched 2011) and also the development of the medium-class *Spitzer* Space Telescope (launched 2003). JPL delivered the bolometric detectors for the *Planck* HFI instrument (launched 2009). Presently, JPL is managing NEOCam, a Discovery class infrared space telescope.

The PICO spacecraft provider will be selected during mission formulation. Multiple organizations are capable of providing a spacecraft bus to meet PICO's requirements. Lockheed Martin contributed to the PICO concept study, leveraging their experience with New Frontiers missions Juno and OSIRIS-REx.

6.3 Heritage

The successful *Planck* mission provides science heritage for PICO. Technical heritage traces to multiple missions.

Because PICO observes in the mm/sub-mm regime, the surface accuracy requirement for the reflectors is relatively easy to meet. PICO's reflectors are similar to *Planck*'s, but somewhat larger (270 cm $\times$ 205 cm primary vs. 189 cm $\times$ 155 cm) [280]. *Herschel* observed at wavelengths more demanding than PICO's and was larger (350 cm diameter primary) [281].

The heritage of the PICO detectors and readout electronics (§ 3.2, § 3.3) is described in § 5.

PICO's detectors are cooled by a cADR (§ 3.4.1) with requirements that are within the capabilities of current ADRs developed by Goddard Space Flight Center. These systems have been applied to several JAXA missions, including *Hitomi* [251].

PICO's 4 K cryocooler (§ 3.4.2) is a direct extension of the JWST MIRI design [252, 253]. PICO benefits from a simpler and more reliable implementation of the J-T system than was required for MIRI, in that no deployment of cooling lines is required, and all flow valving is performed on the warm spacecraft. Cooling multiple independent points with a J-T loop has been demonstrated on *Planck* with the JPL-supplied 18 K cooler [282].

Structures similar to PICO's V-groove radiator assembly (§ 3.4.3) are a standard approach for passive cooling first described more than thirty years ago [283]. PICO has baselined a simple honeycomb material construction like that successfully flown by the *Planck* mission [282, 284].

Most requirements on the PICO spacecraft are well within typical ranges and can be met with standard high heritage systems (§ 4.3). PICO's spin architecture and data volume requirements are less typical, and discussed below.

PICO's spin system is generally less demanding than the successful SMAP spin system. PICO spins its instrument at 1 rpm, passes data and power across the spin interface (Fig. 3.2), and requires $\sim$ 220 N m s of spin momentum cancellation (§ 4.3.1). SMAP spins its 6-m instrument antenna at 14.6 rpm, successfully passes data and power across the spin interface, and requires 359 N m s of spin momentum cancellation [285].

Though PICO's data volume is notable by current standards, it is already enveloped by missions in development. PICO produces 6.1 Tb/day of raw data which is compressed to 1.5 Tb/day (§ 3.3). PICO downlinks data daily, but baselines storage of 3 days of (compressed) data to mitigate missed telecom passes. This requires 4.5 Tb of onboard storage, in family with the 3.14 Tb solid state recorder currently in use by Landsat 8 and much smaller than the 12 Tb flash memory planned for NISAR [286]. The PICO baseline 150 Mb/s Ka-band data downlink is an existing DSN catalog service [261]. The baseline PICO mission generates $\sim 2,200$ Tb of raw (uncompressed) data per year, less than the $\sim 6,800$ Tb/year currently returned by Landsat 8 and $\sim 9,300$ Tb/yr planned by NISAR [286].

6.4 Risk Assessment

6.4.1 Pre-Mission Risks

Technology development (§ 5) is performed prior to the beginning of mission development, and is outside of the mission cost (per NASA direction), so associated risks do not represent threats to the cost of mission development. Rather, these technology development risks affect the availability of the described baseline mission. A technology-related mission descope is described in § 5.5.

6.4.2 Development Risks

PICO's healthy contingencies, margins, and reserves provide flexibility to address risks realized during mission development. PICO carries $> 40\,\%$ instrument sensitivity margin (Table 3.2), $> 100\,\%$ heat lift margin (Table 3.3), 43 % system power contingency, 31 % payload mass contingency, and 25 % spacecraft mass contingency. The Falcon 9 launch capability (assuming ocean recovery) exceeds PICO's total launch mass (including contingency) by a $\sim 50\,\%$ margin. The PICO budget includes 30 % cost reserves for Phases A–D (§ 6.5).

During mission development the Project Systems Engineer continually assesses risks, tracks progress toward retiring them, and updates mitigations. Mitigations for a few top risks identified during this study are described below.

- Thermal risk can be mitigated through extensive thermal modeling and review in Phase A, and design for early test verification.
- Risks associated with the instrument spin architecture can be mitigated by engaging JPL engineers who were involved in the SMAP mission.
- Detector delivery schedule risk can be mitigated by beginning fabrication early in the project life cycle and fabricating a generous number of detector wafers to ensure adequate yield. Multiple institutions (including, for example, JPL, GSFC, NIST, and ANL) would be capable of producing the PICO detectors. Suborbital programs generally achieve $> 66\,\%$ detector wafer yield.
- Risks associated with the integration and test of a cryogenic instrument can be mitigated through advanced planning and allocation of appropriate schedule and schedule margin.

6.4.3 Operations Risks

The PICO design meets the requirements associated with the NASA Class B risk classification. For Class B missions, essential spacecraft and instrument functions are typically fully redundant. This increases mission cost, but significantly reduces the risk of mission failure.

The PICO mission utilizes a single instrument with a single observing mode mapping the sky using a repetitive survey pattern. The mission does not require any time-critical activities. The observatory fits in to the launch vehicle fairing in its operational configuration, so no hardware deployments are required. Because PICO observes at long wavelengths, the telescope does not require a dust cover (nor the associated mission-critical cover release).

The spacecraft incorporates a fault protection system for anomaly detection and resolution. The Sun-pointed, command receptive, thermally stable safe-mode attitude allows ground intervention for fault resolution without time constraints. PICO's high degree of hardware redundancy and onboard fault protection ensure spacecraft safety in the event of unforeseen failures and faults.

As described in § 2.7 and § 2.8, pre-Phase A simulation software maturation is recommended to mitigate the challenges associated with foreground separation and systematics control.

6.5 Mission Cost

We estimate PICO's total Phase A–E lifecycle cost between \$870M and \$960M, including the \$150M allocation for the Launch Vehicle (per NASA direction). These cost estimates include 30 % reserves for development (Phases A–D) and 13 % reserves for operations (Phase E). Pre-Phase-A technology maturation (§ 5) will be accomplished through the normal APRA and SAT processes, and is not included in the mission cost (per NASA direction).

Table 6.1: Detailed breakdown of Team X and PICO Team cost estimates (in FY18\$). Costs are based on the schedule in Fig. 6.1, which includes 5 years of operations.

<table>
<tr><th>Work Breakdown Structure (WBS) elements</th><th>Team X</th><th>PICO team</th></tr>
<tr><td>Development Cost (Phases A–D)</td><td>$ 724M</td><td>$ 634–677M</td></tr>
<tr><td>1.0, 2.0, 3.0 Management, Systems Engineering, and Mission Assurance</td><td>$ 54M</td><td>$ 47– 50M</td></tr>
<tr><td>4.0 Science</td><td colspan="2">$ 19M</td></tr>
<tr><td>5.0 Payload System</td><td colspan="2">$ 168M</td></tr>
<tr><td>6.0 Flight System</td><td>$ 248M</td><td>$ 210–240M</td></tr>
<tr><td>10.0 Assembly, Test, and Launch Operations (ATLO)</td><td>$ 24M</td><td></td></tr>
<tr><td>7.0 Mission Operations Preparation</td><td colspan="2">$ 16M</td></tr>
<tr><td>9.0 Ground Data Systems</td><td colspan="2">$ 21M</td></tr>
<tr><td>12.0 Mission and Navigation Design</td><td colspan="2">$ 7M</td></tr>
<tr><td>Development Reserves (30%)</td><td>$167M</td><td>$ 146–156M</td></tr>
<tr><td>Operations Cost (Phase E)</td><td colspan="2">$ 84M</td></tr>
<tr><td>1.0 Management</td><td colspan="2">$ 6M</td></tr>
<tr><td>4.0 Science</td><td colspan="2">$ 20M</td></tr>
<tr><td>7.0 Mission Operations</td><td colspan="2">$ 34M</td></tr>
<tr><td>9.0 Ground Data Systems</td><td colspan="2">$ 14M</td></tr>
<tr><td>Operations Reserves (13%)</td><td colspan="2">$ 10M</td></tr>
<tr><td>Launch Vehicle Cost</td><td colspan="2">$ 150M</td></tr>
<tr><td>Total Cost</td><td>$ 958M</td><td>$ 868–911M</td></tr>
</table>

Table 6.1 shows the mission cost breakdown, including the JPL Team X cost estimate as well as the PICO team cost estimate. Team X is JPL's concurrent design facility. Team X estimates are generally model-based, and were generated after a series of instrument and mission-level studies. Their accuracy is commensurate with the level of understanding typical to Pre-Phase-A concept development. They do not constitute an implementation or cost commitment on the part of JPL or Caltech.

The PICO team has generally adopted the Team X estimates, but also obtained a parametrically estimated cost range for the Flight System (WBS 6) and Assembly, Test and Launch Operations (ATLO, WBS 7) from Lockheed Martin Corporation to represent the cost benefits that might be realized by working with an industry partner. After adding estimated JPL overhead and Team X estimated V-groove assembly costs (not included in the Lockheed estimate), the PICO team cost is in-family with but lower than the Team X cost (Table 6.1).

Table 6.2: Detailed breakdown of PICO instrument costs.

Instrument Elements	Cost
Management, Systems Eng., Assurance	\$ 18M
4 K Cooler and 0.1 K cADR	\$ 71M
Focal plane and electronics	\$ 27M
Mechanical, Thermal, Software	\$ 17M
Telescope	\$ 6M
Instrument integration and test	\$ 29M
Total Instrument Cost	\$ 168M

Management, Systems Engineering, and Mission Assurance (WBS 1–3) development costs scale linearly with the WBS 4–12 development costs in the Team X model, and are adjusted accordingly in the PICO team estimate. Science team (WBS 4) costs are assessed by Team X based on PICO science team estimates of the numbers and types of contributors and meetings required for each year of PICO mission development and operations. These workforce estimates are informed by recent experience with the *Planck* mission.

Payload system (WBS 5) costs are discussed in detail in § 6.5.1. PICO's spacecraft (WBS 6) cost reflects a robust Class B architecture (§ 4.3). Mission-critical elements are redundant. Appropriate flight spares, engineering models and prototypes are budgeted. The V-groove assembly (§ 3.4.3) is costed in WBS 6. Mission operations (WBS 7), Ground Data Systems (WBS 9), and Mission Navigation and Design (WBS 12) costs reflect a relatively simple concept of operations (§ 4.1). PICO has a single instrument with a single science observing mode, surveying the sky continuously using a pre-planned repetitive survey pattern. Orbit maintenance activities are simple and infrequent.

6.5.1 Payload Cost

The PICO payload consists of a single instrument: an imaging polarimeter. Payload costs are tabulated in Table 6.2.

The superconducting detectors require sub-kelvin cooling to operate. The active cooling system (the 0.1 K cADR and 4 K cryocooler, § 3.4.1 and § 3.4.2) comprises nearly half of the payload cost. The cADR cost for this study is an estimate from NASA Goddard Space Flight Center (GSFC), and assumes the provision of both a flight model and an engineering model. GSFC has produced ADRs for multiple spaceflight missions. The 4 K cryocooler cost for this study is based on the NASA Instrument Cost Model (NICM) VIII CER Cryocooler model [287], assuming a commercial build. PICO benefits greatly from recent and ongoing investment by commercial suppliers of 4 K coolers (as described in § 3.4.2). Team X used NICM VIII to model the cost of the focal plane and dual string readout electronics (§ 3.2, § 3.3). Team X estimated the telescope cost using the Stahl model [288]. The telescope is not a major cost driver, primarily because the reflectors only need to be diffraction limited at 330 μm (900 GHz) (§ 3.1).

Based on JPL experience, 18 % of the instrument cost is allocated for integration and test. This includes integration and test of the flight focal-plane assembly with the flight cADR and then integration and test of the complete instrument including the focal-plane assembly, reflectors, structures, and coolers (§ 3.5). Integration and test of the instrument with the spacecraft is costed in WBS 10 (ATLO).

NASA Standard Template Cost Table

2020 Astrophysical Decadal Survey - Probe Mission Preparatory Study
Master Equipment List Based Parametric Total Lifecycle Cost Estimate

Mission Name / Acronym:	**PICO**
Cost Estimator:	JPL Team X
Date of Cost Estimate:	October 9, 2018
Cost Estimate Based On:	Final Master Equipment List

PROJECT PHASE		***COST [FY18 $M]***
Phase A		(see Note 1)
Phases B-D	Mgmt, SE, MA	$54
	Science	$19
	Telescope	$6
	Instrument	$162
	Spacecraft, including ATLO	$272
	MOS/GDS	$44
	Launch Vehicle and Services	$150
	Reserves	$167
	Total Cost Phases B-D	***$874***
Phase E-F	Operations	$74
	Reserves	$10
	Total Cost Phases E-F	**$84**
	TOTAL LIFECYCLE COST	**$958**

Notes:

- Team X estimates costs for Phase A-D. A break out of Phase A cost is not available. In this table, Phase A costs are included in Phase B-D.

- This parametric cost estimate is based on the Probe's Master Equipment List derived from the Final Engineering Concept Definition Package that accurately reflects the mission described in the Probe's Final Report. This estimate is to be used only for non-binding rough order of magnitude planning purposes.

- Team X estimates are generally model-based, and were generated after a series of instrument and mission level studies. Their accuracy is commensurate with the level of understanding typical to Pre-Phase-A concept development. They do not constitute an implementation or cost commitment on the part of JPL or Caltech.

References

[1] A. Mennella, M. Bersanelli, R. C. Butler *et al.*, “Planck early results. III. First assessment of the Low Frequency Instrument in-flight performance,” *Astron. Astrophys.*, vol. 536, p. A3, Dec. 2011. Retrieved from: http://adsabs.harvard.edu/abs/2011A%26A...536A...3M

[2] Planck HFI Core Team, P. A. R. Ade, N. Aghanim *et al.*, “Planck early results. IV. First assessment of the High Frequency Instrument in-flight performance,” *Astron. Astrophys.*, vol. 536, p. A4, Dec. 2011. Retrieved from: http://adsabs.harvard.edu/abs/2011A%26A...536A...4P

[3] U. Seljak and M. Zaldarriaga, “Signature of Gravity Waves in the Polarization of the Microwave Background,” *Physical Review Letters*, vol. 78, pp. 2054–2057, Mar. 1997. Retrieved from: http://adsabs.harvard.edu/abs/1997PhRvL..78.2054S

[4] M. Kamionkowski, A. Kosowsky, and A. Stebbins, “A Probe of Primordial Gravity Waves and Vorticity,” *Phys. Rev. Lett.*, vol. 78, pp. 2058–2061, Mar. 1997, astro-ph/9609132. Retrieved from: http://adsabs.harvard.edu/cgi-bin/nph-bib_query?bibcode=1997PhRvL..78.2058K&db_key=AST

[5] M. Zaldarriaga and U. Seljak, “All-sky analysis of polarization in the microwave background,” *Phys. Rev. D.*, vol. 55, pp. 1830–1840, Feb. 1997. Retrieved from: http://adsabs.harvard.edu/abs/1997PhRvD..55.1830Z

[6] M. Kamionkowski, A. Kosowsky, and A. Stebbins, “Statistics of cosmic microwave background polarization,” *Phys. Rev. D.*, vol. 55, pp. 7368–7388, Jun. 1997. Retrieved from: http://adsabs.harvard.edu/abs/1997PhRvD..55.7368K

[7] S. W. Henderson, R. Allison, J. Austermann *et al.*, “Advanced ACTPol Cryogenic Detector Arrays and Readout,” *Journal of Low Temperature Physics*, vol. 184, pp. 772–779, Aug. 2016. Retrieved from: http://adsabs.harvard.edu/abs/2016JLTP..184..772H

[8] B. A. Benson, P. A. R. Ade, Z. Ahmed *et al.*, “SPT-3G: a next-generation cosmic microwave background polarization experiment on the South Pole telescope,” in *Society of Photo-Optical Instrumentation Engineers (SPIE) Conference Series*, ser. Society of Photo-Optical Instrumentation Engineers (SPIE) Conference Series, vol. 9153, Jul. 2014, p. 1. Retrieved from: http://adsabs.harvard.edu/abs/2014SPIE.9153E..1PB

[9] N. Galitzki, A. Ali, K. S. Arnold *et al.*, “The Simons Observatory: instrument overview,” in *Millimeter, Submillimeter, and Far-Infrared Detectors and Instrumentation for Astronomy IX*, ser. Society of Photo-Optical Instrumentation Engineers (SPIE) Conference Series, vol. 10708, Jul. 2018, p. 1070804. Retrieved from: http://adsabs.harvard.edu/abs/2018SPIE10708E..04G

[10] T. Essinger-Hileman, A. Ali, M. Amiri *et al.*, “CLASS: the cosmology large angular scale surveyor,” in *Millimeter, Submillimeter, and Far-Infrared Detectors and Instrumentation for Astronomy VII*, ser. *Proceedings of SPIE*, vol. 9153, Jul. 2014, p. 91531I. Retrieved from: http://adsabs.harvard.edu/abs/2014SPIE.9153E..1IE

[11] H. Hui, P. A. R. Ade, Z. Ahmed *et al.*, “BICEP Array: a multi-frequency degree-scale CMB polarimeter,” in *Millimeter, Submillimeter, and Far-Infrared Detectors and Instrumentation for Astronomy IX*, ser. Society of Photo-Optical Instrumentation Engineers (SPIE) Conference Series, vol. 10708, Jul. 2018, p. 1070807. Retrieved from: http://adsabs.harvard.edu/abs/2018SPIE10708E..07H

[12] A. A. Fraisse, P. A. R. Ade, M. Amiri *et al.*, “SPIDER: probing the early Universe with a suborbital polarimeter,” *JCAP*, vol. 4, p. 47, Apr. 2013. Retrieved from: http://adsabs.harvard.edu/abs/2013JCAP...04..047F

[13] J. Lazear, P. A. R. Ade, D. Benford *et al.*, “The Primordial Inflation Polarization Explorer (PIPER),” in *Millimeter, Submillimeter, and Far-Infrared Detectors and Instrumentation for Astronomy VII*, ser. *Proceedings of SPIE*, vol. 9153, Jul. 2014, p. 91531L. Retrieved from: http://adsabs.harvard.edu/abs/2014SPIE.9153E..1LL

[14] A. H. Guth, “Inflationary universe: A possible solution to the horizon and flatness problems,” *Phys. Rev. D.*, vol. 23, pp. 347–356, Jan. 1981. Retrieved from: http://adsabs.harvard.edu/abs/1981PhRvD..23..347G

[15] A. D. Linde, “A new inflationary universe scenario: A possible solution of the horizon, flatness, homogeneity, isotropy and primordial monopole problems,” *Physics Letters B*, vol. 108, pp. 389–393, Feb. 1982. Retrieved from: http://adsabs.harvard.edu/abs/1982PhLB..108..389L

[16] A. Albrecht and P. J. Steinhardt, “Cosmology for grand unified theories with radiatively induced symmetry breaking,” *Physical Review Letters*, vol. 48, pp. 1220–1223, Apr. 1982. Retrieved from: http://adsabs.harvard.edu/abs/1982PhRvL..48.1220A

[17] A. A. Starobinsky, “A new type of isotropic cosmological models without singularity,” *Physics Letters B*, vol. 91, pp. 99–102, Mar. 1980. Retrieved from: http://adsabs.harvard.edu/abs/1980PhLB...91...99S

[18] V. F. Mukhanov and G. V. Chibisov, “Quantum fluctuations and a nonsingular universe,” *Soviet Journal of Experimental and Theoretical Physics Letters*, vol. 33, p. 532, May 1981. Retrieved from: http://adsabs.harvard.edu/abs/1981JETPL..33..532M

[19] A. H. Guth and S. Pi, “Fluctuations in the new inflationary universe,” *Phys. Rev. Lett.*, vol. 49, pp. 1110–1113, Oct. 1982. Retrieved from: http://adsabs.harvard.edu/cgi-bin/nph-bib_query?bibcode=1982PhRvL..49.1110G&db_key=AST

[20] S. W. Hawking, “The development of irregularities in a single bubble inflationary universe,” *Physics Letters B*, vol. 115, pp. 295–297, Sep. 1982. Retrieved from: http://adsabs.harvard.edu/cgi-bin/nph-bib_query?bibcode=1982PhLB..115..295H&db_key=PHY

[21] A. A. Starobinsky, “Dynamics of phase transition in the new inflationary universe scenario and generation of perturbations,” *Physics Letters B*, vol. 117, pp. 175–178, Nov. 1982. Retrieved from: http://adsabs.harvard.edu/abs/1982PhLB..117..175S

[22] J. M. Bardeen, P. J. Steinhardt, and M. S. Turner, “Spontaneous creation of almost scale-free density perturbations in an inflationary universe,” *Phys. Rev. D.*, vol. 28, p. 679, Aug. 1983. Retrieved from: http://adsabs.harvard.edu/cgi-bin/nph-bib_query?bibcode=1983PhRvD..28..679B&db_key=AST

[23] A. A. Starobinskiĭ, “Spectrum of relict gravitational radiation and the early state of the universe,” *Soviet Journal of Experimental and Theoretical Physics Letters*, vol. 30, p. 682, Dec. 1979. Retrieved from: http://adsabs.harvard.edu/abs/1979JETPL..30..682S

[24] The Polarbear Collaboration: P. A. R. Ade, Y. Akiba, A. E. Anthony *et al.*, “A Measurement of the Cosmic Microwave Background B-mode Polarization Power Spectrum at Sub-degree Scales with POLARBEAR,” *Ap. J.*, vol. 794, p. 171, Oct. 2014. Retrieved from: http://adsabs.harvard.edu/abs/2014ApJ...794..171T

[25] R. Keisler, S. Hoover, N. Harrington *et al.*, “Measurements of Sub-degree B-mode Polarization in the Cosmic Microwave Background from 100 Square Degrees of SPTpol Data,” *Ap. J.*, vol. 807, p. 151, Jul. 2015. Retrieved from: http://adsabs.harvard.edu/abs/2015ApJ...807..151K

[26] T. Louis, E. Grace, M. Hasselfield *et al.*, “The Atacama Cosmology Telescope: two-season ACTPol spectra and parameters,” *JCAP*, vol. 6, p. 031, Jun. 2017. Retrieved from: http://adsabs.harvard.edu/abs/2017JCAP...06..031L

[27] BICEP2 and Keck Array Collaboration, P. A. R. Ade, Z. Ahmed *et al.*, “Improved Constraints on Cosmology and Foregrounds from BICEP2 and Keck Array Cosmic Microwave Background Data with Inclusion of 95 GHz Band,” *Physical Review Letters*, vol. 116, no. 3, p. 031302, Jan. 2016. Retrieved from: http://adsabs.harvard.edu/abs/2016PhRvL.116c1302B

[28] Planck Collaboration, Y. Akrami, F. Arroja *et al.*, “Planck 2018 results. I. Overview and the cosmological legacy of Planck,” *arXiv e-prints*, Jul. 2018. Retrieved from: http://adsabs.harvard.edu/abs/2018arXiv180706205P

[29] R. Namba, M. Peloso, M. Shiraishi, L. Sorbo, and C. Unal, “Scale-dependent gravitational waves from a rolling axion,” *JCAP*, vol. 1, p. 041, Jan. 2016. Retrieved from: http://adsabs.harvard.edu/abs/2016JCAP...01..041N

[30] National Research Council, *New Worlds, New Horizons in Astronomy and Astrophysics*. Washington, DC: The National Academies Press, 2010. Retrieved from: https://www.nap.edu/catalog/12951/new-worlds-new-horizons-in-astronomy-and-astrophysics

[31] BICEP2 and Keck Array Collaborations, P. A. R. Ade, Z. Ahmed *et al.*, “BICEP2 / Keck Array X: Constraints on Primordial Gravitational Waves using Planck, WMAP, and New BICEP2/Keck Observations through the 2015 Season,” *arXiv e-prints*, Oct. 2018. Retrieved from: http://adsabs.harvard.edu/abs/2018arXiv181005216A

[32] The Simons Observatory Collaboration, P. Ade, J. Aguirre *et al.*, “The Simons Observatory: Science goals and forecasts,” *ArXiv e-prints*, Aug. 2018. Retrieved from: http://adsabs.harvard.edu/abs/2018arXiv180807445T

[33] L. M. Krauss and F. Wilczek, “Using cosmology to establish the quantization of gravity,” *Phys. Rev. D.*, vol. 89, no. 4, p. 047501, Feb. 2014. Retrieved from: http://adsabs.harvard.edu/abs/2014PhRvD..89d7501K

[34] Planck Collaboration, N. Aghanim, Y. Akrami *et al.*, “Planck 2018 results. VI. Cosmological parameters,” *arXiv e-prints*, Jul. 2018. Retrieved from: http://adsabs.harvard.edu/abs/2018arXiv180706209P

[35] A. S. Goncharov and A. D. Linde, “Chaotic inflation in supergravity,” *Physics Letters B*, vol. 139, pp. 27–30, May 1984. Retrieved from: http://adsabs.harvard.edu/abs/1984PhLB..139...27G

[36] U. Seljak and C. M. Hirata, “Gravitational lensing as a contaminant of the gravity wave signal in the CMB,” *Phys. Rev. D.*, vol. 69, no. 4, p. 043005, Feb. 2004. Retrieved from: http://adsabs.harvard.edu/abs/2004PhRvD..69d3005S

[37] K. M. Smith, D. Hanson, M. LoVerde, C. M. Hirata, and O. Zahn, “Delensing CMB polarization with external datasets,” *JCAP*, vol. 6, p. 014, Jun. 2012. Retrieved from: http://adsabs.harvard.edu/abs/2012JCAP...06..014S

[38] D. J. Watts, B. Wang, A. Ali *et al.*, “A Projected Estimate of the Reionization Optical Depth Using the CLASS Experiment’s Sample Variance Limited E-mode Measurement,” *Ap. J.*, vol. 863, p. 121, Aug. 2018. Retrieved from: http://adsabs.harvard.edu/abs/2018ApJ...863..121W

[39] Planck Collaboration, P. A. R. Ade, N. Aghanim *et al.*, “Planck 2015 results. XVII. Constraints on primordial non-Gaussianity,” *Astron. Astrophys.*, vol. 594, p. A17, Sep. 2016. Retrieved from: https://ui.adsabs.harvard.edu/#abs/2016A&A...594A..17P

[40] U. Seljak, “Extracting Primordial Non-Gaussianity without Cosmic Variance,” *Physical Review Letters*, vol. 102, no. 2, p. 021302, Jan. 2009. Retrieved from: http://adsabs.harvard.edu/abs/2009PhRvL.102b1302S

[41] M. Schmittfull and U. Seljak, “Parameter constraints from cross-correlation of CMB lensing with galaxy clustering,” *Phys. Rev. D.*, vol. 97, no. 12, p. 123540, Jun. 2018. Retrieved from: http://adsabs.harvard.edu/abs/2018PhRvD..97l3540S

[42] N. Dalal, O. Doré, D. Huterer, and A. Shirokov, “Imprints of primordial non-Gaussianities on large-scale structure: Scale-dependent bias and abundance of virialized objects,” *Phys. Rev. D.*, vol. 77, no. 12, p. 123514, Jun. 2008. Retrieved from: http://adsabs.harvard.edu/abs/2008PhRvD..77l3514D

[43] G. Steigman, “Cosmology confronts particle physics.” *Annual Review of Nuclear and Particle Science*, vol. 29, pp. 313–338, 1979. Retrieved from: http://adsabs.harvard.edu/abs/1979ARNPS..29..313S

[44] M. Bolz, A. Brandenburg, and W. Buchmüller, “Thermal production of gravitinos,” *Nuclear Physics B*, vol. 606, pp.

518–544, Jul. 2001. Retrieved from: http://adsabs.harvard.edu/abs/2001NuPhB.606..518B

[45] M. S. Madhavacheril, N. Sehgal, and T. R. Slatyer, "Current dark matter annihilation constraints from CMB and low-redshift data," *Phys. Rev. D.*, vol. 89, no. 10, p. 103508, May 2014. Retrieved from: http://adsabs.harvard.edu/abs/2014PhRvD..89j3508M

[46] D. Green, P. D. Meerburg, and J. Meyers, "Aspects of Dark Matter Annihilation in Cosmology," *ArXiv e-prints*, Apr. 2018. Retrieved from: http://adsabs.harvard.edu/abs/2018arXiv180401055G

[47] X. Chen, S. Hannestad, and R. J. Scherrer, "Cosmic microwave background and large scale structure limits on the interaction between dark matter and baryons," *Phys. Rev. D.*, vol. 65, no. 12, p. 123515, Jun. 2002. Retrieved from: http://adsabs.harvard.edu/abs/2002PhRvD..65l3515C

[48] K. Sigurdson, M. Doran, A. Kurylov, R. R. Caldwell, and M. Kamionkowski, "Dark-matter electric and magnetic dipole moments," *Phys. Rev. D.*, vol. 70, no. 8, p. 083501, Oct. 2004. Retrieved from: http://adsabs.harvard.edu/abs/2004PhRvD..70h3501S

[49] C. Dvorkin, K. Blum, and M. Kamionkowski, "Constraining dark matter-baryon scattering with linear cosmology," *Phys. Rev. D.*, vol. 89, no. 2, p. 023519, Jan. 2014. Retrieved from: http://adsabs.harvard.edu/abs/2014PhRvD..89b3519D

[50] V. Gluscevic and K. K. Boddy, "Constraints on Scattering of keV-TeV Dark Matter with Protons in the Early Universe," *Physical Review Letters*, vol. 121, no. 8, p. 081301, Aug. 2018. Retrieved from: http://adsabs.harvard.edu/abs/2018PhRvL.121h1301G

[51] K. K. Boddy and V. Gluscevic, "First cosmological constraint on the effective theory of dark matter- proton interactions," *Phys. Rev. D.*, vol. 98, p. 083510, Oct. 2018. Retrieved from: https://ui.adsabs.harvard.edu/#abs/2018PhRvD..98h3510B

[52] W. L. Xu, C. Dvorkin, and A. Chael, "Probing sub-GeV dark matter-baryon scattering with cosmological observables," *Phys. Rev. D.*, vol. 97, no. 10, p. 103530, May 2018. Retrieved from: http://adsabs.harvard.edu/abs/2018PhRvD..97j3530X

[53] K. K. Boddy, V. Gluscevic, V. Poulin, E. D. Kovetz, M. Kamionkowski, and R. Barkana, "Critical assessment of CMB limits on dark matter-baryon scattering: New treatment of the relative bulk velocity," *Phys. Rev. D.*, vol. 98, no. 12, p. 123506, Dec. 2018. Retrieved from: http://adsabs.harvard.edu/abs/2018PhRvD..98l3506B

[54] T. R. Slatyer and C.-L. Wu, "Early-Universe constraints on dark matter-baryon scattering and their implications for a global 21 cm signal," *Phys. Rev. D.*, vol. 98, no. 2, p. 023013, Jul. 2018. Retrieved from: http://adsabs.harvard.edu/abs/2018PhRvD..98b3013S

[55] R. Barkana, "Possible interaction between baryons and dark-matter particles revealed by the first stars," *Nature*, vol. 555, pp. 71–74, Mar. 2018. Retrieved from: http://adsabs.harvard.edu/abs/2018Natur.555...71B

[56] J. D. Bowman, A. E. E. Rogers, R. A. Monsalve, T. J. Mozdzen, and N. Mahesh, "An absorption profile centred at 78 megahertz in the sky-averaged spectrum," *Nature*, vol. 555, pp. 67–70, Mar. 2018. Retrieved from: http://adsabs.harvard.edu/abs/2018Natur.555...67B

[57] E. D. Kovetz, V. Poulin, V. Gluscevic, K. K. Boddy, R. Barkana, and M. Kamionkowski, "Tighter limits on dark matter explanations of the anomalous EDGES 21 cm signal," *Phys. Rev. D.*, vol. 98, no. 10, p. 103529, Nov. 2018. Retrieved from: http://adsabs.harvard.edu/abs/2018PhRvD..98j3529K

[58] B. J. Kavanagh, "Earth scattering of superheavy dark matter: Updated constraints from detectors old and new," *Phys. Rev. D.*, vol. 97, no. 12, p. 123013, Jun. 2018. Retrieved from: http://adsabs.harvard.edu/abs/2018PhRvD..97l3013K

[59] A. Arvanitaki, S. Dimopoulos, S. Dubovsky, N. Kaloper, and J. March-Russell, "String axiverse," *Phys. Rev. D.*, vol. 81, no. 12, p. 123530, Jun. 2010. Retrieved from: http://adsabs.harvard.edu/abs/2010PhRvD..81l3530A

[60] R. D. Peccei and H. R. Quinn, "CP conservation in the presence of pseudoparticles," *Physical Review Letters*, vol. 38, pp. 1440–1443, Jun. 1977. Retrieved from: http://adsabs.harvard.edu/abs/1977PhRvL..38.1440P

[61] S. Weinberg, "A new light boson?" *Physical Review Letters*, vol. 40, pp. 223–226, Jan. 1978. Retrieved from: http://adsabs.harvard.edu/abs/1978PhRvL..40..223W

[62] F. Wilczek, "Problem of strong P and T invariance in the presence of instantons," *Physical Review Letters*, vol. 40, pp. 279–282, Jan. 1978. Retrieved from: http://adsabs.harvard.edu/abs/1978PhRvL..40..279W

[63] Planck Collaboration, N. Aghanim, Y. Akrami *et al.*, "Planck 2018 results. VI. Cosmological parameters," *ArXiv e-prints*, Jul. 2018. Retrieved from: http://adsabs.harvard.edu/abs/2018arXiv180706209P

[64] M. Levi, C. Bebek, T. Beers *et al.*, "The DESI Experiment, a whitepaper for Snowmass 2013," *arXiv e-prints*, Aug. 2013. Retrieved from: http://adsabs.harvard.edu/abs/2013arXiv1308.0847L

[65] L. M. Widrow, "Origin of galactic and extragalactic magnetic fields," *Reviews of Modern Physics*, vol. 74, pp. 775–823, 2002. Retrieved from: http://adsabs.harvard.edu/abs/2002RvMP...74..775W

[66] L. M. Widrow, D. Ryu, D. R. G. Schleicher, K. Subramanian, C. G. Tsagas, and R. A. Treumann, "The First Magnetic Fields," *Space Science Reviews*, vol. 166, pp. 37–70, May 2012. Retrieved from: http://adsabs.harvard.edu/abs/2012SSRv..166...37W

[67] R. M. Athreya, V. K. Kapahi, P. J. McCarthy, and W. van Breugel, "Large rotation measures in radio galaxies at Z > 2," *Astron. Astrophys.*, vol. 329, pp. 809–820, Jan. 1998. Retrieved from: http://adsabs.harvard.edu/abs/1998A%26A...329..809A

[68] D. Grasso and H. R. Rubinstein, “Magnetic fields in the early Universe,” *Physics Reports*, vol. 348, pp. 163–266, Jul. 2001. Retrieved from: http://adsabs.harvard.edu/abs/2001PhR...348..163G

[69] T. Vachaspati, “Magnetic fields from cosmological phase transitions,” *Physics Letters B*, vol. 265, pp. 258–261, Aug. 1991. Retrieved from: http://adsabs.harvard.edu/abs/1991PhLB..265..258V

[70] M. S. Turner and L. M. Widrow, “Inflation-produced, large-scale magnetic fields,” *Phys. Rev. D.*, vol. 37, pp. 2743–2754, May 1988. Retrieved from: http://adsabs.harvard.edu/abs/1988PhRvD..37.2743T

[71] B. Ratra, “Cosmological 'seed' magnetic field from inflation,” *Ap. J. Lett.*, vol. 391, pp. L1–L4, May 1992. Retrieved from: http://adsabs.harvard.edu/abs/1992ApJ...391L...1R

[72] A. Díaz-Gil, J. García-Bellido, M. García Pérez, and A. González-Arroyo, “Magnetic Field Production during Preheating at the Electroweak Scale,” *Physical Review Letters*, vol. 100, no. 24, p. 241301, Jun. 2008. Retrieved from: http://adsabs.harvard.edu/abs/2008PhRvL.100x1301D

[73] N. Barnaby, R. Namba, and M. Peloso, “Observable non-Gaussianity from gauge field production in slow roll inflation, and a challenging connection with magnetogenesis,” *Phys. Rev. D.*, vol. 85, no. 12, p. 123523, Jun. 2012. Retrieved from: http://adsabs.harvard.edu/abs/2012PhRvD..85l3523B

[74] A. J. Long, E. Sabancilar, and T. Vachaspati, “Leptogenesis and primordial magnetic fields,” *JCAP*, vol. 2, p. 036, Feb. 2014. Retrieved from: http://adsabs.harvard.edu/abs/2014JCAP...02..036L

[75] R. Durrer and A. Neronov, “Cosmological magnetic fields: their generation, evolution and observation,” *Astronomy and Astrophysics Review*, vol. 21, p. 62, Jun. 2013. Retrieved from: http://adsabs.harvard.edu/abs/2013A%26ARv..21...62D

[76] Planck Collaboration, P. A. R. Ade, N. Aghanim *et al.*, “Planck 2015 results. XIX. Constraints on primordial magnetic fields,” *Astron. Astrophys.*, vol. 594, p. A19, Sep. 2016. Retrieved from: http://adsabs.harvard.edu/abs/2016A%26A...594A..19P

[77] K. E. Kunze and E. Komatsu, “Constraints on primordial magnetic fields from the optical depth of the cosmic microwave background,” *ArXiv:1501.00142*, Dec. 2015. Retrieved from: http://adsabs.harvard.edu/abs/2015arXiv150100142K

[78] J. Chluba, D. Paoletti, F. Finelli, and J.-A. Rubino-Martin, “Effect of primordial magnetic fields on the ionization history,” *ArXiv:1503.04827*, Mar. 2015. Retrieved from: http://adsabs.harvard.edu/abs/2015arXiv150304827C

[79] A. Zucca, Y. Li, and L. Pogosian, “Constraints on primordial magnetic fields from Planck data combined with the South Pole Telescope CMB B -mode polarization measurements,” *Phys. Rev. D.*, vol. 95, no. 6, p. 063506, Mar. 2017. Retrieved from: http://adsabs.harvard.edu/abs/2017PhRvD..95f3506Z

[80] A. Kosowsky and A. Loeb, “Faraday Rotation of Microwave Background Polarization by a Primordial Magnetic Field,” *Ap. J.*, vol. 469, pp. 1–+, Sep. 1996. Retrieved from: http://adsabs.harvard.edu/abs/1996ApJ...469....1K

[81] N. Oppermann, H. Junklewitz, G. Robbers *et al.*, “An improved map of the Galactic Faraday sky,” *Astron. Astrophys.*, vol. 542, p. A93, Jun. 2012. Retrieved from: http://adsabs.harvard.edu/abs/2012A%26A...542A..93O

[82] S. De, L. Pogosian, and T. Vachaspati, “CMB Faraday rotation as seen through the Milky Way,” *Phys. Rev. D.*, vol. 88, no. 6, p. 063527, Sep. 2013. Retrieved from: http://adsabs.harvard.edu/abs/2013PhRvD..88f3527D

[83] L. Pogosian, “Searching for primordial magnetism with multifrequency cosmic microwave background experiments,” *MNRAS*, vol. 438, pp. 2508–2512, Mar. 2014. Retrieved from: http://adsabs.harvard.edu/abs/2014MNRAS.438.2508P

[84] K. Freese, J. A. Frieman, and A. V. Olinto, “Natural inflation with pseudo Nambu-Goldstone bosons,” *Physical Review Letters*, vol. 65, pp. 3233–3236, Dec. 1990. Retrieved from: http://adsabs.harvard.edu/abs/1990PhRvL..65.3233F

[85] J. A. Frieman, C. T. Hill, A. Stebbins, and I. Waga, “Cosmology with Ultralight Pseudo Nambu-Goldstone Bosons,” *Physical Review Letters*, vol. 75, pp. 2077–2080, Sep. 1995. Retrieved from: http://adsabs.harvard.edu/abs/1995PhRvL..75.2077F

[86] S. M. Carroll, “Quintessence and the Rest of the World: Suppressing Long-Range Interactions,” *Physical Review Letters*, vol. 81, pp. 3067–3070, Oct. 1998. Retrieved from: http://adsabs.harvard.edu/abs/1998PhRvL..81.3067C

[87] N. Kaloper and L. Sorbo, “Of pNGB quiScript Ntessence,” *JCAP*, vol. 4, p. 007, Apr. 2006. Retrieved from: http://adsabs.harvard.edu/abs/2006JCAP...04..007K

[88] C. R. Contaldi, J. Magueijo, and L. Smolin, “Anomalous Cosmic-Microwave-Background Polarization and Gravitational Chirality,” *Phys. Rev. Lett.*, vol. 101, p. 141101, Oct. 2008. Retrieved from: https://ui.adsabs.harvard.edu/#abs/2008PhRvL.101n1101C

[89] V. Gluscevic and M. Kamionkowski, “Testing parity-violating mechanisms with cosmic microwave background experiments,” *Phys. Rev. D.*, vol. 81, no. 12, p. 123529, Jun. 2010. Retrieved from: http://adsabs.harvard.edu/abs/2010PhRvD..81l3529G

[90] D. Harari and P. Sikivie, “Effects of a Nambu-Goldstone boson on the polarization of radio galaxies and the cosmic microwave background,” *Physics Letters B*, vol. 289, pp. 67–72, Sep. 1992. Retrieved from: http://adsabs.harvard.edu/abs/1992PhLB..289...67H

[91] S. M. Carroll, G. B. Field, and R. Jackiw, “Limits on a Lorentz- and parity-violating modification of electrodynamics,” *Phys. Rev. D.*, vol. 41, pp. 1231–1240, Feb. 1990. Retrieved from: http://adsabs.harvard.edu/abs/1990PhRvD..41.1231C

[92] M. Kamionkowski, “How to Derotate the Cosmic Microwave Background Polarization,” *Physical Review Letters*, vol. 102, no. 11, p. 111302, Mar. 2009. Retrieved from: http://adsabs.harvard.edu/abs/2009PhRvL.102k1302K

[93] V. Gluscevic, M. Kamionkowski, and A. Cooray, "Derotation of the cosmic microwave background polarization: Full-sky formalism," *Phys. Rev. D.*, vol. 80, no. 2, p. 023510, Jul. 2009. Retrieved from: http://adsabs.harvard.edu/abs/2009PhRvD..80b3510G

[94] V. Gluscevic, D. Hanson, M. Kamionkowski, and C. M. Hirata, "First CMB constraints on direction-dependent cosmological birefringence from WMAP-7," *Phys. Rev. D.*, vol. 86, no. 10, p. 103529, Nov. 2012. Retrieved from: http://adsabs.harvard.edu/abs/2012PhRvD..86j3529G

[95] Planck Collaboration, N. Aghanim, M. Ashdown *et al.*, "Planck intermediate results. XLIX. Parity-violation constraints from polarization data," *Astron. Astrophys.*, vol. 596, p. A110, Dec. 2016. Retrieved from: http://adsabs.harvard.edu/abs/2016A%26A...596A.110P

[96] M. Pospelov, A. Ritz, and C. Skordis, "Pseudoscalar Perturbations and Polarization of the Cosmic Microwave Background," *Physical Review Letters*, vol. 103, no. 5, p. 051302, Jul. 2009. Retrieved from: http://adsabs.harvard.edu/abs/2009PhRvL.103e1302P

[97] BICEP2 and Keck Array Collaboration, P. A. R. Ade, Z. Ahmed *et al.*, "BICEP2 / Keck Array IX: New bounds on anisotropies of CMB polarization rotation and implications for axionlike particles and primordial magnetic fields," *Phys. Rev. D.*, vol. 96, no. 10, p. 102003, Nov. 2017. Retrieved from: http://adsabs.harvard.edu/abs/2017PhRvD..96j2003B

[98] P. Svrcek and E. Witten, "Axions in string theory," *Journal of High Energy Physics*, vol. 6, p. 051, Jun. 2006. Retrieved from: http://adsabs.harvard.edu/abs/2006JHEP...06..051S

[99] R. A. Monsalve, A. E. E. Rogers, J. D. Bowman, and T. J. Mozdzen, "Results from EDGES High-band. I. Constraints on Phenomenological Models for the Global 21 cm Signal," *Ap. J.*, vol. 847, p. 64, Sep. 2017. Retrieved from: http://adsabs.harvard.edu/abs/2017ApJ...847...64M

[100] X. Fan, M. A. Strauss, R. H. Becker *et al.*, "Constraining the Evolution of the Ionizing Background and the Epoch of Reionization with z˜6 Quasars. II. A Sample of 19 Quasars," *Astronomical Journal*, vol. 132, pp. 117–136, Jul. 2006. Retrieved from: http://adsabs.harvard.edu/abs/2006AJ....132..117F

[101] Planck Collaboration, R. Adam, N. Aghanim *et al.*, "Planck intermediate results. XLVII. Planck constraints on reionization history," *Astron. Astrophys.*, vol. 596, p. A108, Dec. 2016. Retrieved from: http://adsabs.harvard.edu/abs/2016A%26A...596A.108P

[102] V. Miranda, A. Lidz, C. H. Heinrich, and W. Hu, "CMB signatures of metal-free star formation and Planck 2015 polarization data," *MNRAS*, vol. 467, pp. 4050–4056, Jun. 2017. Retrieved from: http://adsabs.harvard.edu/abs/2017MNRAS.467.4050M

[103] E. Calabrese, R. Hložek, N. Battaglia *et al.*, "Precision epoch of reionization studies with next-generation CMB experiments," *JCAP*, vol. 8, p. 010, Aug. 2014. Retrieved from: http://adsabs.harvard.edu/abs/2014JCAP...08..010C

[104] K. M. Smith and S. Ferraro, "Detecting Patchy Reionization in the Cosmic Microwave Background," *Physical Review Letters*, vol. 119, no. 2, p. 021301, Jul. 2017. Retrieved from: http://adsabs.harvard.edu/abs/2017PhRvL.119b1301S

[105] C. Dvorkin and K. M. Smith, "Reconstructing patchy reionization from the cosmic microwave background," *Phys. Rev. D.*, vol. 79, no. 4, p. 043003, Feb. 2009. Retrieved from: http://adsabs.harvard.edu/abs/2009PhRvD..79d3003D

[106] Planck Collaboration, N. Aghanim, Y. Akrami *et al.*, "Planck 2018 results. VIII. Gravitational lensing," *ArXiv e-prints*, Jul. 2018. Retrieved from: http://adsabs.harvard.edu/abs/2018arXiv180706210P

[107] LSST Science Collaboration, P. A. Abell, J. Allison *et al.*, "LSST Science Book, Version 2.0," *arXiv e-prints*, Dec. 2009. Retrieved from: http://adsabs.harvard.edu/abs/2009arXiv0912.0201L

[108] B. Yu, R. Z. Knight, B. D. Sherwin, S. Ferraro, L. Knox, and M. Schmittfull, "Towards Neutrino Mass from Cosmology without Optical Depth Information," *arXiv e-prints*, Sep. 2018. Retrieved from: http://adsabs.harvard.edu/abs/2018arXiv180902120Y

[109] J. S. Dunlop, "Observing the First Galaxies," in *The First Galaxies*, ser. Astrophysics and Space Science Library, T. Wiklind, B. Mobasher, and V. Bromm, Eds., vol. 396, 2013, p. 223. Retrieved from: http://adsabs.harvard.edu/abs/2013ASSL..396..223D

[110] M. Schmittfull and U. Seljak, "Parameter constraints from cross-correlation of CMB lensing with galaxy clustering," *Phys. Rev. D.*, vol. 97, no. 12, p. 123540, Jun. 2018. Retrieved from: http://adsabs.harvard.edu/abs/2018PhRvD..97l3540S

[111] Y. Ono, M. Ouchi, Y. Harikane *et al.*, "Great Optically Luminous Dropout Research Using Subaru HSC (GOLDRUSH). I. UV luminosity functions at z 4-7 derived with the half-million dropouts on the 100 $\deg^2$ sky," *Publications of the Astronomical Society of Japan*, vol. 70, p. S10, Jan. 2018. Retrieved from: http://adsabs.harvard.edu/abs/2018PASJ...70S..10O

[112] Y. Harikane, M. Ouchi, Y. Ono *et al.*, "GOLDRUSH. II. Clustering of galaxies at z 4-6 revealed with the half-million dropouts over the 100 $\deg^2$ area corresponding to 1 Gpc^3," *Publications of the Astronomical Society of Japan*, vol. 70, p. S11, Jan. 2018. Retrieved from: http://adsabs.harvard.edu/abs/2018PASJ...70S..11H

[113] E. J. Baxter, R. Keisler, S. Dodelson *et al.*, "A Measurement of Gravitational Lensing of the Cosmic Microwave Background by Galaxy Clusters Using Data from the South Pole Telescope," *Ap. J.*, vol. 806, p. 247, Jun. 2015. Retrieved from: http://adsabs.harvard.edu/abs/2015ApJ...806..247B

[114] M. Madhavacheril, N. Sehgal, R. Allison *et al.*, "Evidence of lensing of the cosmic microwave background by dark matter

halos," *Phys. Rev. Lett.*, vol. 114, p. 151302, Apr 2015. Retrieved from: https://link.aps.org/doi/10.1103/PhysRevLett.114.151302

[115] Planck Collaboration, P. A. R. Ade, N. Aghanim *et al.*, "Planck 2015 results. XXIV. Cosmology from Sunyaev-Zeldovich cluster counts," *Astron. Astrophys.*, vol. 594, p. A24, Sep. 2016. Retrieved from: http://adsabs.harvard.edu/abs/2016A%26A...594A..24P

[116] J.-B. Melin and J. G. Bartlett, "Measuring cluster masses with CMB lensing: a statistical approach," *Astron. Astrophys.*, vol. 578, p. A21, Jun. 2015. Retrieved from: http://adsabs.harvard.edu/abs/2015A%26A...578A..21M

[117] Y. B. Zeldovich and R. A. Sunyaev, "The Interaction of Matter and Radiation in a Hot-Model Universe," *ApSS*, vol. 4, pp. 301–316, Jul. 1969. Retrieved from: http://adsabs.harvard.edu/abs/1969Ap%26SS...4..301Z

[118] R. A. Sunyaev and Y. B. Zeldovich, "The Observations of Relic Radiation as a Test of the Nature of X-Ray Radiation from the Clusters of Galaxies," *Comments on Astrophysics and Space Physics*, vol. 4, p. 173, Nov. 1972. Retrieved from: http://adsabs.harvard.edu/abs/1972CoASP...4..173S

[119] J. L. Sievers, R. A. Hlozek, M. R. Nolta *et al.*, "The Atacama Cosmology Telescope: cosmological parameters from three seasons of data," *JCAP*, vol. 10, p. 060, Oct. 2013. Retrieved from: http://adsabs.harvard.edu/abs/2013JCAP...10..060S

[120] E. M. George, C. L. Reichardt, K. A. Aird *et al.*, "A Measurement of Secondary Cosmic Microwave Background Anisotropies from the 2500 Square-degree SPT-SZ Survey," *Ap. J.*, vol. 799, p. 177, Feb. 2015. Retrieved from: http://adsabs.harvard.edu/abs/2015ApJ...799..177G

[121] J. Delabrouille, J.-F. Cardoso, M. Le Jeune, M. Betoule, G. Fay, and F. Guilloux, "A full sky, low foreground, high resolution CMB map from WMAP," *Astron. Astrophys.*, vol. 493, pp. 835–857, Jan. 2009. Retrieved from: http://adsabs.harvard.edu/abs/2009A%26A...493..835D

[122] J. Delabrouille, M. Betoule, J. B. Melin *et al.*, "The pre-launch Planck Sky Model: a model of sky emission at submillimetre to centimetre wavelengths," *Astron. Astrophys.*, vol. 553, p. A96, May 2013. Retrieved from: https://ui.adsabs.harvard.edu/#abs/2013A&A...553A..96D

[123] L. Verde, "Statistical Methods in Cosmology," in *Lecture Notes in Physics, Berlin Springer Verlag*, ser. Lecture Notes in Physics, Berlin Springer Verlag, G. Wolschin, Ed., vol. 800, Mar. 2010, pp. 147–177. Retrieved from: http://adsabs.harvard.edu/abs/2010LNP...800..147V

[124] Planck Collaboration, N. Aghanim, Y. Akrami *et al.*, "Planck 2018 results. XII. Galactic astrophysics using polarized dust emission," *ArXiv e-prints*, Jul. 2018. Retrieved from: https://ui.adsabs.harvard.edu/#abs/2018arXiv180706212P

[125] D. T. Chuss, B.-G. Andersson, J. Bally *et al.*, "HAWC+/SOFIA Multiwavelength Polarimetric Observations of OMC-1," *ArXiv e-prints*, Oct. 2018. Retrieved from: https://ui.adsabs.harvard.edu/#abs/2018arXiv181008233C

[126] F. Bacciotti, J. M. Girart, M. Padovani *et al.*, "ALMA Observations of Polarized Emission toward the CW Tau and DG Tau Protoplanetary Disks: Constraints on Dust Grain Growth and Settling," *Ap. J.*, vol. 865, p. L12, Oct. 2018. Retrieved from: https://ui.adsabs.harvard.edu/#abs/2018ApJ...865L..12B

[127] C. H. Smith, C. M. Wright, D. K. Aitken, P. F. Roche, and J. H. Hough, "Studies in mid-infrared spectropolarimetry - II. An atlas of spectra," *MNRAS*, vol. 312, pp. 327–361, Feb. 2000. Retrieved from: http://adsabs.harvard.edu/abs/2000MNRAS.312..327S

[128] J. E. Chiar, A. J. Adamson, D. C. B. Whittet *et al.*, "Spectropolarimetry of the 3.4 μm Feature in the Diffuse ISM toward the Galactic Center Quintuplet Cluster," *Ap. J.*, vol. 651, pp. 268–271, Nov. 2006. Retrieved from: http://adsabs.harvard.edu/abs/2006ApJ...651..268C

[129] R. E. Mason, G. S. Wright, A. Adamson, and Y. Pendleton, "Spectropolarimetry of the 3.4 μm Absorption Feature in NGC 1068," *Ap. J.*, vol. 656, pp. 798–804, Feb. 2007. Retrieved from: http://adsabs.harvard.edu/abs/2007ApJ...656..798M

[130] Planck Collaboration, P. A. R. Ade, M. I. R. Alves *et al.*, "Planck intermediate results. XXII. Frequency dependence of thermal emission from Galactic dust in intensity and polarization," *Astron. Astrophys.*, vol. 576, p. A107, Apr. 2015. Retrieved from: http://adsabs.harvard.edu/abs/2015A%26A...576A.107P

[131] P. C. Ashton, P. A. R. Ade, F. E. Angilè *et al.*, "First Observation of the Submillimeter Polarization Spectrum in a Translucent Molecular Cloud," *Ap. J.*, vol. 857, p. 10, Apr. 2018. Retrieved from: http://adsabs.harvard.edu/abs/2018ApJ...857...10A

[132] A. M. Meisner and D. P. Finkbeiner, "Modeling Thermal Dust Emission with Two Components: Application to the Planck High Frequency Instrument Maps," *Ap. J.*, vol. 798, p. 88, Jan. 2015. Retrieved from: https://ui.adsabs.harvard.edu/#abs/2015ApJ...798...88M

[133] B. T. Draine and A. A. Fraisse, "Polarized Far-Infrared and Submillimeter Emission from Interstellar Dust," *Ap. J.*, vol. 696, pp. 1–11, May 2009. Retrieved from: http://adsabs.harvard.edu/abs/2009ApJ...696....1D

[134] V. Guillet, L. Fanciullo, L. Verstraete *et al.*, "Dust models compatible with Planck intensity and polarization data in translucent lines of sight," *Astron. Astrophys.*, vol. 610, p. A16, Feb. 2018. Retrieved from: http://adsabs.harvard.edu/abs/2018A%26A...610A..16G

[135] B. T. Draine and B. Hensley, "Magnetic Nanoparticles in the Interstellar Medium: Emission Spectrum and Polarization," *Ap. J.*, vol. 765, p. 159, Mar. 2013. Retrieved from: http://adsabs.harvard.edu/abs/2013ApJ...765..159D

[136] C. Dickinson, Y. Ali-Haïmoud, A. Barr *et al.*, "The State-of-Play of Anomalous Microwave Emission (AME) research,"

New Ast. Rev., vol. 80, pp. 1–28, Feb. 2018. Retrieved from: http://adsabs.harvard.edu/abs/2018NewAR..80....1D

[137] C. Dickinson, A. Barr, H. C. Chiang *et al.*, "The C-Band All-Sky Survey (C-BASS): Constraining diffuse Galactic radio emission in the North Celestial Pole region," *ArXiv e-prints*, Oct. 2018. Retrieved from: https://ui.adsabs.harvard.edu/#abs/2018arXiv181011681D

[138] S. E. Clark, J. E. G. Peek, and M. E. Putman, "Magnetically Aligned H I Fibers and the Rolling Hough Transform," *Ap. J.*, vol. 789, p. 82, Jul. 2014. Retrieved from: http://adsabs.harvard.edu/abs/2014ApJ...789...82C

[139] S. E. Clark, J. C. Hill, J. E. G. Peek, M. E. Putman, and B. L. Babler, "Neutral Hydrogen Structures Trace Dust Polarization Angle: Implications for Cosmic Microwave Background Foregrounds," *Physical Review Letters*, vol. 115, no. 24, p. 241302, Dec. 2015. Retrieved from: http://adsabs.harvard.edu/abs/2015PhRvL.115x1302C

[140] P. M. W. Kalberla, J. Kerp, U. Haud, B. Winkel, N. Ben Bekhti, L. Flöer, and D. Lenz, "Cold Milky Way HI Gas in Filaments," *Ap. J.*, vol. 821, p. 117, Apr. 2016. Retrieved from: http://adsabs.harvard.edu/abs/2016ApJ...821..117K

[141] P. M. W. Kalberla and J. Kerp, "Anisotropies in the HI gas distribution toward 3C 196," *Astron. Astrophys.*, vol. 595, p. A37, Oct. 2016. Retrieved from: http://esoads.eso.org/abs/2016A%26A...595A..37K

[142] R. M. Crutcher, B. Wandelt, C. Heiles, E. Falgarone, and T. H. Troland, "Magnetic Fields in Interstellar Clouds from Zeeman Observations: Inference of Total Field Strengths by Bayesian Analysis," *Ap. J.*, vol. 725, pp. 466–479, Dec. 2010. Retrieved from: http://adsabs.harvard.edu/abs/2010ApJ...725..466C

[143] HI4PI Collaboration, "HI4PI: A full-sky H I survey based on EBHIS and GASS," *Astron. Astrophys.*, vol. 594, p. A116, Oct. 2016. Retrieved from: http://adsabs.harvard.edu/abs/2016A%26A...594A.116H

[144] J. E. G. Peek, B. L. Babler, Y. Zheng *et al.*, "The GALFA-H I Survey Data Release 2," *Ap. J. Suppl.*, vol. 234, p. 2, Jan. 2018. Retrieved from: http://adsabs.harvard.edu/abs/2018ApJS..234....2P

[145] N. M. McClure-Griffiths, S. Stanimirovic, C. Murray *et al.*, "Galactic and Magellanic Evolution with the SKA," in *Advancing Astrophysics with the Square Kilometre Array (AASKA14)*, Apr. 2015, p. 130. Retrieved from: https://ui.adsabs.harvard.edu/#abs/2015aska.confE.130M

[146] T. P. Ellsworth-Bowers, E. Rosolowsky, J. Glenn, A. Ginsburg, N. J. Evans, II, C. Battersby, Y. L. Shirley, and B. Svoboda, "The Bolocam Galactic Plane Survey. XII. Distance Catalog Expansion Using Kinematic Isolation of Dense Molecular Cloud Structures with ^{13}CO(1-0)," *Ap. J.*, vol. 799, p. 29, Jan. 2015. Retrieved from: http://adsabs.harvard.edu/abs/2015ApJ...799...29E

[147] Planck Collaboration, P. A. R. Ade, N. Aghanim *et al.*, "Planck intermediate results. XXXV. Probing the role of the magnetic field in the formation of structure in molecular clouds," *Astron. Astrophys.*, vol. 586, p. A138, Feb. 2016. Retrieved from: http://adsabs.harvard.edu/abs/2016A%26A...586A.138P

[148] A. Allen, Z.-Y. Li, and F. H. Shu, "Collapse of Magnetized Singular Isothermal Toroids. II. Rotation and Magnetic Braking," *Ap. J.*, vol. 599, pp. 363–379, Dec. 2003. Retrieved from: http://adsabs.harvard.edu/abs/2003ApJ...599..363A

[149] Z.-Y. Li, R. Krasnopolsky, H. Shang, and B. Zhao, "On the Role of Pseudodisk Warping and Reconnection in Protostellar Disk Formation in Turbulent Magnetized Cores," *Ap. J.*, vol. 793, p. 130, Oct. 2014. Retrieved from: http://adsabs.harvard.edu/abs/2014ApJ...793..130L

[150] D. A. Harper, M. C. Runyan, C. D. Dowell *et al.*, "Hawc+, the far-infrared camera and polarimeter for sofia," *Journal of Astronomical Instrumentation*, vol. 07, no. 04, p. 1840008, 2018. Retrieved from: https://doi.org/10.1142/S2251171718400081

[151] A. Lazarian, "Enhancement and Suppression of Heat Transfer by MHD Turbulence," *Ap. J. Lett.*, vol. 645, pp. L25–L28, Jul. 2006. Retrieved from: http://adsabs.harvard.edu/abs/2006ApJ...645L..25L

[152] ——, "Damping of Alfvén Waves by Turbulence and Its Consequences: From Cosmic-ray Streaming to Launching Winds," *Ap. J.*, vol. 833, p. 131, Dec. 2016. Retrieved from: http://adsabs.harvard.edu/abs/2016ApJ...833..131L

[153] A. Lazarian and E. T. Vishniac, "Reconnection in a Weakly Stochastic Field," *Ap. J.*, vol. 517, pp. 700–718, Jun. 1999. Retrieved from: http://adsabs.harvard.edu/abs/1999ApJ...517..700L

[154] S. Xu and A. Lazarian, "Magnetohydrodynamic turbulence and turbulent dynamo in partially ionized plasma," *New Journal of Physics*, vol. 19, no. 6, p. 065005, 2017. Retrieved from: http://stacks.iop.org/1367-2630/19/i=6/a=065005

[155] T. J. Jones, C. D. Dowell, E. Lopez Rodriguez *et al.*, "SOFIA Far Infrared Imaging Polarimetry of M82 and NGC 253: Exploring the Super-Galactic Wind," *arXiv e-prints*, p. arXiv:1812.06816, Dec. 2018. Retrieved from: https://ui.adsabs.harvard.edu/#abs/2018arXiv181206816J

[156] J. Silk and G. A. Mamon, "The current status of galaxy formation," *Research in Astronomy and Astrophysics*, vol. 12, pp. 917–946, Aug. 2012. Retrieved from: http://adsabs.harvard.edu/abs/2012RAA....12..917S

[157] R. S. Somerville and R. Davé, "Physical Models of Galaxy Formation in a Cosmological Framework," *ARAA*, vol. 53, pp. 51–113, Aug. 2015. Retrieved from: http://adsabs.harvard.edu/abs/2015ARA%26A..53...51S

[158] S. Fujimoto, M. Ouchi, K. Kohno *et al.*, "ALMA 26 Arcmin^2 Survey of GOODS-S at One Millimeter (ASAGAO): Average Morphology of High-z Dusty Star-forming Galaxies in an Exponential Disk ($n \simeq 1$)," *Ap. J.*, vol. 861, p. 7, Jul. 2018. Retrieved from: http://adsabs.harvard.edu/abs/2018ApJ...861....7F

[159] R. Cañameras, N. Nesvadba, R. Kneissl *et al.*, "Planck's dusty GEMS. IV. Star formation and feedback in a maximum

starburst at z = 3 seen at 60-pc resolution," *Astron. Astrophys.*, vol. 604, p. A117, Aug. 2017. Retrieved from: http://adsabs.harvard.edu/abs/2017A%26A...604A.117C

[160] A. King and K. Pounds, "Powerful Outflows and Feedback from Active Galactic Nuclei," *ARAA*, vol. 53, pp. 115–154, Aug. 2015. Retrieved from: http://adsabs.harvard.edu/abs/2015ARA%26A..53..115K

[161] J. S. Spilker, M. Aravena, M. Béthermin *et al.*, "Fast molecular outflow from a dusty star-forming galaxy in the early Universe," *Science*, vol. 361, pp. 1016–1019, Sep. 2018. Retrieved from: http://adsabs.harvard.edu/abs/2018Sci...361.1016S

[162] S. Dye, C. Furlanetto, L. Dunne *et al.*, "Modelling high-resolution ALMA observations of strongly lensed highly star-forming galaxies detected by Herschel," *MNRAS*, vol. 476, pp. 4383–4394, Jun. 2018. Retrieved from: http://adsabs.harvard.edu/abs/2018MNRAS.476.4383D

[163] C. Lamarche, A. Verma, A. Vishwas *et al.*, "Resolving Star Formation on Subkiloparsec Scales in the High-redshift Galaxy SDP.11 Using Gravitational Lensing," *Ap. J.*, vol. 867, p. 140, Nov. 2018. Retrieved from: http://adsabs.harvard.edu/abs/2018ApJ...867..140L

[164] P. Sharda, C. Federrath, E. da Cunha, A. M. Swinbank, and S. Dye, "Testing star formation laws in a starburst galaxy at redshift 3 resolved with ALMA," *MNRAS*, vol. 477, pp. 4380–4390, Jul. 2018. Retrieved from: http://adsabs.harvard.edu/abs/2018MNRAS.477.4380S

[165] M. Negrello, S. Amber, A. Amvrosiadis *et al.*, "The Herschel-ATLAS: a sample of 500 μm-selected lensed galaxies over 600 deg^2," *MNRAS*, vol. 465, pp. 3558–3580, Mar. 2017. Retrieved from: http://adsabs.harvard.edu/abs/2017MNRAS.465.3558N

[166] T. Treu, "Strong Lensing by Galaxies," *Ann. Rev. Astr. Ap.*, vol. 48, pp. 87–125, Sep. 2010. Retrieved from: http://adsabs.harvard.edu/abs/2010ARA%26A..48...87T

[167] M. Negrello, R. Hopwood, G. De Zotti *et al.*, "The Detection of a Population of Submillimeter-Bright, Strongly Lensed Galaxies," *Science*, vol. 330, p. 800, Nov. 2010. Retrieved from: http://adsabs.harvard.edu/abs/2010Sci...330..800N

[168] A. M. Swinbank, I. Smail, S. Longmore *et al.*, "Intense star formation within resolved compact regions in a galaxy at z = 2.3," *Nature*, vol. 464, pp. 733–736, Apr. 2010. Retrieved from: http://adsabs.harvard.edu/abs/2010Natur.464..733S

[169] F. Combes, M. Rex, T. D. Rawle *et al.*, "A bright z = 5.2 lensed submillimeter galaxy in the field of Abell 773. HLSJ091828.6+514223," *Astron. Astrophys.*, vol. 538, p. L4, Feb. 2012. Retrieved from: http://adsabs.harvard.edu/abs/2012A%26A...538L...4C

[170] Planck Collaboration, P. A. R. Ade, N. Aghanim *et al.*, "Planck 2015 results. XXVI. The Second Planck Catalogue of Compact Sources," *Astron. Astrophys.*, vol. 594, p. A26, Sep. 2016. Retrieved from: http://adsabs.harvard.edu/abs/2016A%26A...594A..26P

[171] M. Negrello, J. Gonzalez-Nuevo, G. De Zotti *et al.*, "On the statistics of proto-cluster candidates detected in the Planck all-sky survey," *MNRAS*, vol. 470, pp. 2253–2261, Sep. 2017. Retrieved from: http://adsabs.harvard.edu/abs/2017MNRAS.470.2253N

[172] R. A. Overzier, "The realm of the galaxy protoclusters. A review," *Astron. Astrophys. Rev.*, vol. 24, p. 14, Nov. 2016. Retrieved from: http://adsabs.harvard.edu/abs/2016A%26ARv..24...14O

[173] Planck Collaboration, P. A. R. Ade, N. Aghanim *et al.*, "Planck intermediate results. XXXIX. The Planck list of high-redshift source candidates," *Astron. Astrophys.*, vol. 596, p. A100, Dec. 2016. Retrieved from: http://adsabs.harvard.edu/abs/2016A%26A...596A.100P

[174] C.-Y. Chen, P. K. King, and Z.-Y. Li, "Change of Magnetic Field-gas Alignment at the Gravity-driven Alfvénic Transition in Molecular Clouds: Implications for Dust Polarization Observations," *Ap. J.*, vol. 829, p. 84, Oct. 2016. Retrieved from: http://adsabs.harvard.edu/abs/2016ApJ...829...84C

[175] R. J. Ivison, A. M. Swinbank, I. Smail *et al.*, "Herschel-ATLAS: A Binary HyLIRG Pinpointing a Cluster of Starbursting Protoellipticals," *Ap. J.*, vol. 772, p. 137, Aug. 2013. Retrieved from: http://adsabs.harvard.edu/abs/2013ApJ...772..137I

[176] T. Wang, D. Elbaz, E. Daddi *et al.*, "Discovery of a Galaxy Cluster with a Violently Starbursting Core at z = 2.506," *Ap. J.*, vol. 828, p. 56, Sep. 2016. Retrieved from: http://adsabs.harvard.edu/abs/2016ApJ...828...56W

[177] I. Oteo, R. J. Ivison, L. Dunne *et al.*, "An Extreme Protocluster of Luminous Dusty Starbursts in the Early Universe," *Ap. J.*, vol. 856, p. 72, Mar. 2018. Retrieved from: http://adsabs.harvard.edu/abs/2018ApJ...856...72O

[178] B. D. Metzger, P. K. G. Williams, and E. Berger, "Extragalactic Synchrotron Transients in the Era of Wide-field Radio Surveys. I. Detection Rates and Light Curve Characteristics," *Ap. J.*, vol. 806, p. 224, Jun. 2015. Retrieved from: http://adsabs.harvard.edu/abs/2015ApJ...806..224M

[179] Planck Collaboration, P. A. R. Ade, N. Aghanim *et al.*, "Planck 2013 results. XXX. Cosmic infrared background measurements and implications for star formation," *Astron. Astrophys.*, vol. 571, p. A30, Nov. 2014. Retrieved from: http://adsabs.harvard.edu/abs/2014A%26A...571A..30P

[180] P. Collaboration, P. A. R. Ade, N. Aghanim *et al.*, "Planck 2013 results. XVIII. The gravitational lensing-infrared background correlation," *Astron. Astrophys.*, vol. 571, p. A18, Nov. 2014. Retrieved from: http://adsabs.harvard.edu/abs/2014A%26A...571A..18P

[181] P. Madau and M. Dickinson, "Cosmic Star-Formation History," *ARA&A*, vol. 52, pp. 415–486, Aug. 2014. Retrieved from:

http://adsabs.harvard.edu/abs/2014ARA%26A..52..415M

[182] H.-Y. Wu and O. Doré, "Optimizing future experiments of cosmic far-infrared background: a principal component approach," *MNRAS*, vol. 467, pp. 4150–4160, Jun. 2017. Retrieved from: http://adsabs.harvard.edu/abs/2017MNRAS.467.4150W

[183] B. D. Sherwin and M. Schmittfull, "Delensing the CMB with the cosmic infrared background," *Phys. Rev. D.*, vol. 92, no. 4, p. 043005, Aug. 2015. Retrieved from: http://adsabs.harvard.edu/abs/2015PhRvD..92d3005S

[184] M. Tucci, V. Desjacques, and M. Kunz, "Cosmic infrared background anisotropies as a window into primordial non-Gaussianity," *MNRAS*, vol. 463, pp. 2046–2063, Dec. 2016. Retrieved from: http://adsabs.harvard.edu/abs/2016MNRAS.463.2046T

[185] Planck Collaboration, R. Adam, P. A. R. Ade *et al.*, "Planck intermediate results. XXX. The angular power spectrum of polarized dust emission at intermediate and high Galactic latitudes," *Astron. Astrophys.*, vol. 586, p. A133, Feb. 2016. Retrieved from: http://adsabs.harvard.edu/abs/2016A%26A...586A.133P

[186] N. Krachmalnicoff, E. Carretti, C. Baccigalupi *et al.*, "S-PASS view of polarized Galactic synchrotron at 2.3 GHz as a contaminant to CMB observations," *Astron. Astrophys.*, vol. 618, p. A166, Oct. 2018. Retrieved from: http://adsabs.harvard.edu/abs/2018A%26A...618A.166K

[187] U. Fuskeland, I. K. Wehus, H. K. Eriksen, and S. K. Næss, "Spatial Variations in the Spectral Index of Polarized Synchrotron Emission in the 9 yr WMAP Sky Maps," *Ap. J.*, vol. 790, p. 104, Aug. 2014. Retrieved from: https://ui.adsabs.harvard.edu/#abs/2014ApJ...790..104F

[188] Planck Collaboration, A. Abergel, P. A. R. Ade *et al.*, "Planck 2013 results. XI. All-sky model of thermal dust emission," *Astron. Astrophys.*, vol. 571, p. A11, Nov. 2014. Retrieved from: https://ui.adsabs.harvard.edu/#abs/2014A&A...571A..11P

[189] J. Chluba, J. C. Hill, and M. H. Abitbol, "Rethinking CMB foregrounds: systematic extension of foreground parametrizations," *MNRAS*, vol. 472, pp. 1195–1213, Nov. 2017. Retrieved from: http://adsabs.harvard.edu/abs/2017MNRAS.472.1195C

[190] Y. Fantaye, F. Stivoli, J. Grain, S. M. Leach, M. Tristram, C. Baccigalupi, and R. Stompor, "Estimating the tensor-to-scalar ratio and the effect of residual foreground contamination," *JCAP*, vol. 8, p. 1, Aug. 2011. Retrieved from: http://adsabs.harvard.edu/abs/2011JCAP...08..001F

[191] C. Armitage-Caplan, J. Dunkley, H. K. Eriksen, and C. Dickinson, "Impact on the tensor-to-scalar ratio of incorrect Galactic foreground modelling," *MNRAS*, vol. 424, pp. 1914–1924, Aug. 2012. Retrieved from: http://adsabs.harvard.edu/abs/2012MNRAS.424.1914A

[192] A. Kogut and D. J. Fixsen, "Foreground Bias from Parametric Models of Far-IR Dust Emission," *Ap. J.*, vol. 826, p. 101, Aug. 2016. Retrieved from: http://adsabs.harvard.edu/abs/2016ApJ...826..101K

[193] M. Remazeilles, C. Dickinson, H. K. K. Eriksen, and I. K. Wehus, "Sensitivity and foreground modelling for large-scale cosmic microwave background B-mode polarization satellite missions," *MNRAS*, vol. 458, pp. 2032–2050, May 2016. Retrieved from: http://adsabs.harvard.edu/abs/2016MNRAS.458.2032R

[194] R. Stompor, J. Errard, and D. Poletti, "Forecasting performance of CMB experiments in the presence of complex foreground contaminations," *Phys. Rev. D.*, vol. 94, no. 8, p. 083526, Oct. 2016. Retrieved from: http://adsabs.harvard.edu/abs/2016PhRvD..94h3526S

[195] R. Génova-Santos, J. A. Rubiño-Martín, R. Rebolo *et al.*, "QUIJOTE scientific results - I. Measurements of the intensity and polarisation of the anomalous microwave emission in the Perseus molecular complex," *MNRAS*, vol. 452, pp. 4169–4182, Oct. 2015. Retrieved from: http://adsabs.harvard.edu/abs/2015MNRAS.452.4169G

[196] M. Remazeilles, C. Dickinson, H. K. K. Eriksen, and I. K. Wehus, "Sensitivity and foreground modelling for large-scale cosmic microwave background B-mode polarization satellite missions," *MNRAS*, vol. 458, pp. 2032–2050, May 2016. Retrieved from: http://adsabs.harvard.edu/abs/2016MNRAS.458.2032R

[197] J. S. Greaves, W. S. Holland, P. Friberg, and W. R. F. Dent, "Polarized CO Emission from Molecular Clouds," *Ap. J. Lett.*, vol. 512, pp. L139–L142, Feb. 1999. Retrieved from: http://adsabs.harvard.edu/abs/1999ApJ...512L.139G

[198] G. Puglisi, G. Fabbian, and C. Baccigalupi, "A 3D model for carbon monoxide molecular line emission as a potential cosmic microwave background polarization contaminant," *MNRAS*, vol. 469, pp. 2982–2996, Aug. 2017. Retrieved from: http://adsabs.harvard.edu/abs/2017MNRAS.469.2982P

[199] L. Bonavera, J. González-Nuevo, F. Argüeso, and L. Toffolatti, "Statistics of the fractional polarization of compact radio sources in Planck maps," *MNRAS*, vol. 469, pp. 2401–2411, Aug. 2017. Retrieved from: http://adsabs.harvard.edu/abs/2017MNRAS.469.2401B

[200] G. Puglisi, V. Galluzzi, L. Bonavera *et al.*, "Forecasting the Contribution of Polarized Extragalactic Radio Sources in CMB Observations," *Ap. J.*, vol. 858, p. 85, May 2018. Retrieved from: http://adsabs.harvard.edu/abs/2018ApJ...858...85P

[201] T. Trombetti, C. Burigana, G. De Zotti, V. Galluzzi, and M. Massardi, "Average fractional polarization of extragalactic sources at Planck frequencies," *Astron. Astrophys.*, vol. 618, p. A29, Oct. 2018. Retrieved from: http://adsabs.harvard.edu/abs/2018A%26A...618A..29T

[202] L. Toffolatti, C. Burigana, F. Argüeso, and J. María Diego, "Extragalactic compact sources in the planck sky and their cosmological implications," in *Open Questions in Cosmology, first edition*. InTech Open, 11 2012, pp. 57–86. Retrieved

from: http://adsabs.harvard.edu/abs/2013arXiv1302.3355T

[203] M. Remazeilles, A. J. Banday, C. Baccigalupi *et al.*, "Exploring cosmic origins with CORE: B-mode component separation," *JCAP*, vol. 4, p. 023, Apr. 2018. Retrieved from: http://adsabs.harvard.edu/abs/2018JCAP...04..023R

[204] H. K. Eriksen, J. B. Jewell, C. Dickinson, A. J. Banday, K. M. Górski, and C. R. Lawrence, "Joint Bayesian Component Separation and CMB Power Spectrum Estimation," *Ap. J.*, vol. 676, pp. 10–32, Mar. 2008. Retrieved from: http://adsabs.harvard.edu/abs/2008ApJ...676...10E

[205] J. Delabrouille, J.-F. Cardoso, and G. Patanchon, "Multidetector multicomponent spectral matching and applications for cosmic microwave background data analysis," *MNRAS*, vol. 346, pp. 1089–1102, Dec. 2003. Retrieved from: http://adsabs.harvard.edu/abs/2003MNRAS.346.1089D

[206] J.-F. Cardoso, M. Le Jeune, J. Delabrouille, M. Betoule, and G. Patanchon, "Component Separation With Flexible Models - Application to Multichannel Astrophysical Observations," *IEEE Journal of Selected Topics in Signal Processing*, vol. 2, pp. 735–746, Nov. 2008. Retrieved from: http://adsabs.harvard.edu/abs/2008ISTSP...2..735C

[207] S. Basak and J. Delabrouille, "A needlet ILC analysis of WMAP 9-year polarization data: CMB polarization power spectra," *MNRAS*, vol. 435, pp. 18–29, Oct. 2013. Retrieved from: http://adsabs.harvard.edu/abs/2013MNRAS.435...18B

[208] M. Remazeilles, J. Delabrouille, and J.-F. Cardoso, "Foreground component separation with generalized Internal Linear Combination," *MNRAS*, vol. 418, pp. 467–476, Nov. 2011. Retrieved from: http://adsabs.harvard.edu/abs/2011MNRAS.418..467R

[209] J. Errard, S. M. Feeney, H. V. Peiris, and A. H. Jaffe, "Robust forecasts on fundamental physics from the foreground-obscured, gravitationally-lensed CMB polarization," *JCAP*, vol. 3, p. 052, Mar. 2016. Retrieved from: http://adsabs.harvard.edu/abs/2016JCAP...03..052E

[210] B. Thorne, J. Dunkley, D. Alonso, and S. Næss, "The Python Sky Model: software for simulating the Galactic microwave sky," *MNRAS*, vol. 469, pp. 2821–2833, Aug. 2017. Retrieved from: http://adsabs.harvard.edu/abs/2017MNRAS.469.2821T

[211] K. M. Górski, E. Hivon, A. J. Banday, B. D. Wandelt, F. K. Hansen, M. Reinecke, and M. Bartelmann, "HEALPix: A Framework for High-Resolution Discretization and Fast Analysis of Data Distributed on the Sphere," *Ap. J.*, vol. 622, pp. 759–771, Apr. 2005. Retrieved from: http://adsabs.harvard.edu/abs/2005ApJ...622..759G

[212] W. Hu, M. M. Hedman, and M. Zaldarriaga, "Benchmark parameters for CMB polarization experiments," *Phys. Rev. D.*, vol. 67, pp. 043 004–+, Feb. 2003, astro-ph/0210096. Retrieved from: http://adsabs.harvard.edu/cgi-bin/nph-bib_query?bibcode=2003PhRvD..67d3004H&db_key=AST

[213] M. Shimon, B. Keating, N. Ponthieu, and E. Hivon, "CMB polarization systematics due to beam asymmetry: Impact on inflationary science," *Phys. Rev. D.*, vol. 77, no. 8, pp. 083 003–+, Apr. 2008. Retrieved from: http://adsabs.harvard.edu/abs/2008PhRvD..77h3003S

[214] A. P. S. Yadav, M. Su, and M. Zaldarriaga, "Primordial B-mode diagnostics and self-calibrating the CMB polarization," *Phys. Rev. D.*, vol. 81, no. 6, pp. 063 512–+, Mar. 2010. Retrieved from: http://adsabs.harvard.edu/abs/2010PhRvD..81f3512Y

[215] L. M. Griffiths and C. H. Lineweaver, "Testing the Cosmic Microwave Background Data for Systematic Effects," *Ap. J.*, vol. 603, pp. 371–382, Mar. 2004. Retrieved from: http://adsabs.harvard.edu/abs/2004ApJ...603..371G

[216] Planck Collaboration, P. A. R. Ade, J. Aumont *et al.*, "Planck 2015 results. III. LFI systematic uncertainties," *Astron. Astrophys.*, vol. 594, p. A3, Sep. 2016. Retrieved from: http://adsabs.harvard.edu/abs/2016A%26A...594A...3P

[217] J. Kaplan and J. Delabrouille, "Some sources of systematic errors on CMB polarized measurements with bolometers," in *Astrophysical Polarized Backgrounds*, ser. American Institute of Physics Conference Series, S. Cecchini, S. Cortiglioni, R. Sault, and C. Sbarra, Eds., vol. 609, Mar. 2002, pp. 209–214. Retrieved from: http://adsabs.harvard.edu/abs/2002AIPC..609..209K

[218] N. J. Miller, M. Shimon, and B. G. Keating, "CMB polarization systematics due to beam asymmetry: Impact on cosmological birefringence," *Phys. Rev. D.*, vol. 79, no. 10, p. 103002, May 2009. Retrieved from: http://adsabs.harvard.edu/abs/2009PhRvD..79j3002M

[219] L. Pagano, P. de Bernardis, G. de Troia *et al.*, "CMB polarization systematics, cosmological birefringence, and the gravitational waves background," *Phys. Rev. D.*, vol. 80, no. 4, p. 043522, Aug. 2009. Retrieved from: http://adsabs.harvard.edu/abs/2009PhRvD..80d3522P

[220] Planck Collaboration, P. A. R. Ade, N. Aghanim *et al.*, "Planck 2015 results. XII. Full focal plane simulations," *Astron. Astrophys.*, vol. 594, p. A12, Sep. 2016. Retrieved from: http://adsabs.harvard.edu/abs/2016A%26A...594A..12P

[221] P. Natoli, M. Ashdown, R. Banerji *et al.*, "Exploring cosmic origins with CORE: Mitigation of systematic effects," *Journal of Cosmology and Astro-Particle Physics*, vol. 2018, p. 022, Apr. 2018. Retrieved from: https://ui.adsabs.harvard.edu/#abs/2018JCAP...04..022N

[222] J. Aumont, J. F. Macías-Pérez, A. Ritacco, N. Ponthieu, and A. Mangilli, "Absolute calibration of the polarisation angle for future CMB *B*-mode experiments from current and future measurements of the Crab nebula," *ArXiv e-prints*, May 2018. Retrieved from: http://adsabs.harvard.edu/abs/2018arXiv180510475A

[223] "Pico website." Retrieved from: https://sites.google.com/umn.edu/picomission/home

[224] J. H. Kang, P. A. R. Ade, Z. Ahmed *et al.*, "2017 upgrade and performance of BICEP3: a 95GHz refracting telescope for degree-scale CMB polarization," in *Millimeter, Submillimeter, and Far-Infrared Detectors and Instrumentation for Astronomy IX*, ser. Society of Photo-Optical Instrumentation Engineers (SPIE) Conference Series, vol. 10708, Jul. 2018, p. 107082N. Retrieved from: http://adsabs.harvard.edu/abs/2018SPIE10708E..2NK

[225] Private communication.

[226] K. Young, M. Alvarez, N. Battaglia *et al.*, "Optical design of PICO: a concept for a space mission to probe inflation and cosmic origins," in *Society of Photo-Optical Instrumentation Engineers (SPIE) Conference Series*, vol. 10698, Aug. 2018, p. 1069846. Retrieved from: https://ui.adsabs.harvard.edu/#abs/2018SPIE10698E..46Y

[227] P. de Bernardis, P. A. R. Ade, J. J. A. Baselmans *et al.*, "Exploring cosmic origins with CORE: The instrument," *Journal of Cosmology and Astro-Particle Physics*, vol. 2018, p. 015, Apr. 2018. Retrieved from: https://ui.adsabs.harvard.edu/#abs/2018JCAP...04..015D

[228] S. M. Duff, J. Austermann, J. A. Beall *et al.*, "Advanced ACTPol Multichroic Polarimeter Array Fabrication Process for 150 mm Wafers," *Journal of Low Temperature Physics*, vol. 184, pp. 634–641, Aug. 2016. Retrieved from: https://ui.adsabs.harvard.edu/#abs/2016JLTP..184..634D

[229] BICEP2 Collaboration, Keck Array Collaboration, SPIDER Collaboration *et al.*, "Antenna-coupled TES Bolometers Used in BICEP2, Keck Array, and Spider," *Ap. J.*, vol. 812, p. 176, Oct. 2015. Retrieved from: https://ui.adsabs.harvard.edu/#abs/2015ApJ...812..176B

[230] J. M. Edwards, R. O'Brient, A. T. Lee, and G. M. Rebeiz, "Dual-Polarized Sinuous Antennas on Extended Hemispherical Silicon Lenses," *IEEE Transactions on Antennas and Propagation*, vol. 60, pp. 4082–4091, Sep. 2012. Retrieved from: https://ui.adsabs.harvard.edu/#abs/2012ITAP...60.4082E

[231] A. Suzuki, K. Arnold, J. Edwards *et al.*, "Multi-Chroic Dual-Polarization Bolometric Detectors for Studies of the Cosmic Microwave Background," *Journal of Low Temperature Physics*, vol. 176, pp. 650–656, Sep. 2014. Retrieved from: https://ui.adsabs.harvard.edu/#abs/2014JLTP..176..650S

[232] R. O'Brient, P. Ade, K. Arnold *et al.*, "A dual-polarized broadband planar antenna and channelizing filter bank for millimeter wavelengths," *Applied Physics Letters*, vol. 102, p. 063506, Feb. 2013. Retrieved from: https://ui.adsabs.harvard.edu/#abs/2013ApPhL.102f3506O

[233] E. D. Shirokoff, "The South Pole Telescope bolometer array and the measurement of secondary Cosmic Microwave Background anisotropy at small angular scales," Ph.D. dissertation, University of California, Berkeley, Jan. 2011. Retrieved from: https://ui.adsabs.harvard.edu/#abs/2011PhDT.......383S

[234] L. Bleem, P. Ade, K. Aird *et al.*, "An Overview of the SPTpol Experiment," *Journal of Low Temperature Physics*, vol. 167, pp. 859–864, Jun. 2012. Retrieved from: https://ui.adsabs.harvard.edu/#abs/2012JLTP..167..859B

[235] A. D. Turner, J. J. Bock, J. W. Beeman *et al.*, "Silicon nitride Micromesh Bolometer Array for Submillimeter Astrophysics," *Appl. Optics*, vol. 40, pp. 4921–4932, Oct. 2001. Retrieved from: https://ui.adsabs.harvard.edu/#abs/2001ApOpt..40.4921T

[236] A. D. Beyer, M. E. Kenyon, P. M. Echternach *et al.*, "Ultra-sensitive Transition-Edge Sensors for the Background Limited Infrared/Sub-mm Spectrograph (BLISS)," *Journal of Low Temperature Physics*, vol. 167, pp. 182–187, May 2012. Retrieved from: http://adsabs.harvard.edu/abs/2012JLTP..167..182B

[237] A. S. Rahlin, P. A. R. Ade, M. Amiri *et al.*, "Pre-flight integration and characterization of the SPIDER balloon-borne telescope," in *Millimeter, Submillimeter, and Far-Infrared Detectors and Instrumentation for Astronomy VII*, vol. 9153, Jul. 2014, p. 915313. Retrieved from: https://ui.adsabs.harvard.edu/#abs/2014SPIE.9153E..13R

[238] S. W. Henderson, R. Allison, J. Austermann *et al.*, "Advanced ACTPol Cryogenic Detector Arrays and Readout," *Journal of Low Temperature Physics*, vol. 184, pp. 772–779, Aug. 2016. Retrieved from: https://ui.adsabs.harvard.edu/#abs/2016JLTP..184..772H

[239] H. Hui, P. A. R. Ade, Z. Ahmed *et al.*, "BICEP Array: a multi-frequency degree-scale CMB polarimeter," in *Society of Photo-Optical Instrumentation Engineers (SPIE) Conference Series*, vol. 10708, Jul. 2018, p. 1070807. Retrieved from: https://ui.adsabs.harvard.edu/#abs/2018SPIE10708E..07H

[240] M. C. Runyan, P. A. R. Ade, M. Amiri *et al.*, "Design and performance of the SPIDER instrument," in *Millimeter, Submillimeter, and Far-Infrared Detectors and Instrumentation for Astronomy V*, vol. 7741, Jul. 2010, p. 77411O. Retrieved from: https://ui.adsabs.harvard.edu/#abs/2010SPIE.7741E..1OR

[241] Z. D. Kermish, "The POLARBEAR Experiment: Design and Characterization," Ph.D. dissertation, University of California, Berkeley, 2012. Retrieved from: http://adsabs.harvard.edu/abs/2012PhDT.......145K

[242] EBEX Collaboration, A. M. Aboobaker, P. Ade *et al.*, "The EBEX Balloon-borne Experiment: Optics, Receiver, and Polarimetry," *The Astrophysical Journal Supplement Series*, vol. 239, p. 7, Nov. 2018. Retrieved from: https://ui.adsabs.harvard.edu/#abs/2018ApJS..239....7T

[243] BICEP2 Collaboration, P. A. R. Ade, R. W. Aikin *et al.*, "Detection of B-Mode Polarization at Degree Angular Scales by BICEP2," *Phys. Rev. Lett.*, vol. 112, p. 241101, Jun. 2014. Retrieved from: https://ui.adsabs.harvard.edu/#abs/2014PhRvL.112x1101B

[244] F. Pajot, "Planck compression," Private communication.

[245] Planck HFI Core Team, P. A. R. Ade, N. Aghanim *et al.*, "Planck early results. IV. First assessment of the High Frequency Instrument in-flight performance," *Astron. Astrophys.*, vol. 536, p. A4, Dec. 2011. Retrieved from: https://ui.adsabs.harvard.edu/#abs/2011A&A...536A...4P

[246] The EBEX Collaboration, A. Aboobaker, P. Ade *et al.*, "The EBEX Balloon-borne Experiment—Gondola, Attitude Control, and Control Software," *The Astrophysical Journal Supplement Series*, vol. 239, p. 9, Nov. 2018. Retrieved from: https://ui.adsabs.harvard.edu/#abs/2018ApJS..239....9T

[247] M. Donabedian, A. I. of Aeronautics, and Astronautics, *Spacecraft Thermal Control Handbook, Vol. 2: Cryogenics*, ser. EngineeringPro collection. Aerospace Press, 2003. Retrieved from: https://books.google.com/books?id=nsLqjwEACAAJ

[248] R. G. Ross, "Estimation of thermal conduction loads for structural supports of cryogenic spacecraft assemblies," *Cryogenics*, vol. 44, pp. 421–424, Jun. 2004. Retrieved from: https://ui.adsabs.harvard.edu/#abs/2004Cryo...44..421R

[249] M. Petach and M. Michaelian, "Mid InfraRed Instrument (MIRI) cooler cold head assembly acceptance testing and characterization," *Cryocoolers*, vol. 18, p. 11, 2014. Retrieved from: https://cryocoolerorg.wildapricot.org/resources/Documents/C18/002.pdf

[250] P. J. Shirron, M. O. Kimball, D. J. Fixsen, A. J. Kogut, X. Li, and M. J. DiPirro, "Design of the PIXIE adiabatic demagnetization refrigerators," *Cryogenics*, vol. 52, pp. 140–144, Apr. 2012. Retrieved from: https://ui.adsabs.harvard.edu/#abs/2012Cryo...52..140S

[251] P. J. Shirron, M. O. Kimball, B. L. James *et al.*, "Thermodynamic performance of the 3-stage ADR for the Astro-H Soft-X-ray Spectrometer instrument," *Cryogenics*, vol. 74, pp. 24–30, Mar. 2016. Retrieved from: https://ui.adsabs.harvard.edu/#abs/2016Cryo...74...24S

[252] D. Durand, R. Colbert, C. Jaco, M. Michaelian, T. Nguyen, M. Petach, and J. Raab, "Mid Infrared Instrument (miri) Cooler Subsystem Prototype Demonstration," in *Advances in Cryogenic Engineering*, ser. American Institute of Physics Conference Series, J. G. Weisend, J. Barclay, S. Breon *et al.*, Eds., vol. 52, Mar. 2008, pp. 807–814. Retrieved from: https://ui.adsabs.harvard.edu/#abs/2008AIPC..985..807D

[253] J. Rabb et al, "Ngas scw-4k," Presentation at the 2013 Space Cryogenics Workshop, 2013.

[254] D. S. Glaister, W. Gully, R. Ross, P. Hendershott, E. Marquardt, and V. Kotsubo, "Ball Aerospace 4-6 K Space Cryocooler," in *Advances in Cryogenic Engineering: Transactions of the Cryogenic Engineering Conference*, ser. American Institute of Physics Conference Series, I. Weisend, J. G., J. Barclay, S. Breon *et al.*, Eds., vol. 823, Apr. 2006, pp. 632–639. Retrieved from: https://ui.adsabs.harvard.edu/#abs/2006AIPC..823..632G

[255] F. Pajot, P. A. R. Ade, J. L. Beney *et al.*, "Planck pre-launch status: HFI ground calibration," *Astron. Astrophys.*, vol. 520, p. A10, Sep. 2010. Retrieved from: https://ui.adsabs.harvard.edu/#abs/2010A&A...520A..10P

[256] C. L. Bennett, M. Bay, M. Halpern *et al.*, "The Microwave Anisotropy Probe Mission," *Ap. J.*, vol. 583, pp. 1–23, Jan. 2003. Retrieved from: https://ui.adsabs.harvard.edu/#abs/2003ApJ...583....1B

[257] J. A. Tauber, N. Mandolesi, J. L. Puget *et al.*, "Planck pre-launch status: The Planck mission," *Astron. Astrophys.*, vol. 520, p. A1, Sep. 2010. Retrieved from: https://ui.adsabs.harvard.edu/#abs/2010A&A...520A...1T

[258] Space Exploration Technologies Corp., *Falcon 9 Launch Vehicle: Payload User's Guide, Rev 2*. Space Exploration Technologies Corp., October 2015. Retrieved from: https://www.spacex.com/sites/spacex/files/falcon_9_users_guide_rev_2.0.pdf

[259] W. Hu, M. M. Hedman, and M. Zaldarriaga, "Benchmark parameters for CMB polarization experiments," *Phys. Rev. D.*, vol. 67, p. 043004, Feb. 2003. Retrieved from: https://ui.adsabs.harvard.edu/#abs/2003PhRvD..67d3004H

[260] H. Kurki-Suonio, E. Keihänen, R. Keskitalo, T. Poutanen, A. S. Sirviö, D. Maino, and C. Burigana, "Destriping CMB temperature and polarization maps," *Astron. Astrophys.*, vol. 506, pp. 1511–1539, Nov. 2009. Retrieved from: https://ui.adsabs.harvard.edu/#abs/2009A&A...506.1511K

[261] Deep Space Network, Jet Propulsion Laboratory, California Institute of Technology, "Deep space network services catalog 820-100, rev. f." February 2015. Retrieved from: https://deepspace.jpl.nasa.gov/files/820-100-F1.pdf

[262] Planck Collaboration, R. Adam, P. A. R. Ade *et al.*, "Planck 2015 results. I. Overview of products and scientific results," *Astron. Astrophys.*, vol. 594, p. A1, Sep. 2016. Retrieved from: https://ui.adsabs.harvard.edu/#abs/2016A&A...594A...1P

[263] The Simons Observatory Collaboration, P. Ade, J. Aguirre *et al.*, "The Simons Observatory: Science goals and forecasts," *arXiv e-prints*, Aug. 2018. Retrieved from: https://ui.adsabs.harvard.edu/#abs/2018arXiv180807445T

[264] D. Dutcher, P. A. R. Ade, Z. Ahmed *et al.*, "Characterization and performance of the second-year SPT-3G focal plane," in *Society of Photo-Optical Instrumentation Engineers (SPIE) Conference Series*, vol. 10708, Jul. 2018, p. 107081Z. Retrieved from: https://ui.adsabs.harvard.edu/#abs/2018SPIE10708E..1ZD

[265] J. G. Staguhn, D. J. Benford, C. A. Allen *et al.*, "GISMO: a 2-millimeter bolometer camera for the IRAM 30 m telescope," in *Society of Photo-Optical Instrumentation Engineers (SPIE) Conference Series*, vol. 6275, Jun. 2006, p. 62751D. Retrieved from: https://ui.adsabs.harvard.edu/#abs/2006SPIE.6275E..1DS

[266] R. Gualtieri, J. P. Filippini, P. A. R. Ade *et al.*, "SPIDER: CMB Polarimetry from the Edge of Space," *Journal of Low Temperature Physics*, vol. 193, pp. 1112–1121, Dec. 2018. Retrieved from: http://adsabs.harvard.edu/abs/2018JLTP..193.1112G

[267] J. P. Filippini, "No title," *in preparation*, 2019.

[268] W. S. Holland, D. Bintley, E. L. Chapin *et al.*, "SCUBA-2: the 10 000 pixel bolometer camera on the James Clerk Maxwell Telescope," *MNRAS*, vol. 430, pp. 2513–2533, Apr. 2013. Retrieved from: https://ui.adsabs.harvard.edu/#abs/2013MNRAS.430.2513H

[269] W. B. Doriese, K. M. Morgan, D. A. Bennett *et al.*, "Developments in Time-Division Multiplexing of X-ray Transition-Edge Sensors," *Journal of Low Temperature Physics*, vol. 184, pp. 389–395, Jul. 2016. Retrieved from: https://ui.adsabs.harvard.edu/#abs/2016JLTP..184..389D

[270] Y. Li, J. E. Austermann, J. A. Beall *et al.*, "Performance of the advanced ACTPol low frequency array," in *Society of Photo-Optical Instrumentation Engineers (SPIE) Conference Series*, vol. 10708, Jul. 2018, p. 107080A. Retrieved from: https://ui.adsabs.harvard.edu/#abs/2018SPIE10708E..0AL

[271] B. Westbrook, A. Cukierman, A. Lee, A. Suzuki, C. Raum, and W. Holzapfel, "Development of the Next Generation of Multi-chroic Antenna-Coupled Transition Edge Sensor Detectors for CMB Polarimetry," *Journal of Low Temperature Physics*, vol. 184, pp. 74–81, Jul. 2016. Retrieved from: https://ui.adsabs.harvard.edu/#abs/2016JLTP..184...74W

[272] S. M. Simon, J. E. Golec, A. Ali *et al.*, "Feedhorn development and scalability for Simons Observatory and beyond," in *Society of Photo-Optical Instrumentation Engineers (SPIE) Conference Series*, vol. 10708, Jul. 2018, p. 107084B. Retrieved from: https://ui.adsabs.harvard.edu/#abs/2018SPIE10708E..4BS

[273] M. Ferlet, G. Laurent, B. Swinyard, J. Glenn, J. Bock, and K. Dohlen, "Characterisation of Herschel-SPIRE flight model optical performances," in *Space Telescopes and Instrumentation 2008: Optical, Infrared, and Millimeter*, ser. Society of Photo-Optical Instrumentation Engineers (SPIE) Conference Series, vol. 7010, Jul. 2008, p. 70102U. Retrieved from: https://ui.adsabs.harvard.edu/#abs/2008SPIE.7010E..2UF

[274] J. T. Sayre, P. Ade, K. A. Aird *et al.*, "Design and characterization of 90 GHz feedhorn-coupled TES polarimeter pixels in the SPTPol camera," in *Millimeter, Submillimeter, and Far-Infrared Detectors and Instrumentation for Astronomy VI*, vol. 8452, Sep. 2012, p. 845239. Retrieved from: https://ui.adsabs.harvard.edu/#abs/2012SPIE.8452E..39S

[275] B. Dober, D. T. Becker, D. A. Bennett *et al.*, "Microwave SQUID multiplexer demonstration for cosmic microwave background imagers," *Applied Physics Letters*, vol. 111, p. 243510, Dec. 2017. Retrieved from: https://ui.adsabs.harvard.edu/#abs/2017ApPhL.111x3510D

[276] K. D. Irwin and K. W. Lehnert, "Microwave SQUID multiplexer," *Applied Physics Letters*, vol. 85, p. 2107, Sep. 2004. Retrieved from: https://ui.adsabs.harvard.edu/#abs/2004ApPhL..85.2107I

[277] H. McCarrick, G. Jones, B. R. Johnson *et al.*, "Design and performance of dual-polarization lumped-element kinetic inductance detectors for millimeter-wave polarimetry," *Astron. Astrophys.*, vol. 610, p. A45, Feb. 2018. Retrieved from: http://adsabs.harvard.edu/abs/2018A%26A...610A..45M

[278] B. A. Steinbach, J. J. Bock, H. T. Nguyen, R. C. O'Brient, and A. D. Turner, "Thermal Kinetic Inductance Detectors for Ground-Based Millimeter-Wave Cosmology," *Journal of Low Temperature Physics*, vol. 193, pp. 88–95, Nov. 2018. Retrieved from: https://ui.adsabs.harvard.edu/#abs/2018JLTP..193...88S

[279] B. R. Johnson, D. Flanigan, M. H. Abitbol *et al.*, "Development of Multi-chroic MKIDs for Next-Generation CMB Polarization Studies," *Journal of Low Temperature Physics*, vol. 193, pp. 103–112, Nov. 2018. Retrieved from: http://adsabs.harvard.edu/abs/2018JLTP..193..103J

[280] P. Gloesener, "Large Aluminium Convex Mirror for the Cryo-Optical Test of the Planck Primary Reflector," in *ESA Special Publication*, vol. 621, Jun. 2006, p. 43. Retrieved from: https://ui.adsabs.harvard.edu/#abs/2006ESASP.621E..43G

[281] Y. Toulemont, T. Passvogel, G. Pillbrat, D. de Chambure, D. Pierot, and D. Castel, "The 3.5m all SiC telescope for Herschel," in *5th International Conference on Space Optics*, B. Warmbein, Ed., vol. 554, Jun. 2004, pp. 341–348. Retrieved from: https://ui.adsabs.harvard.edu/#abs/2004ESASP.554..341T

[282] Planck Collaboration, P. A. R. Ade, N. Aghanim *et al.*, "Planck early results. II. The thermal performance of Planck," *Astron. Astrophys.*, vol. 536, p. A2, Dec. 2011. Retrieved from: https://ui.adsabs.harvard.edu/#abs/2011A&A...536A...2P

[283] S. Bard, "Development of a High-Performance Cryogenic Radiator with V-Groove Radiation Shields," *Journal of Spacecraft and Rockets*, vol. 24, pp. 193–197, May 1987. Retrieved from: https://ui.adsabs.harvard.edu/#abs/1987JSpRo..24..193B

[284] European Space Agency, "Planck cooling system," September 2009. Retrieved from: http://sci.esa.int/planck/45498-cooling-system/?fbodylongid=2123

[285] T. S. Brown, *A GNC Perspective of the Launch and Commissioning of NASA's New SMAP (Soil Moisture Active Passive) Spacecraft*. American Institute of Aeronautics and Astronautics, 2018/11/19 2016. Retrieved from: https://doi.org/10.2514/6.2016-0479

[286] L. E. Z. Jasper and P. Xaypraseuth, "Data production on past and future nasa missions," in *2017 IEEE Aerospace Conference*, March 2017, pp. 1–11. Retrieved from: https://doi.org/10.1109/AERO.2017.7943918

[287] J. Mrozinski and M. DiNicola, "NICM: Cryocooler," NASA 2017 Cost Symposium Presentations, August 2017. Retrieved from: https://www.nasa.gov/offices/ocfo/cost_symposium/2017_presentations

[288] H. P. Stahl and T. Henrichs, "Multivariable parametric cost model for space and ground telescopes," in *Modeling, Systems Engineering, and Project Management for Astronomy VI*, ser. Society of Photo-Optical

Instrumentation Engineers (SPIE) Conference Series, vol. 9911, Sep. 2016, p. 99110L. Retrieved from: https://ui.adsabs.harvard.edu/#abs/2016SPIE.9911E..0LS